MULTISCALE MODELING AND UNCERTAINTY ANALYSIS OF MECHANICAL BEHAVIOR OF NANOSTRUCTURED METALS

A Dissertation
Presented to
The Academic Faculty

by

Zhi Zeng

In Partial Fulfillment
of the Requirements for the Degree
Doctor of Philosophy in the
Georgia W. Woodruff School of Mechanical Engineering

Georgia Institute of Technology
May 2017

MULTISCALE MODELING AND UNCERTAINTY ANALYSIS OF MECHANICAL BEHAVIOR OF NANOSTRUCTURED METALS

Approved by:

Dr. Ting Zhu, Advisor
School of Mechanical Engineering
Georgia Institute of Technology

Dr. Christopher Saldana
School of Mechanical Engineering
Georgia Institute of Technology

Dr. David L. McDowell
School of Mechanical Engineering
Georgia Institute of Technology

Dr. Hamid Garmestani
School of Materials Science and Engineering
Georgia Institute of Technology

Dr. Chaitanya Deo
School of Mechanical Engineering
Georgia Institute of Technology

Date Approved: February 7, 2017

ACKNOWLEDGEMENTS

Foremost, I would like to express my sincerest gratitude to my Ph.D. thesis advisor, Dr. Ting Zhu, for his invaluable guidance and continuous support for my Ph.D. study. He gave me strong motivation and helped me very patiently throughout my thesis work. He was very insightful in his mentorship. Working with him is one of the most precious experiences in my life.

I would like to thank my thesis committee members: Dr. David L. McDowell, Dr. Chaitanya Deo, Dr. Christopher Saldana and Dr. Hamid Garmestani, for their guidance that significantly enhance my work.

In addition, I want to extend my gratitude to Dr. Scott X. Mao from University of Pittsburg, Dr. Morris Wang from Lawrence Livermore National Laboratory, Dr. Andy Godfrey from Tsinghua University and Dr. Jiangwei Wang from Zhejiang University, for research collaboration. I would also like to thank my colleagues - Sankar Narayanan, Yuan Li and Yin Zhang for helpful discussions.

TABLE OF CONTENTS

LIST OF TABLES

LIST OF FIGURES

LIST OF SYMBOLS AND ABBREVIATIONS

HNM	heterogeneous nanostructured metals
FCC	face-centred cubic
BCC	body-centred cubic
GND	geometrically necessary dislocations
NG	nano-grained
GNG	gradient nano-grained
AM	additively manufacturing
TEM	transmission electron microscopy
SEM	scanning electron microscope
EBSD	electron backscatter diffraction
MD	molecular dynamics
MS	molecular static
NEB	nudged elastic band
RVE	representative volume element
CPFE	crystal plasticity finite element
SPS	spark plasma sintering
EAM	embedded atom method
σ	stress
ε	strain
m	Strain rate sensitivity
$\mathbf{F}$	deformation gradient tensor
$\mathbf{F}^*$	elastic deformation gradient

$\mathbf{F}^p$	plastic deformation gradient
$\mathbf{C}$	fourth-order elasticity tensor
$\mathbf{T}^*$	stress measure
$\mathbf{T}$	Cauchy stress
s^α	slip resistance
s_0	initial value of slip resistance
$\dot{\gamma}_o$	reference shearing rate
$\mathbf{E}^*$	elastic strain measure
h_0	hardening parameter
a	hardening parameter
s_{sat}	hardening parameter

SUMMARY

Metals with heterogeneous nanostructures hold great promise for achieving a synergy of ultra-high strength and ductility, thus overcoming the conventional strength-ductility tradeoff in nanostructured materials. To provide a fundamental understanding of the mechanics and physical mechanisms governing the strength and ductility in heterogeneous nanostructured metals, we conduct both atomistic and crystal plasticity modeling studies of heterogeneous nanostructured metals in this thesis. The heterogeneous nanostructured metals studied include gradient nano-grained copper, transmodal grained aluminum and additively manufactured stainless steel. A general modeling framework is developed for heterogeneous nanostructures. Specifically, we develop a Voronoi tessellation-based geometrical method to build the heterogeneous nano-grained structures. The distribution of grain size and the spatial arrangement of nonuniform grains are fully controllable. We also develop a crystal plasticity finite element model that accounts for grain-size-dependent yield strength and strain hardening. The associated finite element simulations reveal both the gradient stress and gradient plastic strain. To gain mechanistic insights into the controlling deformation mechanisms in heterogeneous nanostructured metals, we perform large scale molecular dynamics simulations to reveal grain boundary-dominated plastic deformation. Moreover, we also perform atomistic studies of unit processes of plastic deformation, including dislocation slip, deformation twinning and grain boundary sliding, through direct coupling with in situ transmission electron microscopy experiment. The uncertainties arising from the heterogeneous grains with a variety of size and spatial distributions are quantified. Heterogeneous microstructures turn

microstructure uncertainties into valuable features of material properties. This thesis work provides the fundamental understanding of strength and ductility as well as unit deformation mechanisms of nanostructured metals. Furthermore, our uncertainty study has important implications for the design and fabrication of high-performance nanostructured materials.

CHAPTER 1. INTRODUCTION

1.1 Heterogeneous nanostructured metals

Metals are the workhorse material for the manufacturing industry and structural applications. This is largely because they have a good balance of strength and ductility. There is however a relentless quest to reach a more superior combination of strength and ductility. Unfortunately, these two properties are usually considered mutually exclusive: a gain in strength is inevitably accompanied by a sacrifice in ductility, resulting in a strength-ductility tradeoff[1-6]. For example, homogeneous nanocrystalline metals exhibit ultra-high strengths over 1 GPa, but that comes with diminishing tensile ductility. A major challenge, therefore, is to engineer novel microstructures to restore a respectable ductility to these high-strength metals, so as to achieve a desirable strength-ductility synergy[7, 8].

There have been many success stories in the design of multi-component and multiphase alloys[9-11], as well as composites[12, 13], to achieve high strength while retaining reasonable ductility. The focus in this review is, however, on single-phase materials, such as elemental metals or solid solutions based on a primary element or on an intermediate phase. Elemental and single-phase metals are desirable in many applications. For instance, additional components or phases increase variables of processing and cost, make the material prone to corrosion due to inhomogeneities and associated disparity in electrochemical potentials, reduce the electrical and thermal conductivity, and bring in sites for stress concentration and crack initiation. Moreover, precipitation and dispersion of different phases require a delicate control of the phase decomposition sequence (e.g., to avoid over-aging in precipitation hardening).

In recent years, new material processing routes have emerged that enable microstructural control on the nanometer scale. One can now create heterogeneous nanostructures in an otherwise single-phase metal. The progress to be reviewed here has exploited this opportunity, through a common design strategy of heterogeneous nanostructured metals (HNMs). From this particular standpoint, the primary questions we aim to address are i) what kind of nanostructure design in single-phase metals can push the boundary of the strength-ductility combination, and ii) what are the new deformation mechanisms responsible for the enhanced strength-ductility synergy in these heterogeneous nanostructures. From both the materials science and mechanics perspectives, the principles and lessons learnt from these simpler single-phase materials can also shed light on the design strategies of overcoming the strength-ductility tradeoff for complex alloys and composites.

The strength-ductility tradeoff. Strength and ductility are among the most important mechanical properties of materials for structures and devices. Conventional coarse-grained metals have relatively low strength, but high tensile ductility. Homogeneous nanocrystalline metals with grain size finer than 100 nm usually exhibit more than five times higher strength than their coarse-grained counterparts[10, 11]. This effect of "smaller is stronger" is generally understood in terms of the Hall-Petch effect of grain size strengthening. That is, grain boundaries can obstruct the motion of dislocations that serve as major carriers of plastic deformation at room temperature. As a result, the smaller the grains, the stronger resistances the grain boundaries provide against dislocation motion, and the higher the yield stress of plastic flow. In other words, the strength of polycrystalline metals can be increased by reducing the grain size. However, one drawback with this

strengthening approach is that the resulting materials suffer from greatly reduced ductility; the elongation to failure is an order of magnitude smaller than the failure strain (often >50%) in coarse-grained counterparts. In particular, the uniform elongation before strain localization (necking) decreases to less than a few percent. The shaded area in Figure 1.1 covers the typical experimental data of strength and ductility for various metals that have refined grains or dislocation structures, showing a fast loss of uniform elongation with increasing strength (the strength and ductility are normalized with the reference being the engineering yield stress and uniform elongation of the coarse-grained counterpart, respectively). Therefore, imparting high strength without conceding too much ductility is one of the major challenges in nanostructuring metals[14].

It should be emphasized that even a nanocrystalline metal is not intrinsically brittle due to the lack of plasticity mechanisms. For example, under a confined loading an electrodeposited Ni micropillar with 20 nm grain size can be compressed into a pancake (up to 200% true strain, or 85% reduction of its height) without fracture[15]. It is just that under high *tensile* stresses, the plastic elongation is susceptible to a localized necking deformation that instigates early failure. It is well known from the Hart criterion[16, 17] that the necking instability sets in when

$$\frac{d\sigma}{d\varepsilon} + m\sigma \le \sigma \tag{1.1}$$

where σ is the true stress, ε is the true strain and m is the strain rate sensitivity. Since m is not sufficiently high ($m < 0.05$ at room temperature)[18-20], the strain-hardening rate $d\sigma / d\varepsilon$ (i.e., the tangent slope of the true stress-strain curve in Figure 1.2) has to be high enough to keep up with the increasing stress σ for averting the inequality in Equation (1),

so as to stabilize the uniform tensile plastic deformation. Incidentally, achieving a high tensile ductility resulting from enhanced stable plastic flow can be beneficial for improving fracture toughness[21], despite the different stress states under uniaxial tension and at the crack tip.

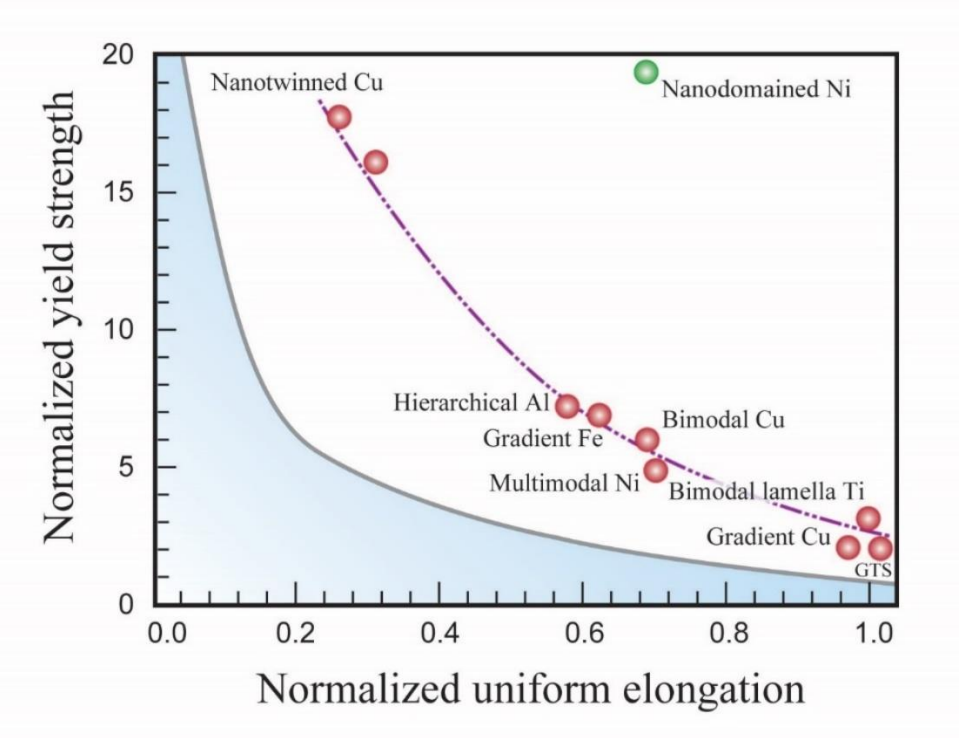

Figure 1.1 Yield strength versus tensile uniform elongation of metals. The shaded area under the banana-shaped curve covers the strength-ductility data of conventional metals with homogeneous microstructures. The reader is referred to the literature[2, 22, 23] for numerous data points already summarized previously. The solid circles along the dashed line (a guide to the eye) are HNM examples cited in the text with an elevated combination of strength and ductility; from left to right: nanotwinned Cu[23], hierarchical Al[24], gradient Fe[25], bimodal Cu[2], multimodal Ni[26], gradient Cu[27], bimodal lamella Ti[28], gradient TWIP steel (GTS) [29] and nanodomained Ni (the green point)[22]. Here the strength and ductility values have been normalized with respect to their coarse-grained counterpart as the reference. The reference yield strength and uniform elongation values are taken from the respective stress-strain curve of the coarse-grained sample presented for comparison in each of these references. The hierarchical Al[24] had the composition of a 7075 Al alloy, but was made into a *single-phase* FCC solid solution via severe plastic deformation; so comparison was made with reference to a solution-treated but un-aged bulk metastable single-phase alloy at this composition.

For almost all metals after strengthening such as cold working or grain refinement, the slope of the stress-strain curve in the plastic flow regime (strain hardening modulus) is much lower than for coarse-grained metals[18, 30]. For example, in nanocrystalline grains with abundant high-angle grain boundaries, almost all the dislocations mediating the plastic strain would quickly traverse the tiny crystal grains, and annihilate into the surrounding grain boundaries, with little chance and space to be retained inside[30]. This takes away an effective strain hardening mechanism in coarse-grained metals, i.e., the continuous multiplication and storage of dislocations during plastic straining. Consequently, $d\sigma/d\varepsilon$ is typically low, leading to an early necking instability at a low tensile strain, especially when compounded by a high tensile stress. As shown in Figure 1.2 using homogenously-grained Ni with different grain sizes as an example, with increasing yield strength (decreasing grain size) the uniform elongation drops fast, all the way to the nanocrystalline case (18 nm) where the tensile ductility almost vanishes. This example further demonstrates the strength-ductility tradeoff shown in Figure 1.1.

A high strain hardening capability is therefore key to evading the strength-ductility tradeoff. In this regard, creation of heterogeneous nanostructures is particularly beneficial and has therefore served as an overarching mechanism in promoting strength-ductility synergy. In heterogeneous structures, soft and hard regions (e.g., small and large grains) are mixed together. Soft regions deform plastically more than hard regions, so that gradients of plastic deformation build up. Accommodation of such plastic gradients requires the storage of geometrically necessary dislocations[31] (dislocations of the same sign), which contribute to work hardening. This is a non-local effect of strengthening. The characteristic length scale of gradient plastic deformation, λ, is determined by the spacing

between neighboring soft and hard regions. It was pointed out by Ashby[31] long time ago that the density of geometrically necessary dislocations is proportional to local plastic strain but inversely proportional to λ. Heterogeneous nanostructures are characterized by unusually small λ, and thus offer a high capacity of storing more geometrically necessary dislocations, thereby enhancing strain hardening and consequently the strength-ductility synergy. This key message will be emphasized time and again, for HNMs that are plastically non-homogeneous[31] with large strain gradients.

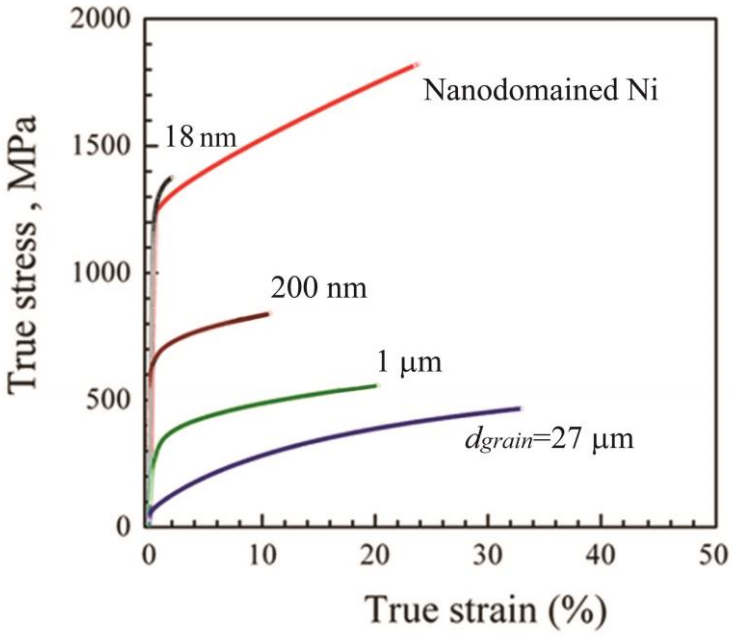

Figure 1.2 Tensile stress-strain curves of Ni[22]. The coarse-grained Ni has an average grain size *d* of 27 μm. Other electrodeposited Ni samples have *d* ranging from 1 μm to 18 nm. The electroplated Ni with nanodomains has an average domain size *d* of about 7 nm. The true stress-strain curves are converted from engineering stress-strain curves (up to the maximum stress point where non-uniform elongation sets in).

Thermomechanical routes for preparing heterogeneous microstructures normally involve severe plastic deformation[3, 4, 32] and dynamic plastic deformation[33, 34], followed by an annealing treatment. The resulting materials usually have complicated residual deformation microstructures as well as a strong deformation texture. With the newly acquired ability to control structure on the nanometer scale via either a top-down or a bottom-up approach, one can now purposely deploy heterogeneous nanostructures in an otherwise single-phase metal. In this thesis, we concentrate on several recent designs of HNMs, including gradient nano-grained metals, transmodal grained aluminum and additively manufactured 316 L stainless steel.

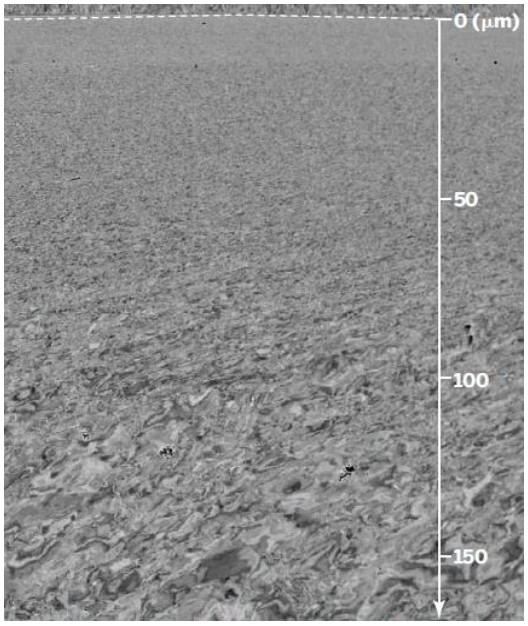

Figure 1.3 Scanning electron microscopy (SEM) image of gradient nano-grained Cu with a gradual gradient in grain size from the surface to interior[7].

Gradient nano-grained metals. At another front of research for controlling the grain size distribution, a spatial gradient in grain size can be produced in the surface layer of a metal, giving rise to "gradient nano-grained metals". Incidentally, materials with spatial gradients in composition and structure near surface has been of considerable interest in the field of tribology for enhancing resistance to contact deformation and damage[35]. In a recent study, Fang et al. used surface mechanical grinding treatment to process a gradient nano-grained layer enclosing a coarse-grained core of Cu[27]. As shown in Figure 1.3, the topmost layer of the gradient structure, up to a depth of 60 μm, consists of nano-grains with an average grain size of about 20 nm. The grain size gradually increases to about 300 nm in the depth of 60 μm to 150 μm. Below a depth of 150 μm, the grain size continues to increase to that of coarse grains at the micrometer scale. The gradient nano-grained layer exhibits a high yield strength, and when constrained by the substrate can sustain a tensile true strain exceeding 100% without cracking. Another example is that of Wu et al., who used surface mechanical attrition treatment to prepare the gradient nano-grained steel with a sandwich sheet structure, i.e., a coarse-grained core in between two surface gradient nano-grained layers[25]. The tensile tests showed that the gradient structure induces an extra strain hardening and hence high ductility. This extra strain hardening was attributed to the buildup of geometrically necessary dislocations, as well as to the multiaxial stress states arising from interplay between the coarse- and fine-grained sub-layers that promotes the activation of new slip systems and dislocation accumulation. Several examples of such gradient nano-grained metals are included in Figure 1.1. It should be noted that to date, most gradient nano-grained structures have been made on the surface of a coarse-grained substrate, graduated with a smooth gradient of grain size. The processing relies on surface

mechanical treatment that limits the thickness of the near-surface, gradient nano-grained layer. As a result, the strength-ductility synergy in the entire sample is limited. Further development in this direction thus calls for new processing routes to decrease the ratio of the thickness of the bulk sample to its hardened surface layer of gradient nano-grains. Very recently, Thevamaran et al. reported a dynamic creation of gradient nano-grained structures in single crystal silver microcubes undergoing high-velocity impact against an impenetrable substrate[36]. Their work demonstrated a promising pathway to develop gradient nano-grained metals with a large gradient of grain size. Hughes et al.[37, 38] used friction-induced nanograin refinement technique to produce nanocrystalline Cu with even smaller grain size.

***Transmodal grained aluminum*.** The spark plasma sintering process is more feasible to prepare designer HNMs by consolidating powders under a relatively low pressure while being heated through the application of a pulsed direct current. This method has been used to form metal samples with a fine grain size in near-micrometer regime[39]. Recent development allows for the sintering of metal powders of different sizes for creating bulk samples with a bimodal and even a trans-modal distribution of grain sizes. As shown in Figure 1.4, the polycrystalline Al has a combination of fine grains and coarse grains. The grains are well-mixed. We call this material 'bimodal grained Al'. The EBSD images of bimodal grained Al are shown in Figure 1.4. Furthermore, the proportion of the mixed powders are varied, respectively, with a weight ratio of 5.2μm of 0%, 12%, 25%, 37%, 50%, 63%, 75%, 88% and 100%. The microstructures of bimodal grained Al are varying with the proportion.

Figure 1.5 shows examples of heterogeneous grains with a bimodal (Figure 1.5(a)) versus a trans-modal (Figure 1.5(b)) distribution of grain sizes. We expect that a close integration of the above novel visualization techniques with material processing would provide a transformative approach for the creation of designer HNMs towards unprecedented strength-ductility synergy.

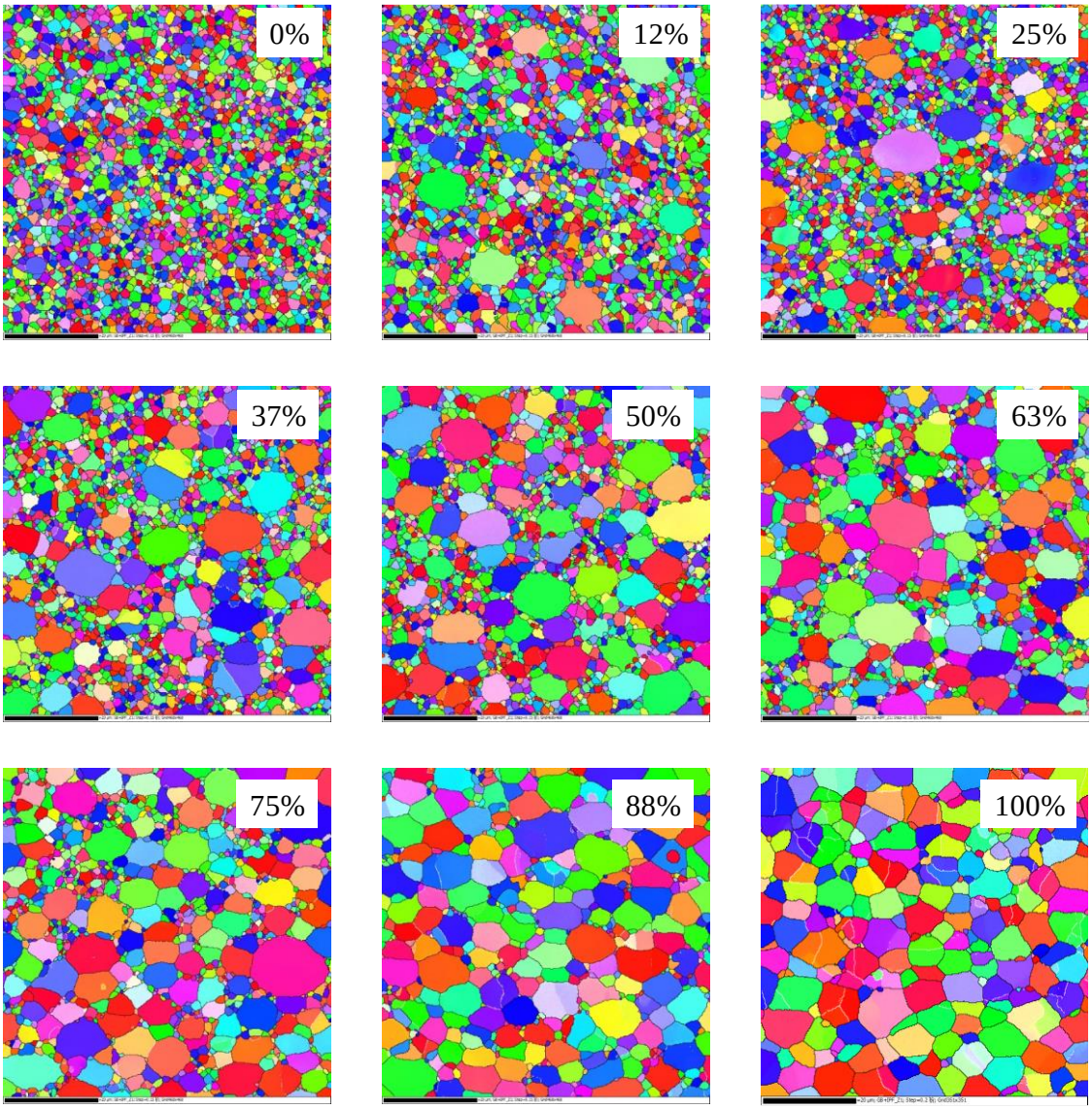

Figure 1.4 EBSD images of bimodal grained Al with different proportions of fine powders (0.8μm and coarse powders (5.2μm), respective; with a weight ratio of 5.2μm of 0%, 12%, 25%, 37%, 50%, 63%, 75%, 88% and 100%.

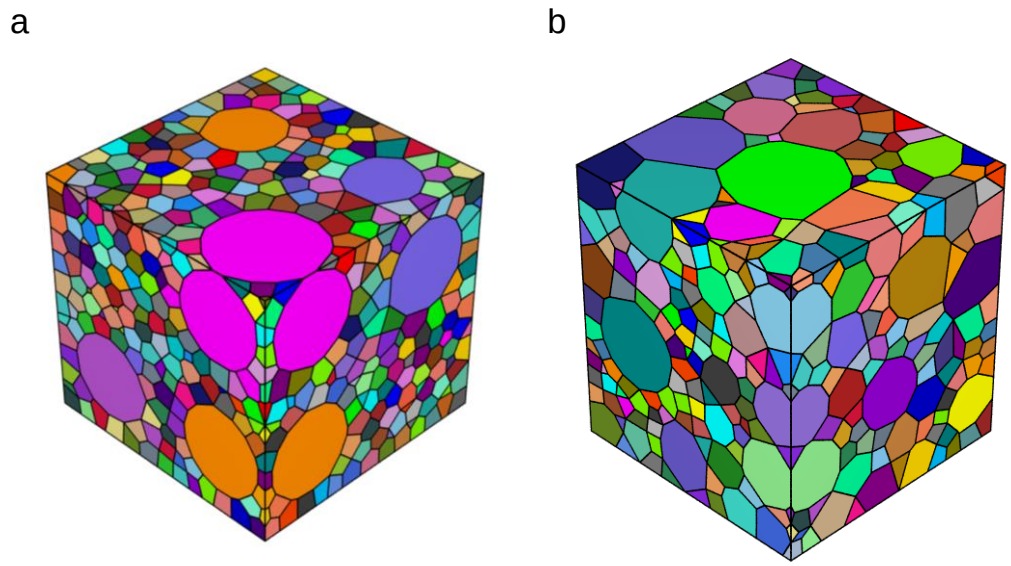

Figure 1.5 Structure models of heterogeneous grains with controllable grain size and distribution. (a) A bimodal grained structure with ~ 50 vol% grains of size of 0.8μm and 50 vol% grains of 5.2μm. (b) A trans-modal grained structure with a uniform distribution of grain sizes in between 0.8μm and 5.2μm. Grain is colored according to its orientation assigned randomly.

Additively manufactured stainless steel. Heterogeneous microstructures are the prominent feature in materials processed by additive manufacturing[40], which enables the building of three-dimensional (3D) objects by adding material layer-upon-layer, via for example spreading and selectively melting individual powder layers. While the required heterogeneity control on the nanometer scale is challenging to additive manufacturing at present, it may very well become easy in the near future, considering fast and continuous advances in novel additive manufacturing processing. Fullydense square-shaped pillars of 316L SS using L-PBF via an island scan strategy with a variety of laser powers and speeds. As an L-PBF process relies on layer-by-layer melting, welding and solidification of powder

precursors, several characteristic microstructures inevitably co-exist in AM parts, including anisotropic or elongated grains[41], voids, layered structures, and impurities. The cross-sectional, grain orientation and size distribution are measured by electron backscatter diffraction (EBSD) in a scanning electron microscope (SEM). Grains under EBSD exhibit a ripple pattern instead of a traditional faceted morphology. The EBSD also shows highly unconventional grain shape and distribution.

1.2 Multiscale modeling and uncertainty quantification

Successful predictive modeling for mechanical properties of nanostructured materials include two parts: mechanistic model and uncertainty analysis[42, 43]. Both of these two parts are addressed in this thesis. The mechanistic modeling of heterogeneous nanostructured metals is essentially a multiscale study. Figure 1.6 shows that the length scale of modeling spans over 9 orders of magnitude. At atomic scale, the modeling work in this thesis is focus on dislocations, twinning deformation and grain boundaries. The modeling methods are molecular dynamics (MD) simulations, molecular static (MS) simulations and nudged elastic band (NEB) simulations[44-46]. At mesoscale, the modeling work in this thesis is focus on grains, microstructure and representative volume element (RVE) of heterogeneous grains. The modeling methods are large scale molecular dynamics simulations and crystal plasticity finite element (CPFE) simulations[47-49]. The experimental measurements at the macroscopic scale are used to validate the simulation results. Moreover, due to the recent developments of high resolution transmission electron microscopy, we are able to directly compare the atomistic simulations to the experimental observations.

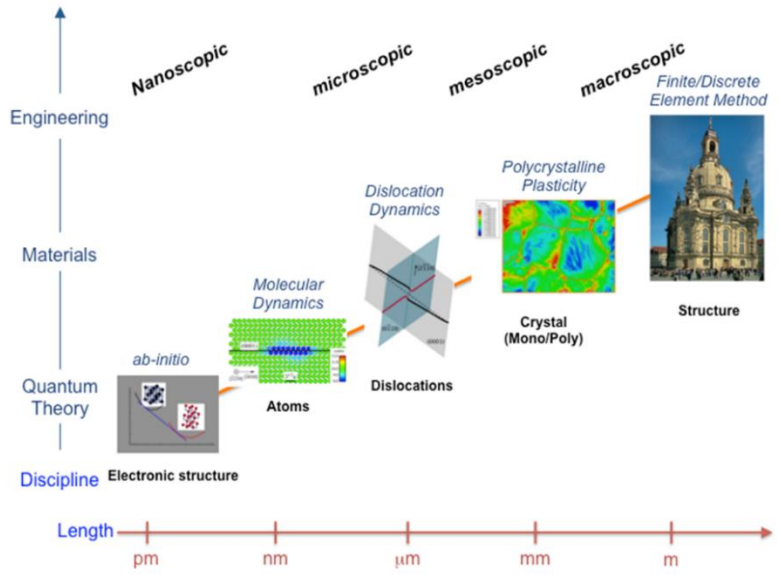

Figure 1.6 Multiscale mechanistic modeling of heterogeneous nanostructured metals. The modeling spans from atomic scale to mesoscopic scale, by performing molecular dynamics simulations, molecular static simulations, nudged elastic band simulations and crystal plasticity finite element simulations.

The uncertainties in the modeling of heterogeneous nanostructured metals is multiscale[50, 51]. There are both aleatory and epistemic uncertainties. The uncertainties have a hierarchical structure[43]. Figure 1.7 illustrates this hierarchical structure. At the lowest level which is at the atomic scale, the uncertainties arise from MD, MS and NEB simulations of unit processes; at the middle level which is at the mesoscopic scale, the uncertainties arise from the CPFE modeling of RVE of heterogeneous grains; at the highest level which is at the macroscopic scale, the uncertainties arise from the experimental measurements of structural samples. Furthermore, the uncertainties from a lower level are passed to an upper level.

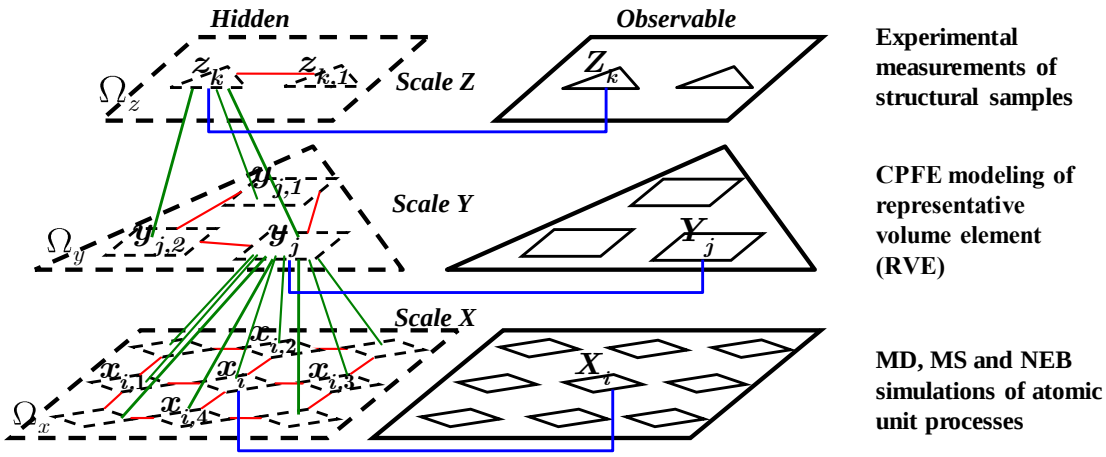

Figure 1.7 Multiscale hierarchical uncertainty in the modeling of heterogeneous nanostructured metals. The uncertainties arise at different scales/levels. The uncertainties from a lower level are passed to an upper level.

The General Hidden Markov Model[43] is used to quantify the uncertainties. Parametric study is conducted on the multiscale modeling. As illustrated in Figure 1.8, different parameters are input into simulations. For example, in MD simulations, the parameters are Burgers vector, slip plane, interatomic potential, and so on; in CPFE simulations, the parameters are constitutive relations, element sizes, and so on. Different input parameters result in different output properties from simulations, such as strengths, barriers and dislocation reactions. Uncertainty quantifications are performed based on the parametric study. The uncertainty analysis quantifies the difference between atomistic simulations, CPFE simulations and experiments. The microstructure uncertainties arise from the heterogeneities of microstructures and have effects on the strength-ductility properties. These microstructure uncertainties can lead to variation of material properties - a theme that I originally planned to study. In recent years, microstructure uncertainties are

being utilized to enhance the strength and ductility through engineering materials with gradient grains, transmdoal grains and 3D printed microstructures, etc. So my thesis research has been geared toward this emerging direction of heterogeneous microstructures that turn microstructure uncertainties into valuable features.

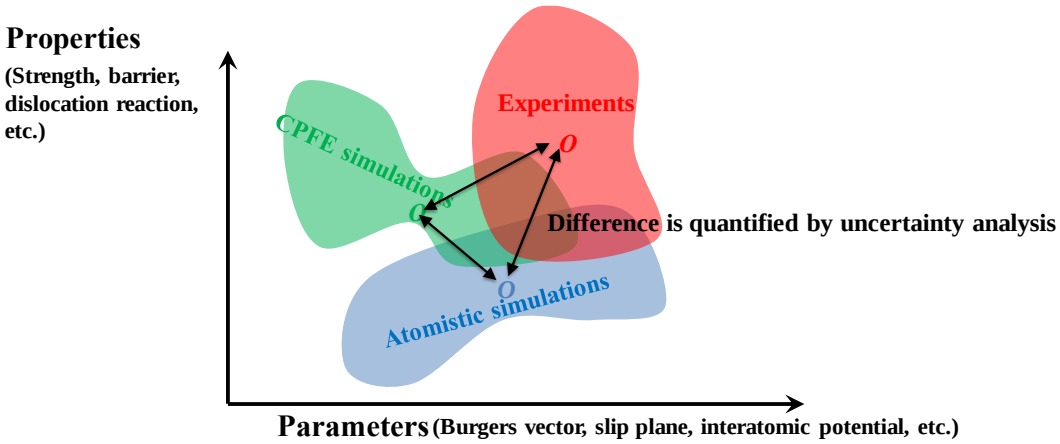

Figure 1.8 Uncertainty analysis quantifies the differences between predictions from different scales. The horizontal axis stands for the controllable input parameters for simulations at difference scales. The vertical axis stands for the output properties from simulations at different scales.

To practice this approach, five mechanical systems are studied. First, the mechanics of gradient nano-grained copper are studied by performing CPFE simulations. To understand the atomic deformation mechanisms, large scale MD simulations of gradient nano-grained copper are performed. Second, the strengths of transmodal grained aluminums are studied by performing CPFE simulation. Third, to understand the atomic failure mechanisms, MD simulation of fracture in nanotwinned copper are performed. Fourth, additively manufactured stainless steel are modeled with CPFE simulations. Fifth, to understand the atomic deformation mechanism in body-centred cubic metals, MD

simulations of nanoscale tungsten are performed. More detailed introduction on these topics are presented in the following sections.

1.2.1 Mechanics and deformation mechanisms of gradient nano-grained copper

The experimental works described in section 1.1 have shown either significantly enhanced mechanical properties or intriguing mechanical behaviors of GNG metals. However, the mechanics and deformation mechanisms of GNG metals remain little understood. While nanocrystalline metals with uniform grain sizes have been extensively studied in the past [10, 14, 44-47, 52-55], the available models of GNG metals are severely limited. Recently, Li et al. [56-58] used a multilayer structure with gradient properties to model the GNG metals and they employed a J_2-type plastic flow rule to account for the influences of grain size on yield strength and strain hardening. The associated numerical simulations examined the effects of gradient grains on strength, ductility and work hardening. However, the multilayer structures and phenomenological constitutive relations give an over-simplified representation of the highly heterogeneous microstructures and mechanical responses of GNG metals. Hence, there is a critical gap between the existing models and the complex mechanical behavior of GNG metals. Developing the mechanically based models is essential for understanding the mechanics and physics of GNG structures and for designing the high-performance GNG materials in the future.

In this thesis, we develop both crystal plasticity and atomistic models to investigate the mechanical behavior of GNG Cu. We build the GNG structures by adapting the conventional Voronoi tessellation method [59]. Such GNG structures are used for both crystal plasticity finite element and molecular dynamics simulations. We also extend the

classical crystal plasticity theory to incorporate grain-size-dependent constitutive relations. Crystal plasticity finite element and molecular dynamics simulations are performed to examine the effects of gradient grains on the mechanical behavior of GNG Cu. This work is presented in Chapter 2.

1.2.2 Strength and deformation mechanisms in transmodal grained aluminum

Nanocrystalline metals have high yield strength but low ductility. Heterogeneous grains by mixing small grains and large grains is one way to increase the ductility of nanocrystalline metals. In experiments, one kind of Al powders with an average sizes of 0.8μm and another kind of Al powders with an average sizes of 0.8μm are mixed together. The spark plasma sintering (SPS) technique has been used to sinter the mixed Al powders to prepare polycrystalline Al. During the SPS process, the grain growth is constraint. As a result, the polycrystalline Al has a combination of fine grains and coarse grains. The grains of different sizes are mixed. We call this material 'bimodal grained Al'.

Multiple kinds of Al powders with different averages sizes, gradually changing from small sizes to large sizes, are mixed together to prepare the polycrystalline Al. As a result, the polycrystalline Al has mixed grains gradually transiting from fine grains to coarse grains. The grains of different sizes are mixed.

To understand the deformation mechanisms bimodal grained Al and transmodal grained Al, we performed size-dependent crystal plasticity finite element (CPFE) simulations to investigate the effect of heterogeneous grains on the strength of bimodal grained Al and transmodal grained Al. We developed three dimensional model of heterogeneous grains with controllable sizes and distributions. We performed CPFE

simulations to simulate the uniaxial deformations of the bimodal grained and transmodal grained Al. The work is present in Chapter 3.

1.2.3 Fracture in a thin film of nanotwinned copper

Ultrafine grained copper with embedded nanoscale twin lamellas (hereafter referred to as nanotwinned Cu) exhibits an unusual combination of ultra-high strength (~ 1 GPa) and high tensile ductility (~14% elongation to failure) [23, 60-62]. However, most engineering applications would require the materials to have high fracture resistances as well [63]. Unlike the strength and tensile ductility that have been extensively studied [20, 54, 55, 64-69], the fracture behavior and associated microscopic mechanisms in nanotwinned metals are much less known.

Several recent studies have investigated the fracture in nanotwinned metals. Qin et al. [70] processed bulk coarse-grained Cu samples by dynamic plastic deformation and obtained a composite microstructure of nanoscale grains with embedded nanoscale twin bundles. They measured an enhanced fracture toughness relative to samples without nanotwins, and found that twin bundles caused the elongated deep dimples on fracture surfaces that contributed to an increase of fracture energy. Singh et al. [71] measured the fracture toughness and fatigue crack growth in nanotwinned Cu processed by electrodeposition, and showed that the presence of nanotwins enhanced both monotonic and cyclic crack growth resistances. Shan et al. [72] and Kim et al. [73] used the in situ transmission electron microscopy (TEM) to directly observe crack growth in nanotwinned Cu. Figure 1.9 shows the representative in situ TEM results of crack growth across twin groups in a thin foil of nanotwinned Cu [72]. It is seen from Figure 1.9(a) that a

characteristic zigzag crack path formed during tensile loading. Figure 1.9(b) presents magnified images of region 1 in Figure 1.9(a) showing the $\langle 110 \rangle_M$ and $\langle 110 \rangle_T$ crack edges in the adjoining matrix (M) and twin (T) crystals. Kim et al. [73] and Zhou and Qu [74] performed molecular dynamics (MD) simulations of fracture in thick nanotwinned samples. They observed the damage and fracture processes, including crack blunting through dislocation emission, crack bridging by twin lamella, crack deflection by grain boundaries, and nanovoid formation at the intersections between grain boundaries and twin boundaries.

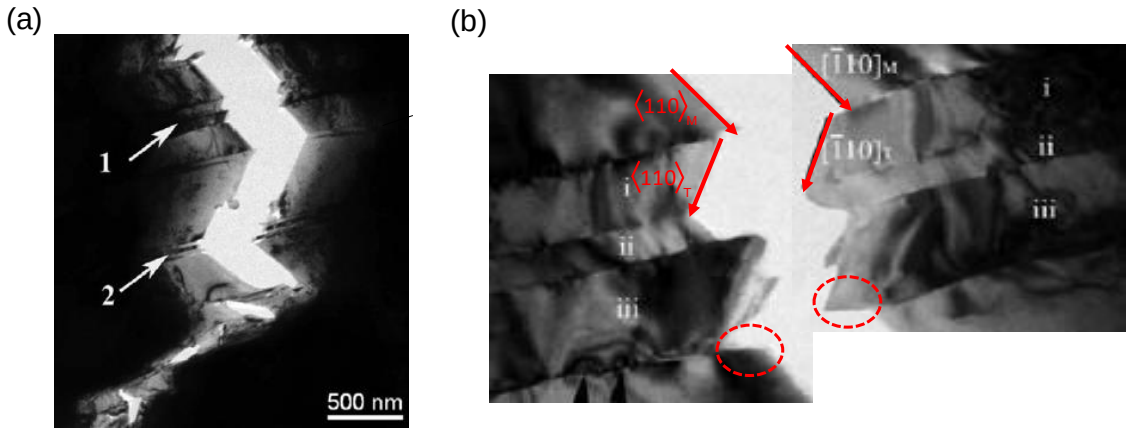

Figure 1.9 In situ TEM images of crack growth across twin groups in a thin foil of nanotwinned Cu, from a previous study by Shan et al. [72]. (a) A zigzag crack formed during tensile loading. (b) Magnified images of region 1 in (a), showing the $\langle 110 \rangle_M$ and $\langle 110 \rangle_T$ crack edges in the adjoining matrix (M) and twin (T) crystals. Circles indicate the short crack edges on twin boundaries.

The experimental and modeling studies discussed above suggest that the crack-twin boundary interactions can be beneficial to enhance fracture toughness. But the toughening mechanism associated with nanotwins are still little understood. Particularly, the following

questions have hitherto not been well addressed: What are the intrinsic fracture mechanisms in nanotwinned metals? How do twin boundaries affect crack propagation? The present work is motivated by previous in situ TEM observations [72, 73] and aims to address the above questions by studying the growth of a pre-crack in a free-standing thin film of nanotwinned Cu using MD simulations. Furthermore, MD simulations can directly reveal the underlying atomic-level processes of deformation and fracture, thereby shedding light onto the failure mechanisms of nanotwinned metals. This work is presented in Chapter 3.

1.2.4 Heterogeneity- and defect-controlled strength and deformation mechanisms in additively manufactured steels

Laser-based powder-bed-fusion (L-PBF) technology for additive manufacturing [75, 76] has recently gained considerable attention, due to its capability of directly building near full-density metal parts from a computer-aided design (i.e., a stereolithography file). L-PBF is being increasingly used as a facile and powerful additive manufacturing approach for a broad range of applications in aerospace, automobiles, and biomedical fields. Unlike conventional coarse-grained, ultrafine-grained or nanocrystalline metals, the additively manufactured (AM) material possesses a unique microstructure resulting from highly localized melting and fast cooling rates (~10^3-10^8 K/s) [75], leading to a set of mechanical properties that are drastically different from conventional counterparts. A current challenge in this field is to elucidate the strength scaling law as well as the controlling deformation mechanisms for AM materials [77-79].

Here we report that 316L stainless steels (SS) made by L-PBF can have hardness values that are over four times higher than that predicted from the H-P scaling law. The

strength-controlling grain sizes derived from the measured hardness values are nearly two orders of magnitude smaller than those measured from experiments. Such high hardness is in accordance with the high yield strength measured from uniaxial loading of AM 316L SS. The microstructural characterization and analysis of AM 316L SS reveal rather complex structural and chemical heterogeneities in these materials.

To further understand the deformation mechanisms of AM 316L SS, we performed *size-dependent* crystal plasticity finite element (CPFE) simulations to investigate the effects of grain-level heterogeneities as well as sub-grain heterogeneities and defects (e.g., local misorientations, cellular structures, dislocations, and LAGBs) on plastic responses. To gain further mechanistic insights into the strength-controlling sub-grain heterogeneities and defects, we performed molecular dynamics (MD) simulations of plastic deformation in a model of polycrystalline fcc steel (Fe-10Ni-17Cr). This work is presented in Chapter 4.

1.2.5 Deformation mechanisms in nanoscale body-centered cubic crystals

The past decade has witnessed a dramatic increase in the study of mechanical properties and deformation mechanisms in metallic nanostructures[34, 42, 60, 80, 81]. In this field, one prominent approach is to conduct *in situ* mechanical testing of nanostructures[81-88]. These real time experiments have revealed a wealth of novel deformation behaviors and size effects in various kinds of nanoscale crystals, including dislocation starvation[89], mechanical annealing[82], surface dislocation controlled yielding[84, 85], and twinning dominated deformation[90-92]. However, the majority of those results are obtained for FCC nanostructures. Given the widespread use of bulk BCC metals, BCC nanostructures are expected to play significant roles in future

nanotechnologies[93-95]. Hence it is natural to ask to what degree these phenomena and size effects in nanoscale FCC crystals still hold in BCC crystals.

One fundamental question regarding the deformation mechanism of metallic nanostructures is whether or not the material will deform via twinning[34, 96-98]. Deformation twinning is commonly observed in hexagonal-close packed (HCP) crystals[34, 83, 99, 100] but is much less common in bulk FCC and BCC crystals. Deformation twinning in these materials usually occurs under high strain rates or low temperatures[99, 101, 102], conditions that lead to high stresses. High stresses are readily achieved in nanoscale crystals[42, 81], resulting from the starvation of deformation carriers in these small crystals due to their large surface area to volume ratio. Such high stresses are thought to favor twinning even at room temperature and low strain rates, which can critically affect the mechanical properties such as strength and ductility of metallic nanostructures[34, 87, 92]. Recently, both *in situ* and *ex situ* nanomechanical experiments have revealed deformation twinning in FCC nanostructures, including Au nanowhiskers[90] and Cu nanowires[91]. In contrast, the mechanical testing of small-volume BCC crystals has only reported dislocation mediated plasticity, for example, in single crystalline W, Mo, Ta, Nb, V, Fe nanowires or nanopillars[86, 88, 103-106] and Mo alloy nanofibers[107]. In mechanical testing experiments where TEM analysis was not used, and thus dislocations were not observed, the deformation is still attributed to dislocation plasticity[108, 109]. Deformation twinning was reported in nanocrystalline Ta[110]; however, a close examination of this experiment shows that the observed twinning likely occurred in small grains of FCC Ta, instead of BCC Ta.

The lack of observation of deformation twinning in BCC nanostructures is

unexpected. In bulk BCC metals, deformation at room temperature is usually controlled by dislocations with high lattice resistances[88, 106, 111-115]. In small-scale BCC crystals, the large surface area tends to destabilize bulk dislocation sources, thus causing a reduction of dislocation density. It follows that a small number of bulk dislocations with low mobilities in BCC nanostructures may not be sufficient to accommodate the applied load. As a result, twinning may become necessary and even dominate the deformation at room temperature and low strain rates. To understand the competition between dislocation slip and deformation twinning in small-scale BCC metals, here we investigate the deformation behavior of nanoscale BCC tungsten (W) crystals using *in situ* nanomechanical testing with high resolution TEM (HRTEM). To achieve this, we develop a unique *in situ* welding process to fabricate the W nanowires. This method overcomes the difficulties of synthesizing sub-100 nm BCC samples without preexisting defects, in contrast to the commonly used sample preparation by the focused ion beam method which tends to create feature sizes larger than 100 nm as well as surface damage[82, 83, 88, 89]. Using these *in situ* fabricated samples, we demonstrate that twinning is the dominant deformation mechanism in nanoscale W crystals at room temperature and low strain rates. Such mechanical twinning is pseudoelastic, as evidenced by the reversible detwinning during unloading. We further find that the loading orientation governs the competition between twinning and dislocation slip. Atomistic simulations are performed to provide insights into the twinning dominated deformation mechanism in these nanoscale BCC crystals.

CHAPTER 2. MECHANICS AND DEFORMATION MECHANISMS OF GRADIENT NANO-GRAINED COPPER

In this Chapter, we develop both crystal plasticity and atomistic models to investigate the mechanical behavior of GNG Cu. Crystal plasticity finite element and molecular dynamics simulations are performed to examine the effects of gradient grains on the mechanical behavior of GNG Cu. In section 2.1, we provide an overview of crystal plasticity and atomistic models in terms of their unique and distinct features. Section 2.2 is focused on the methods and results of crystal plasticity finite element simulations, while section 2.3 molecular dynamics simulations for GNG Cu. We conclude in section 2.4 with a summary and outlook.

2.1 Overview of crystal plasticity and atomistic models

In this work, we employ both crystal plasticity finite element (CPFE) and molecular dynamics (MD) methods to study the mechanical behavior of GNG Cu. Figure 2.1 shows the CPFE and MD models of GNG Cu, featuring a gradient distribution of grain sizes. Built upon the conventional models of nanocrystalline metals with uniform grain sizes, we make the following new developments to model the GNG Cu. One is to generate the *gradient* grains through an adapted Voronoi tessellation method, thus providing realistic heterogeneous microstructures for CPFE and MD simulations. The other is to extend the classical crystal plasticity theory by incorporating the *grain-size-dependent* constitutive relations, thus allowing us to directly link the grain-level deformation properties and macroscopic constitutive responses. The details of these two developments, including

implementation within the simulation packages of ABAQUS/CAE [116] and LAMMPS [117], will be described in section 2.2.

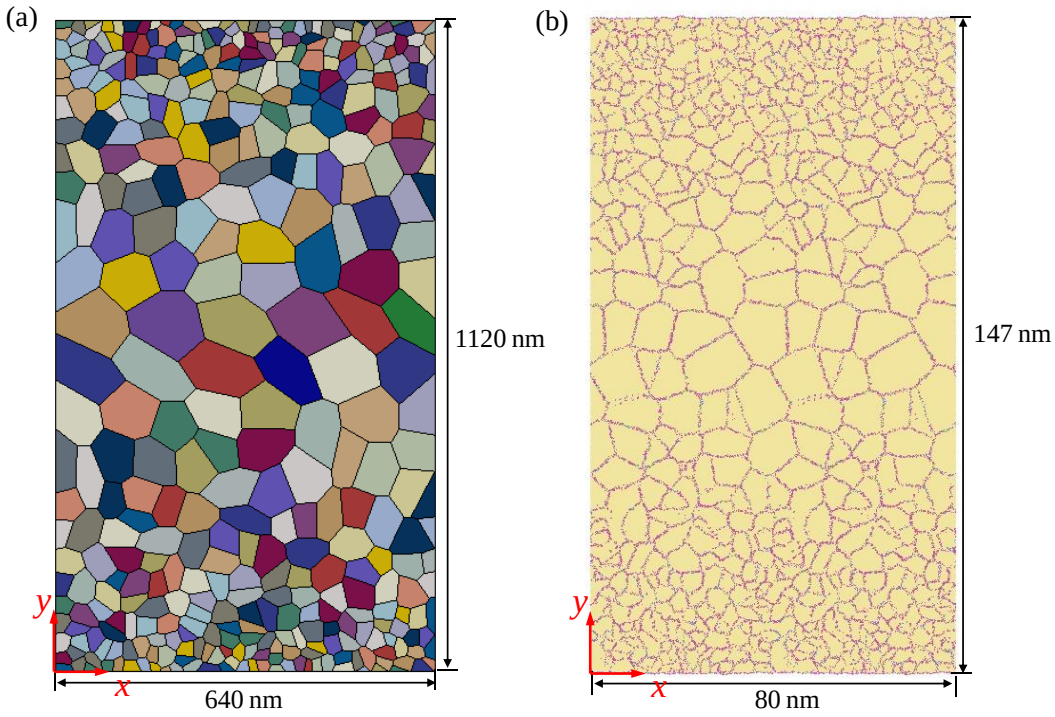

Figure 2.1 Overview of the crystal plasticity and atomistic models of GNG Cu, both of which consist of an assembly of quasi-2D columnar grains with gradient grain sizes. (a) Crystal plastic finite element model, where grain sizes vary from ~ 20 nm in the top/bottom surface layer to ~ 110 nm in the central region. Grains are colored randomly in ABAQUS/CAE. (a) Atomic structure of GNG Cu for molecular dynamics simulations, where grain sizes vary from ~ 2.5 nm in the top/bottom surface layer to ~ 10 nm in the central region. Atoms are colored in ATOMEYE [118] according to the coordination number (CN). Atoms in yellow (CN = 12) make up the perfect FCC lattice inside grains, while atoms in pink (CN = 11) are located at grain boundaries.

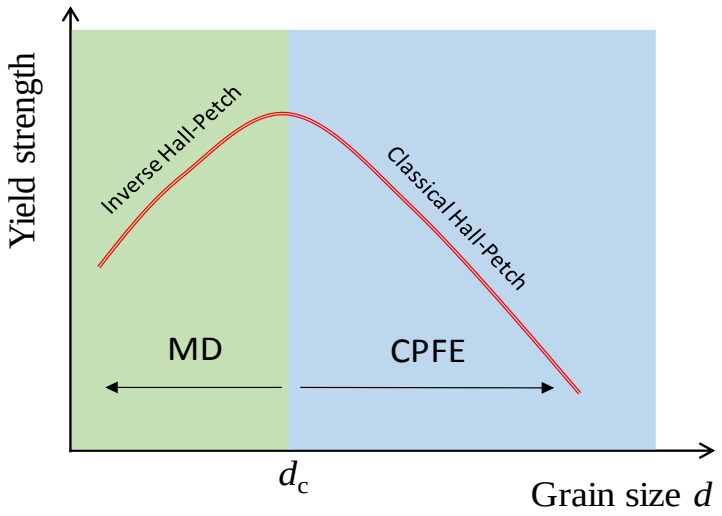

Figure 2.2 Schematic illustration of yield strength versus grain size d in polycrystalline metals with uniform grain sizes. There exists a critical gain size d_c that separates the classical Hall-Petch regime (i.e., smaller grain is stronger) with the inverse Hall-Petch regime (i.e., smaller grain is softer) [45, 52]. The CPFE and MD models are used to study GNG Cu in these two regimes, respectively.

It is important to note that our CPFE and MD models of GNG Cu cover two different regimes of grain size. Figure 2.2 shows a schematic illustration of yield strength versus grain size d in polycrystalline metals with uniform grain sizes. It is known that there exists a critical gain size d_c that separates the classical Hall-Petch regime (i.e., smaller is stronger) with the inverse Hall-Petch regime (i.e., smaller is softer) [45, 52]. The yield stress in the former is usually controlled by dislocation plasticity within grains, while that in the latter by grain boundary shear and migration [46, 52]. The critical grain size d_c is typically about 20 nm in FCC nanocrystalline metals [45, 52]. In our CPFE and MD studies, the range of grain sizes covered is dictated, on one hand, by the characteristic physical length scale in the model, and on the other hand, by the available computing resources, meaning that a more powerful computer would allow a larger size range for a

prescribed gradient of grain size. In our MD model of GNG Cu, the grain size varies from ~ 2.5 nm in the top/bottom surface layer to ~ 10 nm in the central region (Figure 2.1b). Hence, the plastic yielding and flow responses in MD fall into the inverse Hall-Petch regime. In contrast, the characteristic length scale in our CPFE models of GNG Cu is determined by the deformation mechanism - dislocation plasticity within grains - incorporated into the crystal plasticity constitutive relations. As such, our CPFE models fall into the classical Hall-Petch regime for grain sizes greater than 20nm; different ranges of gradient grain sizes are studied by our CPFE simulations.

2.2 Crystal plasticity finite element (CPFE) model

2.2.1 Grain-size-dependent crystal plasticity model

To model the constitutive response of GNG Cu, we extend the classical crystal plasticity theory by incorporating the grain size dependence of plastic yielding, strain hardening and rate sensitivity. The rate-dependent finite strain crystal plasticity theory adopted here can be traced to the works by Rice [119], Asaro and Rice [120], and Kalidindi et al. [121]. According to Kalidindi et al. [121], a polar decomposition of the deformation gradient tensor $\mathbf{F}$ is given by $\mathbf{F}^{*} \equiv \mathbf{F}\mathbf{F}^{p-1}$, where $\mathbf{F}^{*}$ is the elastic deformation gradient and $\mathbf{F}^{p}$ the plastic deformation gradient, with $\det \mathbf{F}^{p} = 1$ (plastic incompressibility). The stress in a single crystal is given by $\mathbf{T}^{*} = \mathbf{C}[\mathbf{E}^{*}]$, where $\mathbf{E}^{*} \equiv (1/2)\left\{\mathbf{F}^{*\mathrm{T}}\mathbf{F}^{*} - \mathbf{I}\right\}$ is an elastic strain measure, $\mathbf{C}$ is the fourth-order elasticity tensor. The stress measure $\mathbf{T}^{*}$ is related to the Cauchy stress $\mathbf{T}$ according to $\mathbf{T}^{*} \equiv \mathbf{F}^{*-1}\left[\left(\det \mathbf{F}^{*}\right)\mathbf{T}\right]\mathbf{F}^{*-\mathrm{T}}$. The rate of the plastic deformation gradient $\mathbf{F}^{p}$ is given

$$\dot{\mathbf{F}}^p = \mathbf{L}^p \mathbf{F}^p,\ \mathbf{L}^p = \sum_\alpha \dot{\gamma}^\alpha \mathbf{S}_o^\alpha,\ \mathbf{S}_o^\alpha \equiv \mathbf{m}_o^\alpha \otimes \mathbf{n}_o^\alpha \tag{2.1}$$

where $\mathbf{m}_o^\alpha$ and $\mathbf{n}_o^\alpha$ are orthonormal unit vectors which define, respectively, the slip direction and slip plane normal of the slip system α in a fixed reference configuration, and $\dot{\gamma}^\alpha$ is the plastic shearing rate on this slip system.

The plastic shearing rate on the slip system α is

$$\dot{\gamma}^\alpha = \dot{\gamma}_o \left| \frac{\tau^\alpha}{s^\alpha} \right|^{1/m} \operatorname{sign}\left(\tau^\alpha\right), \tag{2.2}$$

where $\tau^\alpha \approx \mathbf{T}^* \cdot \mathbf{S}_o^\alpha$ is the resolved shear stress, s^α is the slip resistance for the slip system α, $\dot{\gamma}_o$ is the reference shearing rate, and m is the strain rate sensitivity parameter. The initial value of s^α is denoted as s_0. During plastic deformation, the slip resistance s^α evolves according to

$$\dot{s} = \sum_\beta h^{\alpha\beta} \left| \dot{\gamma}^\beta \right|,\ h^{\alpha\beta} = q^{\alpha\beta} h^{(\beta)},\ h^{(\beta)} = h_0 \left(1 - s^\beta / s_{\text{sat}}\right)^a \tag{2.3}$$

where $q^{\alpha\beta}$ are the components of a matrix which describes the latent hardening behavior of the crystal, and h_0, a and s_{sat} are hardening parameters which are taken to be identical for all slip systems.

Our crystal plasticity model is grain-size-dependent. For each grain, the slip resistance parameters, including $\{s_0, h_0, a, s_{\text{sat}}, m\}$, are taken as functions of grain size d [47, 122]. In line with the macroscopic Hall-Petch relation [123, 124], which states that

the yield strength is inversely proportional to the square root of grain size, we assume all the slip resistance parameters to be inversely proportional to the square root of grain size,

$$\left\{s_0(d), h_0(d), a(d), s_{\text{sat}}(d), m(d)\right\} \sim d^{-1/2} \tag{2.4}$$

The numerical values for the grain-size-dependent initial slip resistance s_0 are readily estimated from the available experimental data in the literature, but the determination of the strain hardening related parameters $\{h_0,\ a,\ s_{\text{sat}}\}$ requires certain assumptions. Specifically, the initial values of slip resistance s_0 are determined based on the experimentally measured yield stresses of NG Cu with uniform grain size *d*, i.e., from 860 MPa to 400 MPa for *d* from 20 nm to 110 nm [10, 53]. Dividing these macroscopic yield stresses by Talyor's factor of 3, we estimate the corresponding slip resistance s_0 in between 286 MPa and 133MPa. The NG Cu shows little hardening in experiments. However, we assign small values of $\{h_0,\ a,\ s_{\text{sat}}\}$, so as to produce a weak hardening for facilitating numerical stability in CPFE simulations. For the 20 nm grain, we take h_0 = 102 MPa, a = 2.0, s_{sat} = 600 MPa; and for the 110 nm grain, h_0 = 48 MPa, a = 1.8, s_{sat} = 287 MPa. Furthermore, experiments show that the strain rate sensitivity *m* of NG Cu with uniform grain size vary from 0.4 and 0.022 for *d* from 20 nm to 110 nm [125]. To evaluate the slip resistance parameter such as s_0 for intermediate grain sizes, we use the above bounding values to fit the formula of $s_0 = B + C \cdot d^{-1/2}$ where B and C are the fitting constants. Along the same line, we also fit other slip resistance parameters of $\{h_0,\ a,\ s_{\text{sat}}, m\}$. All the fitting formulas are obtained as follows:

$$s_0(\text{MPa}) = 19.3 + 1196 \cdot d^{-1/2},\ h_0(\text{MPa}) = 8.68 + 415.8 \cdot d^{-1/2}, \tag{2.5}$$

$$a = 1.65 + 1.56 \cdot d^{-1/2},\ s_{\text{sat}}(\text{MPa}) = 53.7 + 2443 \cdot d^{-1/2},\ m = 0.0086 + 0.1403 \cdot d^{-1/2}$$

Figure 2.3 shows the curves of slip resistance s versus plastic shear γ for several representative grain sizes between 20 nm and 110 nm.

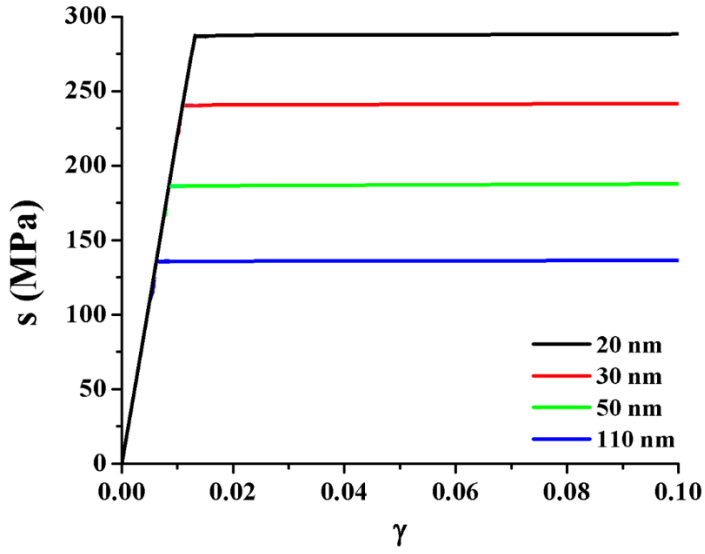

Figure 2.3 Slip resistance versus plastic shear strain for various grain sizes from 20 nm to 110 nm.

Other material properties, including elastic constants (C_{11}, C_{12}, C_{44}), slip systems ($\mathbf{m}_o^\alpha$, $\mathbf{n}_o^\alpha$), and the latent hardening matrix $\{q^{\alpha\beta}\}$, are assumed to be independent of grain size. For FCC Cu, we take $C_{11} = 170$ GPa, $C_{12} = 124$ GPa and $C_{44} = 75$ GPa; twelve

$\{111\}\langle 110\rangle$ slip systems for ($\mathbf{m}_o^\alpha$, $\mathbf{n}_o^\alpha$); $q^{\alpha\beta}$ = 1.0 if the slip systems α and β are coplanar and $q^{\alpha\beta}$ = 1.4 if they are non-coplanar [121].

2.2.2 Finite element model

To prepare for CPFE simulations of GNG Cu, we first construct a two-dimensional GNG structure with columnar grains by adapting the Voronoi tessellation method in Matlab. The construction begins with a layered rectangular structure with gradient thickness. Each layer is divided into grains with the average size being equal to the layer thickness. That is, the number of grains in each layer equals to the layer length divided by its thickness, so that the average grain shape is square, giving equi-axial grains. For each grain, the horizontal position of its centroid is randomly assigned and the vertical position is located at the middle of the layer. After all the grain centroids are assigned in all the layers, the Voronoi tessellation is applied (with a built-in function voronoi command in Matlab) to construct the Voronoi diagram. Each Voronoi cell is a polygon with an irregular shape, representing a grain in the GNG structure. The geometrical information of the GNG structure is used to develop the corresponding finite element model in ABAQUS/CAE by using a Python script.

Figure 2.1(a) shows an example of the GNG structure rendered in ABAQUS/CAE. In this case, the grain size gradually increases from ~ 20 nm in the top/bottom surface layer to ~ 110 nm in the central region. Hence, grain sizes in the GNG sample fall into the Hall-Petch regime, as discussed in section 2.1. The overall sample geometry is 640 nm in length and 1120 nm in width. The sample is meshed with non-structured plane strain elements. As a result, most elements have four nodes (CPE4R) and a small fraction three nodes

(CPE3). Displacements and tractions are continuous at grain boundaries, meaning no separation or sliding between every pair of adjoining grains. Using the GNG structure in Figure 2.1(a), CPFE simulations are performed to investigate the axial tensile behavior of GNG Cu under the plane-strain condition.

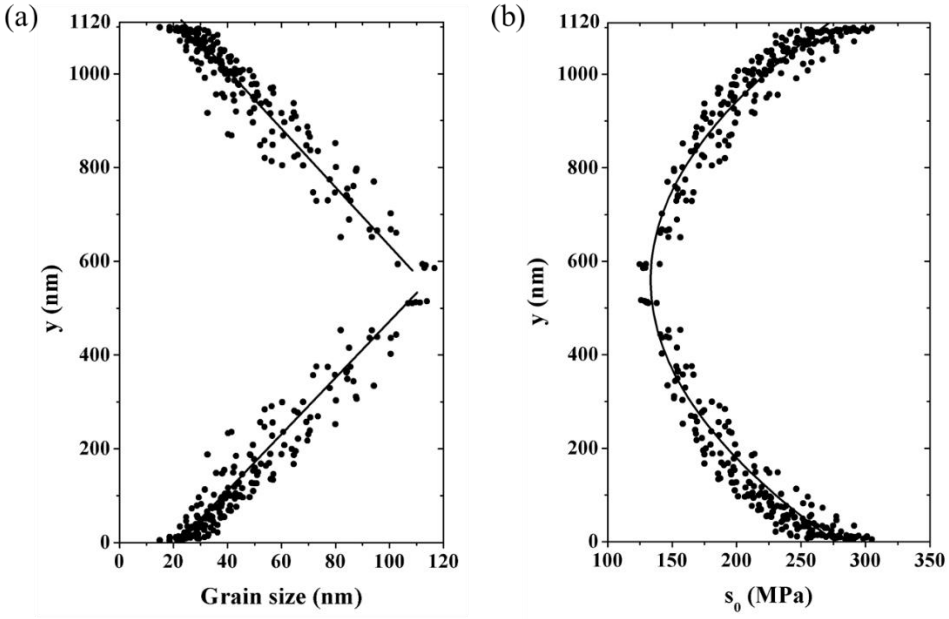

Figure 2.4 Distributions of (a) gradient grain sizes and (b) grain-level slip resistances in the cross section of a CPFE-simulated GNG sample, as shown in Figure 2.1(a). The data point represents (a) the size and (b) the slip resistance of a grain. The solid line is the fitting curve.

Figure 2.4(a) shows the gradient distribution of grain sizes along the cross section (y axis) of the GNG sample. The orientation of grains is assigned randomly in terms of three Euler angles, $\{\theta, \varphi, \Omega\}$, representing rotation from the crystal basis to the global basis [121]. A user material subroutine VUMAT is developed in ABAQUS/EXPLICIT to

implement the grain-size-dependent crystal plasticity model described in section 2.2.1. As such, all the slip resistance parameters at each integration point depend on the local grain size according to Equation (2.5). As an example, Figure 2.4(b) shows the gradient distribution of initial slip resistance s_0 along the cross section. With reference to Figure 2.1(a), the boundary conditions of the GNG sample are prescribed as follows: the upper and lower surfaces are traction free; on the left side (x = 0), the displacement in the x direction is zero (u_x = 0); on the right side (x = 640 nm), the velocity in the x direction is constant (v_x = 0.64 nm/s), corresponding to an applied tensile strain rate of 0.001/s.

2.2.3 CPFE simulation results

2.2.3.1 Grain-size-dependent yield strength

Figure 2.5 shows CPFE simulation results of GNG Cu using the grain-size-dependent crystal plasticity model described in section 2.2.2. Recall that the GNG structure simulated is shown in Figure 2.1(a), which consists of gradient grains with the size range of 20 - 110 nm in the Hall-Petch regime. Figure 2.3 shows the slip resistance as a function of plastic shear strain for several representative grain sizes. We assume no strain hardening at the grain level. Figure 2.5(a) presents the simulated stress-strain curve for the GNG Cu sample subjected to axial tension under the plane-strain condition. Deformation begins with a linear elastic regime. When the elastic strain rises to about 0.27%, the GNG Cu sample starts to yield, i.e., deviation from the linear stress-strain response, at about 390 MPa. Further straining causes a smooth, gradual increase of the axial tensile stress. Such a gradual yielding behavior can be attributed to progressive attainment of yield strengths in grains with different orientations and, more importantly, with different sizes giving

different slip resistances. When the tensile strain reaches about 0.5%, the entire GNG Cu sample yields and the stress-strain curve attains a plateau of about 510 MPa.

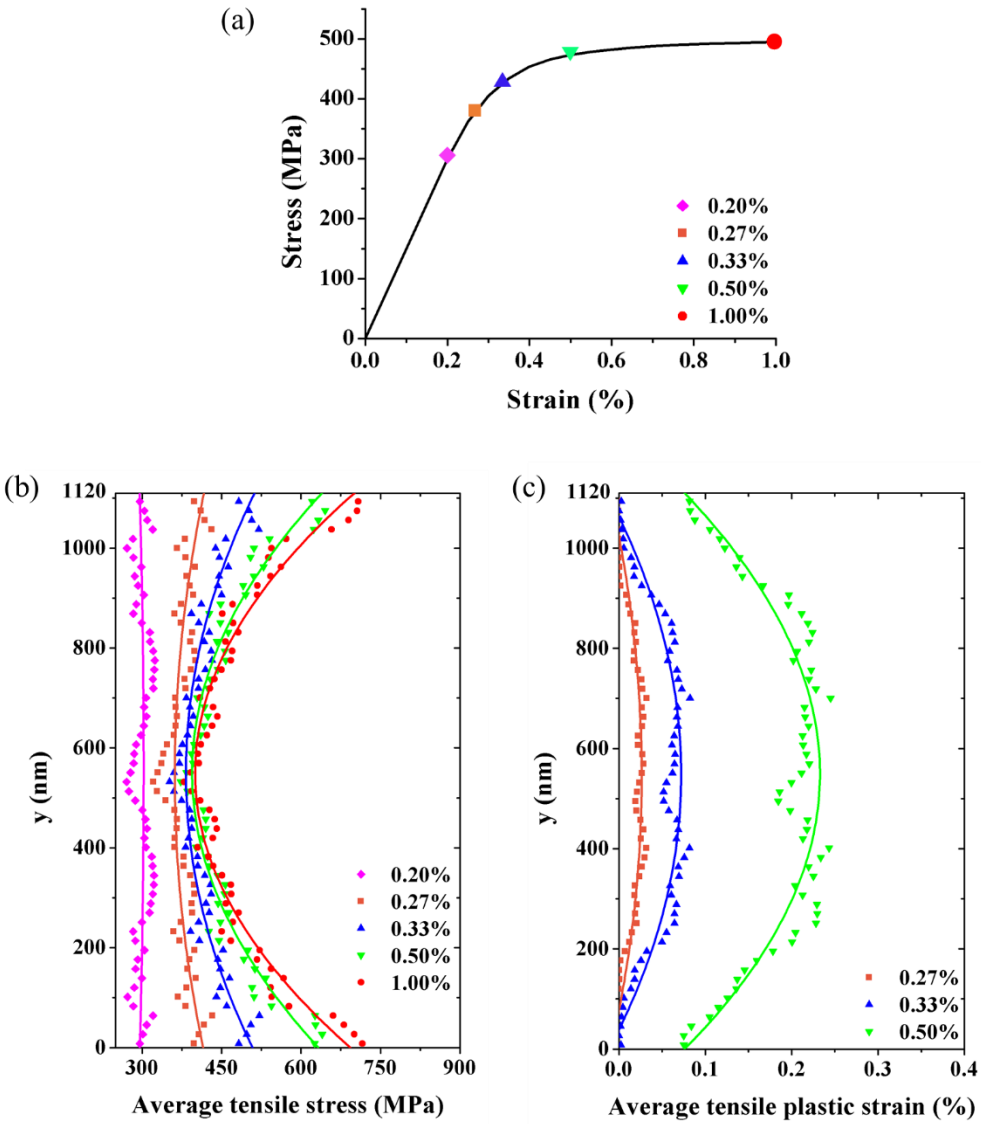

Figure 2.5 CPFE simulation results of GNG Cu subjected to axial tensile loading. (a) Overall stress-strain curve. Gradient distributions are revealed for both (b) tensile stresses and (c) tensile plastic strains in the cross section at various applied strains as marked in (a).

Importantly, our CPFE simulation reveals the novel gradient distributions of both stress and plastic strain in the cross section of GNG Cu, which arise due to progressive yielding of grains with gradient sizes. In Figure 2.5(b), we plot the distributions of tensile stress in the sample cross section at various applied strains of 0.2%, 0.27%, 0.33%, 0.5% and 1%. To generate these plots, we divide the GNG Cu sample into 60 slabs in the *y* direction and then calculate the average of nodal axial stresses in each slab. As such, the data points in Figure 2.5(b) correspond to the calculated average tensile stresses at different locations of the cross section and the solid lines are the fitting curves. It is seen that at small applied strains, the distribution of axial stresses in the cross section is nearly uniform, e.g., the pink curve at a strain of 0.2%. This is because all the grains undergo elastic deformation and the linear elastic constitutive relation is independent of grain size. As the applied strain continues to increase, large grains in the central region of the cross section begin to yield, causing a drastic slowdown of increase of axial stresses in the central region. In contrast, small grains near the surface continue the elastic deform, resulting in a more pronounced increase of axial stresses near the surface. Due to the gradient distribution of grain sizes between the central and surface regions, the cross-sectional stress exhibits a smooth gradient distribution, e.g., the blue curve at a strain of 0.33%. Such a gradient stress distribution evolves as the applied strain increases, e.g., the green curve at a strain of 0.5%. Meanwhile, the plastically yielded domain gradually expands from the central region to the surface within the cross section of the sample. Finally, the entire GNG sample yields and the gradient stress distribution is fully developed without further changes with increasing applied strain load, e.g., the red curve at a strain of 1%. This stage corresponds to the plateau of the stress-strain curve in Figure 2.5(a).

In addition to the gradient stresses, our CPFE simulation reveals the gradient plastic strains in GNG Cu. In Figure 2.5(c), we plot the distributions of the accumulated tensile plastic strains in the sample cross section at various applied strains of 0.27%, 0.33%, and 0.5%, evaluated using the same scheme for averaging the stresses in the cross section. Similar to the gradient stresses, the gradient distribution of plastic strain is caused by progressive yielding of grains with gradient sizes. We note that the distribution of plastic strains exhibits the maximum in the center where large grains first attain the yield points and the minimum at the surface where progressive yielding arrives the latest. Hence, the gradient variation of axial plastic strains is opposite to that of axial stresses, as seen from Figure 2.5(b) and (c). More interestingly, the gradient plastic strains arise under an overall uniform deformation of the GNG samples, and they stand in contrast to the widely studied strain-gradient plasticity induced by applying non-uniform deformations such as torsion [126], bending [127], and indentation [128]. The plastic strain gradient signifies the plastically inhomogeneous deformation that can provide a non-local effect of material strengthening [129], which is additional to the strengthening generated by local plastic strains. In this work, we will not further quantitatively evaluate the additional strengthening effect of gradient plastic strains, due to a lack of related experimental characterization and data. Nonetheless, the gradient plastic strain arising from gradient grain sizes represents a new material strengthening mechanism due to non-homogenous plastic deformation and warrant a systemic study in the future.

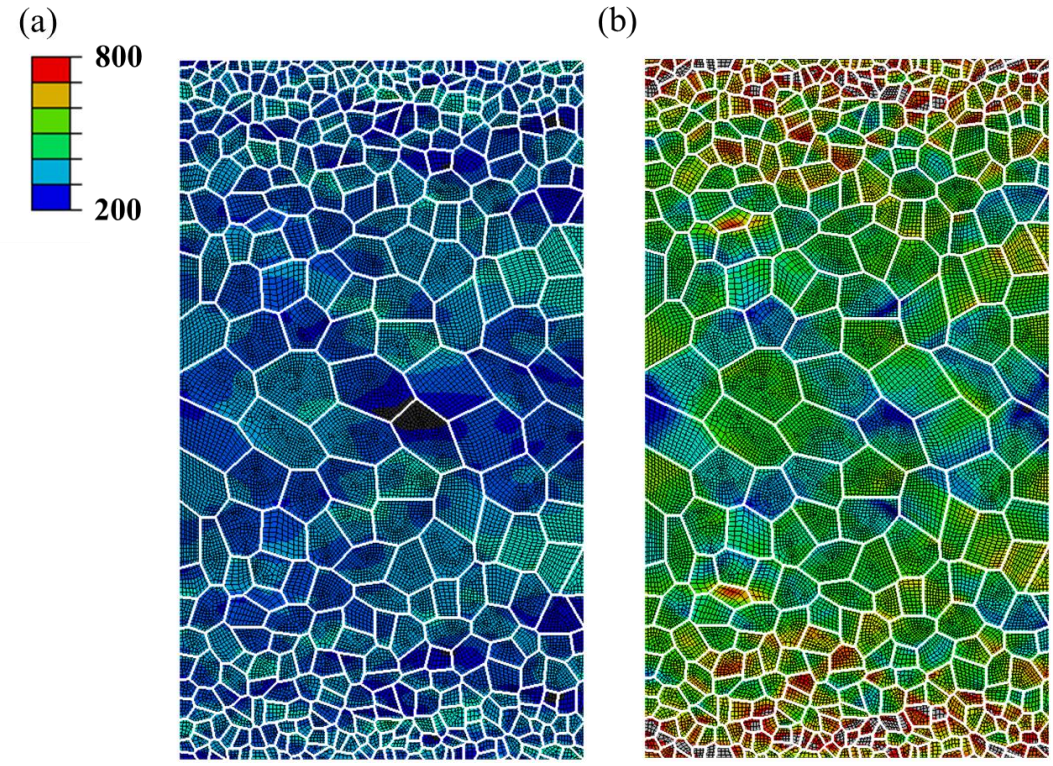

Figure 2.6 Contours of the axial stress at the applied strain load of (a) 0.2% and (b) 1%. Scale bars are in the unit of MPa.

To further understand the gradient distributions of stress and plastic strain in the cross section of GNG Cu, we plot in Figure 2.6 the contours of axial stresses at two different applied strains, showing the evolving spatial distribution of gradient stresses. When the applied strain load is low, deformation of gradient grains is elastic. At a representative axial strain of 0.2%, the spatial stress distribution in Figure 2.6(a) is nearly uniform, consistent with the plot of the cross-sectional stress distribution (e.g., the pink curve) in Figure 2.5(b). As the applied strain load is increased, a stress gradient develops in the cross section due to progressive yielding in gradient grains. At an applied strain of 1%, the spatial stress distribution in Figure 2.6(b) is clearly gradient, consistent with the

plot of the average stress distribution (e.g., the blue curve) in Figure 2.5(b). Both Figure 2.6(a) and (b) also show the inhomogeneous spatial distribution of stress in grains with similar sizes, i.e., located at a similar distance to the top/bottom free surface. Such inhomogeneities can be primarily attributed to the random distributions of grain orientations and partly to the small variation of grain sizes. In addition, we plot in Figure 2.7 the contours of the accumulated axial plastic strain at two intermediate applied strain loads, which exhibit the progressive yielding responses: larger, inhomogeneous plastic strains have been accumulated in the central region, and smaller, inhomogeneous plastic strains in the top/bottom surface layers.

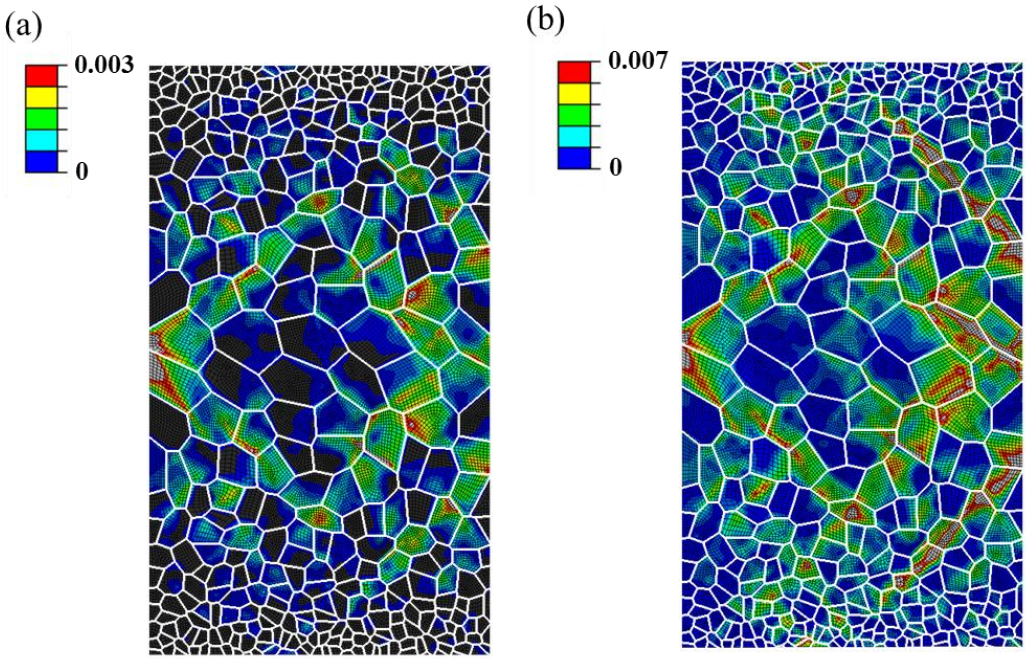

Figure 2.7 Contours of the plastic strain at the applied strain load of (a) 0.33% and (b) 0.5%. Scale bars are in the unit of MPa.

2.2.3.2 Grain-size-dependent strength and hardening

When nano-grains fall in the size range of tens of nanometers, strain hardening is typically weak. However, as nano-grains are greater than 100 nm, strain hardening increases with grain size [10]. To explore the effects of strain hardening on GNG metals, we perform CPFE simulations accounting for the grain size dependence of both yield strength and strain hardening. We still use the GNG Cu structure in Figure 2.1(a), but it now represents gradient grains in the size range of 100 - 550 nm, as opposed to the size range of 20 - 110 nm simulated in section 2.2.3.1. The corresponding grain-size-dependent constitutive relations at the grain level are prescribed as follows:

$$s_0(\text{MPa}) = 19.3 + 1196 \cdot d^{-1/2},\ h_0(\text{MPa}) = 17358 - 172570 \cdot d^{-1/2}, \tag{2.6}$$

$$a = 3.19 - 13.95 \cdot d^{-1/2},\ s_{\text{sat}}(\text{MPa}) = -38.76 + 3254 \cdot d^{-1/2},\ m = 0.0086 + 0.1403 \cdot d^{-1/2}$$

In Equation (2.6), the slip resistance s_0 and rate sensitivity m are taken from the available experimental data [10, 53], and other strain hardening parameters are assigned to produce the grain-size-dependent strain hardening. In Figure 2.8(a), we plot the slip resistance as a function plastic shear strain for several representative grain sizes based on Equation (2.6). Larger grains exhibit lower yield strengths, but stronger hardenings. As a reference, we also simulate the GNG Cu in the same size range of 100 - 550 nm, with grain-size-dependent yield strength but without strain hardening. The corresponding slip resistance parameters as a function plastic shear strain is prescribed by Equation (2.5), and the associated curves for s_0 are plotted in Figure 2.8(b) for several representative grain sizes. Figure 2.8(c) shows the simulated tensile stress-strain curve for both cases. In the

case of the GNG Cu without grain-level strain hardening, the overall stress-strain response (red curve) in Figure 2.8(c) is similar to the earlier result in Figure 2.5(a), as both involve the perfectly plastic grains, but represent different ranges of grain sizes. A notable difference is the lower plateau of flow stress in Figure 2.8(c) relative to that in Figure 2.5(c), which arises due to the smaller slip resistances in larger grains.

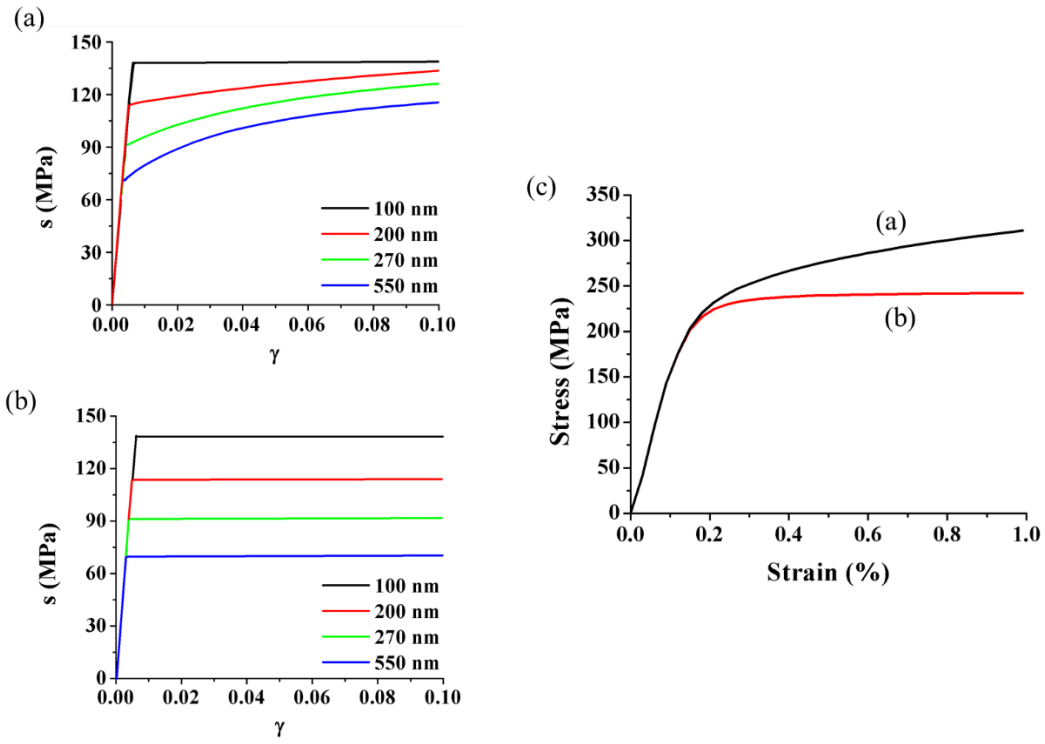

Figure 2.8 Effect of the grain-level strain hardening on the overall stress-strain response. (a) Slip resistance versus plastic shear strain for grain sizes from 100 nm to 500 nm, showing grain-size-dependent strain hardening. (b) Same as (a), but without strain hardening. (c) Overall stress-strain curves that respectively correspond to the grain-level slip resistances prescribed in (a) (black curve) and (b) (red curve).

However, in the case of the GNG Cu with grain-level strain hardening, the overall stress-strain response (black curve) in Figure 2.8(c) exhibits a pronounced strain hardening, which represents the collective response of nano-grains with grain-size-dependent strain hardening. Incidentally, high strain hardening is a desirable material characteristic that can promote uniform tensile plastic deformation and thus prevent premature plastic instability such as necking and rupture [7]. Our GNG model with grain-size-dependent strain hardening demonstrates an appealing opportunity of tailoring grain-level strain hardening for achieving the desired overall strain hardening in GNG structures. Such a material design route requires the integrated experimental and modeling study in the future.

Moreover, we compare in Figure 2.9 the distributions of the cross-sectional stresses in GNG samples with and without grain-level strain hardening. In both Figure 2.9(a) and (b), the gradient stresses start to develop as the central regions attain the respective yield points, see for example the orange curves in both figures at the applied strain of 0.2%. However, in Figure 2.9(a), both the magnitude of stress and stress gradients in the cross section increase markedly with increasing applied strain loads, owing to the strong strain hardening at the grain level. In contrast, the corresponding changes in Figure 2.9(b) are much weaker, due to a lack of grain-level strain hardening. Hence, these results demonstrate that tailoring the strain hardening characteristics at the grain level in GNG structures can yield different spatial distributions of stresses and stress gradients, which might enable a further control of surface-initiated fracture and fatigue in GNG materials.

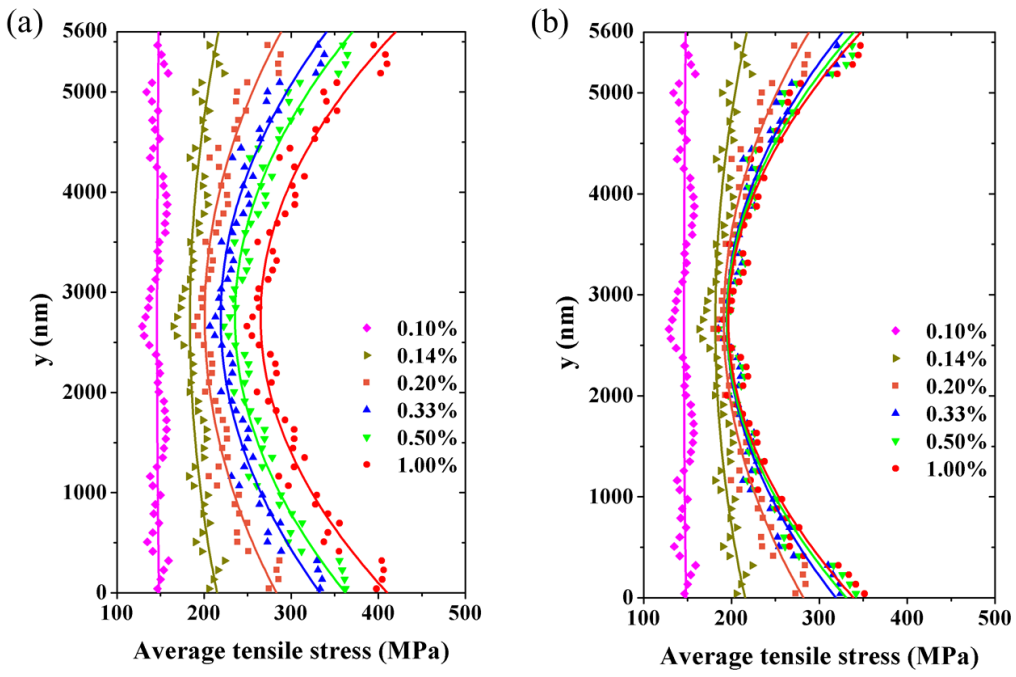

Figure 2.9 Effects of the grain-level strain hardening on the stress distribution in the cross section of GNG samples. (a) Distribution of cross-sectional tensile stresses at various applied strains when strain hardening is grain-size-dependent (corresponding to Figure 2.8(a)). (b) Same as (a) except that the grain-level strain hardening is absent in the crystal plasticity model (corresponding to Figure 2.8(b)).

2.3 Atomistic modeling

2.3.1 Molecular dynamics (MD) setup

In addition to CPFE studies, we perform MD simulations of GNG Cu using LAMMPS, in order to understand the competing deformation mechanisms. An embedded atom method (EAM) potential of Cu is used [130]. Similar to the CPFE simulation, we first generate a quasi-two-dimensional GNG structure with columnar grains using the adapted Voronoi tessellation method in Matlab. Then we cut the single crystal lattice of FCC Cu into polygons for fitting into different grain domains of the GNG structure. In the resulting

GNG sample for MD simulation, the thickness direction of each grain is aligned with <112> , but the in-plane orientation is randomly assigned. Hence the GNG sample has the <112> texture. The sample is relaxed in LAMMPS for 7000 ps at the temperature of 300 K and zero stresses using a Nose-Hoover thermostat and barostat. This process eliminates a most of the unfavorable features in grain boundaries with high energies. As a result, many initial faceted grain boundaries become curved for accommodating the local structure incompatibilities between adjoining grains. Displacements of triple junctions and associated changes of dihedral angles are also observed due to the concerted movement of grain boundaries connected at a shared triple junction.

The relaxed atomic structure of GNG Cu, rendered by ATOMEYE [118], has been shown in Figure 1(b). In this GNG sample, the grain size varies from ~ 2.5 nm in the top/bottom surface layer to ~ 10 nm in the central region. These grain sizes fall into the inverse Hall-Petch regime, which is further confirmed by our MD simulations, to be discussed next. Overall, the MD sample has an in-plane dimension of 80 nm × 147 nm, and is 1.8 nm in thickness. It should be noted that the actual GNG sample used in our MD simulations is shown in Figure 2.10(a), since we take half of the model shown in Figure 1(b) for saving the computation time. As such, the total number of atoms in the system of Figure 2.10(a) is 869,536 and the total number of grains is about 720. The top and bottom surfaces are traction free, while the sample thickness is fixed, corresponding to the plain-strain condition. Periodic boundary conditions are imposed in the *x* and thickness directions. Grains across the right and left edges of the simulation box are carefully constructed to avoid artificial boundaries on these edges that are potentially caused by periodic boundary conditions. A tensile strain rate of $5\times10^{7}/s$ is applied in the *x* direction.

The MD time step is 1 fs. The system temperature is maintained at 300 K using the Nose-Hoover thermostat.

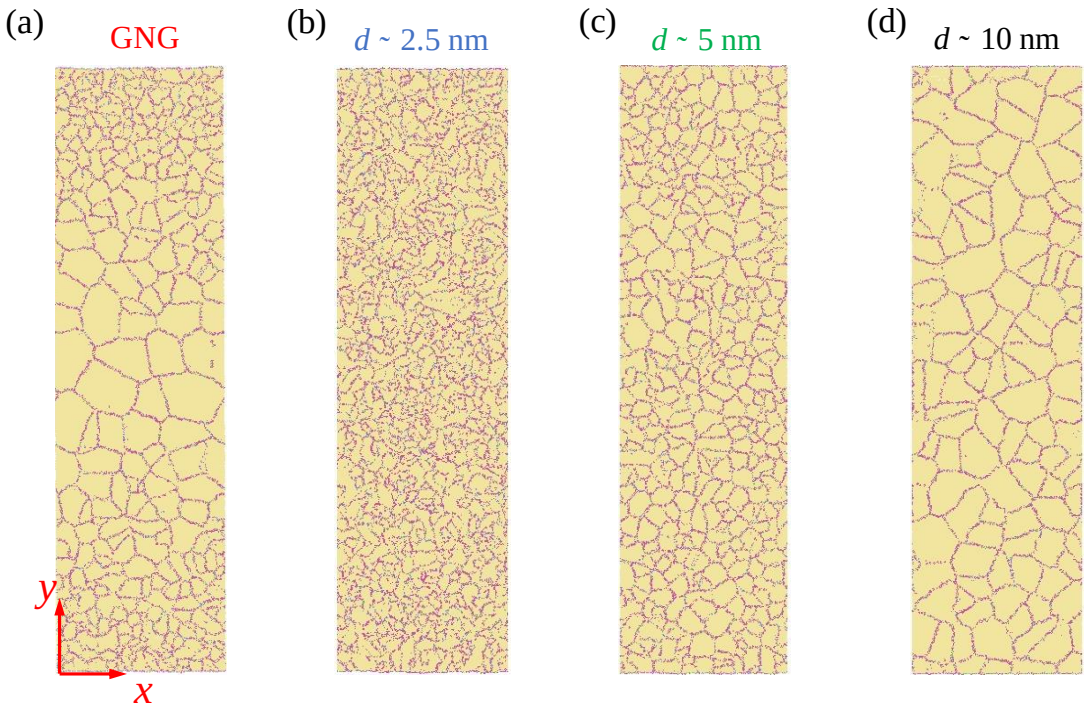

Figure 2.10 Atomic structures of GNG and NG Cu before loading. (a) GNG Cu with gradient grain sizes. (b-d) NG Cu with uniform grain sizes; the average grain size *d* is about (b) 2.5 nm, (c) 5 nm and (d) 10 nm. Atoms are colored by the coordination number, same as Figure 1(b).

MD simulations are also performed for NG Cu with uniform grain sizes. Figure 2.10(b-d) show the corresponding atomic structures where the average grain size *d* is about 2.5 nm, 5 nm and 10 nm, respectively. These NG samples have the same overall dimension as the GNG sample in Figure 2.10(a). The total numbers of atoms in NG samples are 869,632 ($d \sim 2.5$ nm), 869,860 (5 nm) and 869,608 (10 nm), respectively. The total numbers

of grains are 2,162 (d ~ 2.5 nm), 572 (5 nm), 157 (10 nm), respectively. The boundary conditions, loading rate, time step and temperature for NG Cu are identical to those for GNG Cu.

2.3.2 MD simulation results

2.3.2.1 Mechanics of GNG and NG

Figure 2.11 shows MD-simulated stress-strain curves, including the GNG Cu with gradient grain sizes and NG Cu with uniform grain sizes. All the stress-strain curves exhibit an initial elastic response and then attain plastic yielding without a pronounced yield drop. As the applied strain load is further increased, the GNG Cu and NG Cu (including d ~ 10 nm and 5nm) exhibit a stress plateau with negligible strain hardening, while the NG Cu with d ~ 2.5 nm a gentle strain hardening. Comparing the three stress-strain curves of NG Cu with uniform grain sizes, we observe the behavior of "smaller is softer". Defining the yield stress from 1% strain offset, we estimate the respective yield stress of NG Cu for d ~ 10 nm, 5 nm and 2.5 nm as 1.9 GPa, 1.6 GPa, and 1.3 GPa, thereby confirming the behavior of "smaller is softer" for NG Cu. Hence, the grain size range of 2.5 - 10 nm studied for both NG and GNG samples by the present MD simulations fall into the inverse Hall-Petch regime. This result also has implications for the strength/rate-controlling deformation mechanisms in MD simulations, to be discussed next. In addition, we note that the characteristic tensile stresses in the GNG sample (the red curve in Figure 2.11), including yield stress and flow stress plateau, are closer to those of the NG sample with the average grain size of 10 nm. This result is understandable because of the relatively large volume fraction of big grains (close to 10 nm) in the GNG sample as seen in Figure 2.10(a).

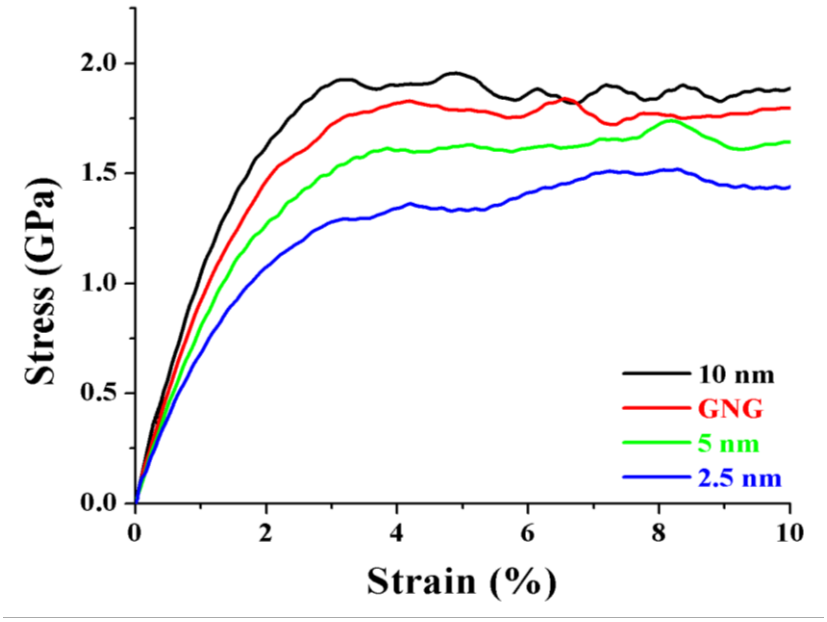

Figure 2.11 MD-simulated tensile stress-strain curves for the GNG Cu with gradient grain sizes (red) and NG Cu with uniform grain sizes, including cases with the average grain size of 10 nm (black), 5 nm (green) and 2.5 nm (blue).

Figure 2.12 shows the distribution of average tensile stresses in the cross section of a MD- simulated GNG Cu at different applied strains. Similar to the CPFE results, the cross-sectional stress is uniform at low strain loads because the elastic properties are independent of grain size; as the applied strain load is increased, a gradient stress distribution develops due to progressive yielding of nano-grains with gradient sizes. However, nano-grains in MD simulations exhibit the "smaller is softer" behavior in the inverse Hall-Petch regime, as shown in Figure 2.11. These results indicate that in the GNG sample, the smaller nano-grains in the surface region should typically attain plastic yielding earlier than the larger grains in the central region. This leads to a gradual increase of stress from the surface to the center, which is opposite to the sign of stress gradient from CPFE

simulations of the GNG Cu with grain size in the Hall-Petch regime, as shown in Figure 5(b).

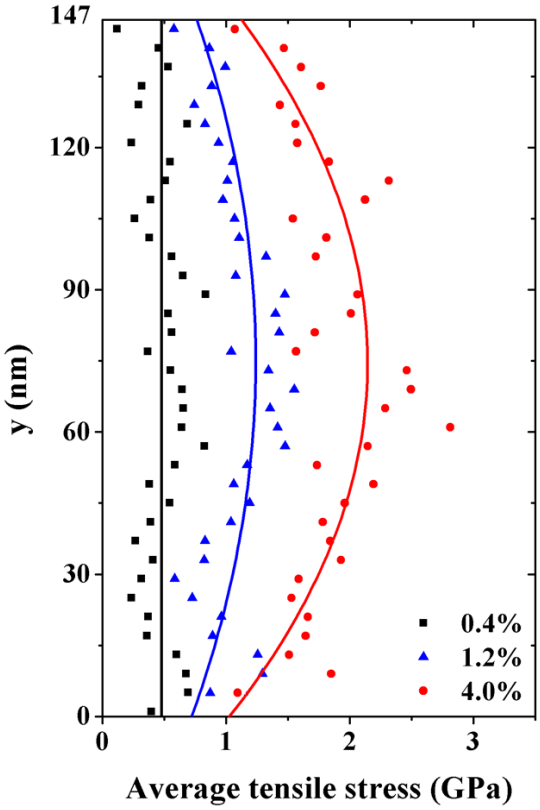

Figure 2.12 MD-simulated distribution of average tensile stress in the cross section of GNG Cu at various applied strain loads. The symbols represent the average tensile stresses and the solid lines are the fitting curves.

2.3.2.2 Deformation mechanisms

Grain growth is an important deformation mechanism in the MD simulations of GNG Cu under axial tension, as shown in Figure 2.13. Grain growth starts to appear in a small fraction of nano-grains when the overall strain exceeds the elastic limit. But dramatic grain growth occurs in many grains only after the overall strain exceeds ~ 10%, as seen

from Figure 2.13(a-d). Grain growth is more dramatic in smaller nano-grains near the surface than larger grains in the central region. Progressive grain growth in the surface layer results in a gradual increase of surface roughness. These MD results are consistent with the earlier experimental observations of drastic grain growth in the surface GNG layer at large tensile strains by Fang et al. [27].

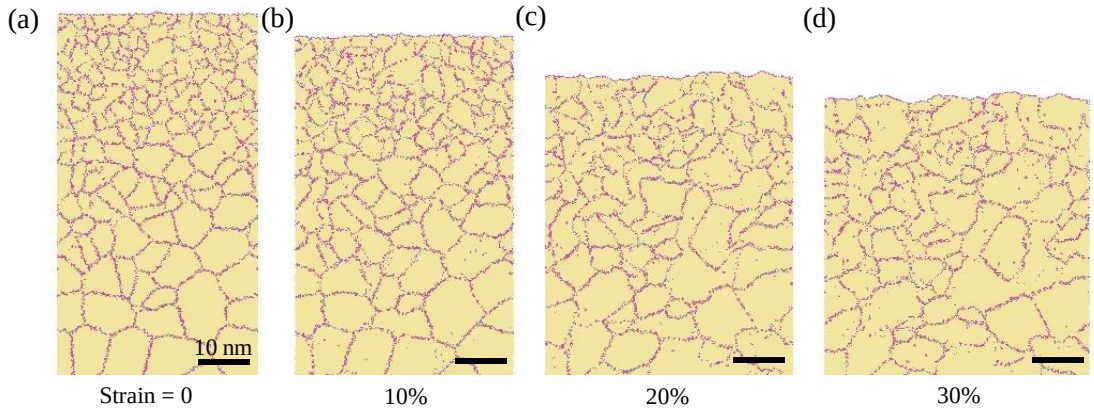

Figure 2.13 MD snapshots showing grain growth during axial tension of a GNG sample at various applied strains in (a-d). The GNG structure in (a) is the same as that in Figure 2.10(a). In (a-d), only the upper half of the GNG sample is plotted, so as to enlarge the displayed images for better visualization of gradient structures. Atoms are colored using the coordination number as defined in Figure 1(b), such that grain boundaries (primarily consisting of pink atoms) are clearly visible.

MD simulations further reveal the atomically-detailed processes of grain growth, which occurs through migration of grain boundaries, i.e., normal grain boundary motion, that is often coupled with shear deformation of the lattice traversed by the grain boundary. This coupled mode of grain boundary motion is consistent with the earlier MD study by Cahn et al. [131], and is further shown by our detailed tracking of individual grain

boundaries in MD simulations. Figure 2.14 presents an example of coupled migration and shear at a representative grain boundary. In Figure 2.14(a), we plot the grain boundary being tracked (highlighted by a red line) before loading, along with a line of atoms colored in black, serving as a marker. At an overall tensile strain of 10%, coupled migration and shear at this grain boundary can be clearly seen in Figure 2.14(b); migration of the grain boundary is shown by the boundary displacement from the initial to the current location; shear deformation of the lattice traversed by the grain boundary is clearly evident from the kinking of the black marker. The grain boundary migration can be also seen in Figure 2.14(c) and (d), where atoms are colored by the coordination number such that the grain boundary (mostly consisting of pink atoms) is readily distinguishable.

Migration of a grain boundary can often result in the concerted motion of adjoining grain boundaries connected at a shared triple junction. Using the same visualization schemes as in Figure 2.14, Figure 2.15 shows the concerted motion of three grain boundaries connected at a triple junction, in addition to coupled migration and shear occur at each individual grain boundary. Such concerted motions of grain boundaries can effectively accommodate the deformation incompatibility at the triple junction and also facilitate the equiaxial grain growth.

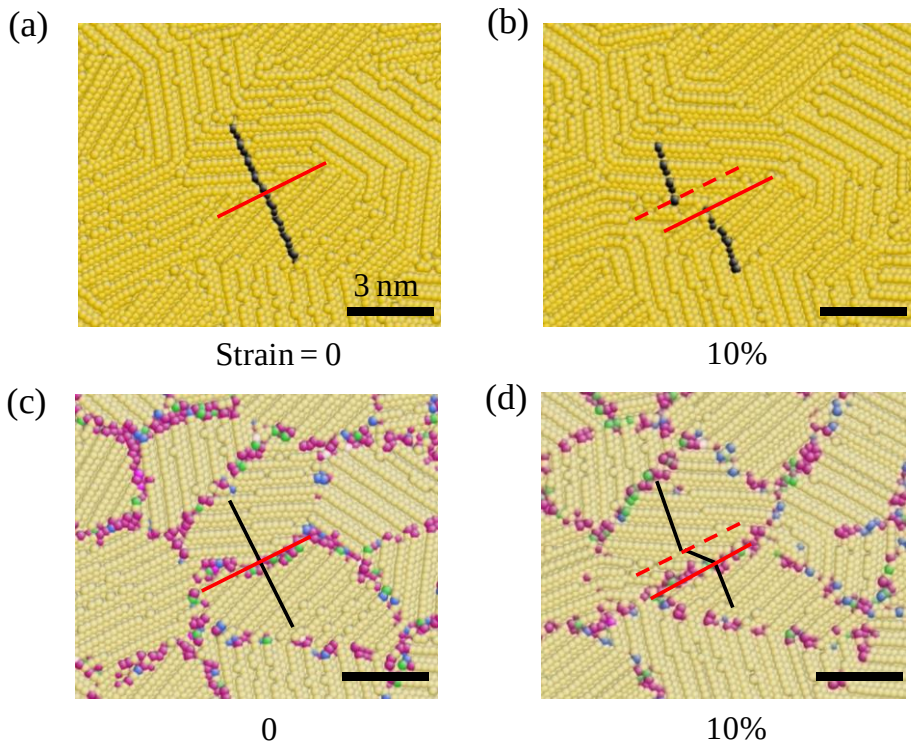

Figure 2.14 Coupled migration and shear deformation at a grain boundary. (a) Initial atomic structure at zero strain. The grain boundary is indicated by a red solid line. A straight line of atoms intersecting this grain boundary is colored in black, serving as a marker during deformation. (b) Atomic structure at an overall axial strain of 10%. The current position of the migrating grain boundary is indicated by the red solid line, while the old position by the red dashed line. Kinking of the marker occurs due to shear deformation of the lattice traversed by the grain boundary. (c-d) Same as (a-b) except that atoms are colored by the coordination number, clearly showing the migration of the grain boundary.

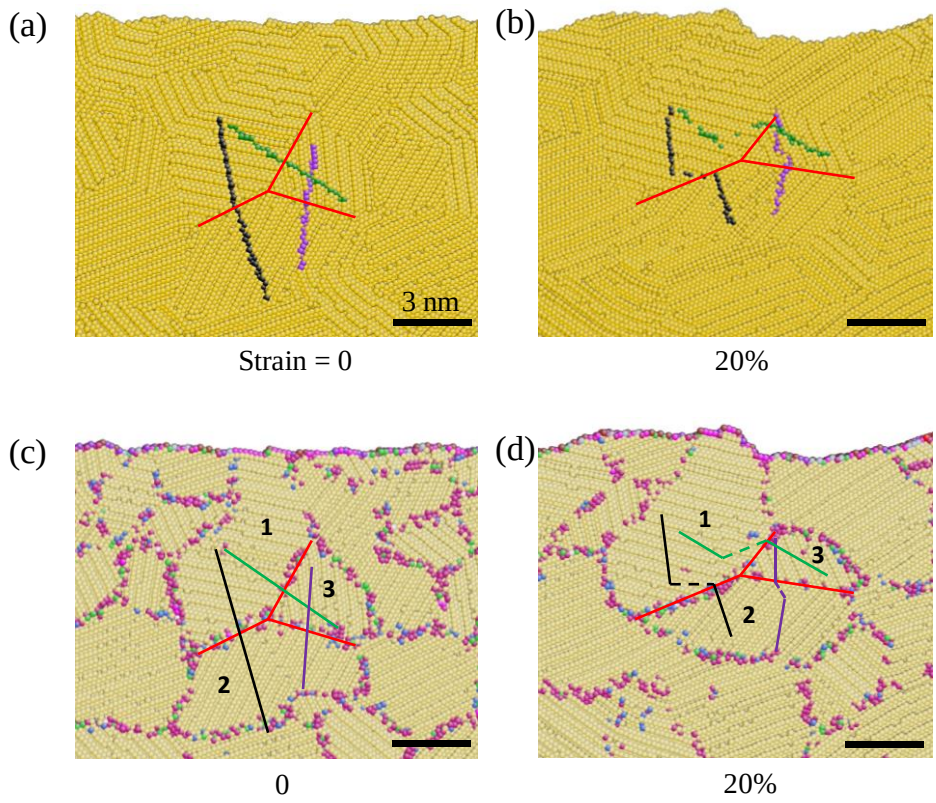

Figure 2.15 Concerted motion of grain boundaries at a common triple junction. (a-b) Atomic structures at the overall axial strain of zero (left) and 20% (right), with the same marking schemes as Figure 2.14(a-b). Concerted motion of three grain boundaries leads to the displacement of the triple junction. (c-d) Same as (a-b) except that atoms are colored by the coordination number, clearly showing the migration of grain boundaries.

In addition to grain growth, dislocation plasticity is also considerably active in the MD simulations of tensile deformation of GNG Cu. Figure 2.16 shows the dislocations inside nano-grains at different applied axial strains. Specifically, in Figure 2.16(a), the GNG Cu at zero strain is nearly free of dislocations. As the axial load increases, leading partials start to nucleate from grain boundaries, presumably at easy sites with relatively low barriers of nucleation. At this stage, most trailing partials are still held by grain boundaries, such that leading partials glide inside grains with stacking fault ribbons in their

wakes, as seen from Figure 2.16(b-d). As the applied strain load is further increased, trailing partials emit progressively at grain boundaries. The resulting full dislocations traverse through the grains. Subsequently, they are either obstructed by or transmit through the opposite sides of grain boundaries. Meanwhile, leading partials continue to nucleate from other sites of grain boundaries, followed by similar processes of gliding, full-dislocation formation, obstruction and/or transmission. Such dynamic dislocation activities proceed continuously with increasing loads.

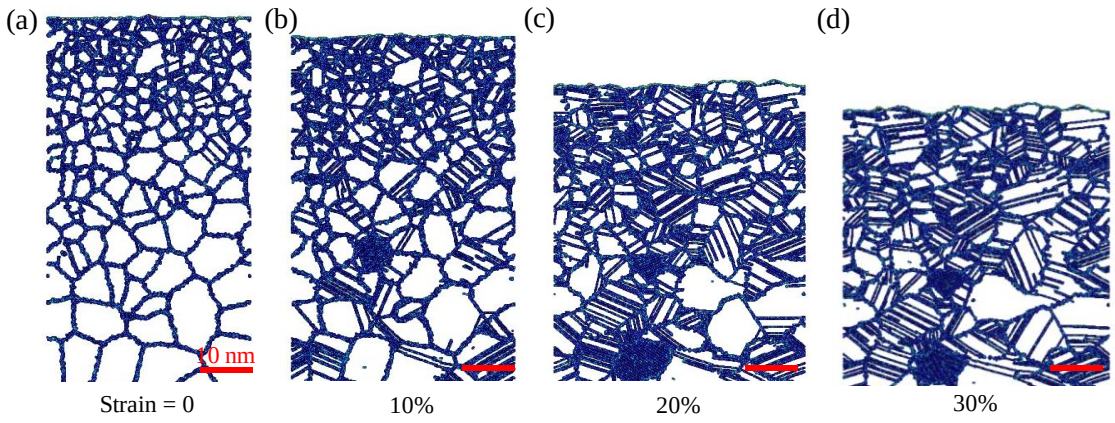

Figure 2.16 MD snapshots showing the dislocation processes in GNG Cu during axial tension of a GNG sample at various strain levels in (a-d). Atoms are colored by the central symmetry parameter, showing grain boundaries and stacking faults - both partial and full dislocations appear in these images.

From Figure 2.16, it is interesting to observe that there are more dislocations inside smaller nano-grains within the surface layer than inside larger grains within the central region. Ashby has shown that the density of geometrically necessary dislocations (GND) in a grain is inversely proportional to the grain size [129]. This provides a plausible explanation of our MD results of grain-size-dependent dislocation density. Such a gradient

distribution of GND is a unique characteristic of the GNG structure. Its implication on plastic strain gradients and associated mechanics effects will be further discussed in section 2.4.

Since both grain growth and dislocation plasticity are observed in the present MD simulations of GNG Cu, one natural question is which mechanism is strength/rate-controlling. Argon and Yip [52] have previously developed a theoretical model showing that the intra-grain mechanism of dislocation plasticity is strength/rate-controlling in the classical Hall-Petch regime, while the inter-grain mechanism of grain boundary shear in the inverse Hall-Petch regime. Recall that we show in Figure 2.11 the tensile stress-strain curves for NG Cu with uniform grain sizes, which exhibit the behavior of "smaller is softer". In other words, the grain size range of 2.5 - 10nm studied for both NG and GNG samples by the present MD simulations fall into the inverse Hall-Petch regime. Hence, based on the Argon-Yip model, the strength/rate-controlling mechanism in those NG and GNG samples can be reasonably attributed to grain boundary shear, which is usually coupled with grain boundary migration and resultant grain growth as discussed earlier.

2.4 Summary and outlook

2.4.1 Summary

We have developed both crystal plasticity and atomistic models to investigate the mechanics and deformation mechanisms in GNG Cu. We build a quasi-two-dimensional model of columnar nano-grains with gradient sizes using an adapted Voronoi tessellation method. We also extend the classical crystal plasticity theory to incorporate the grain-size-

dependent yield strength and strain hardening. The major results are summarized as follows.

- CPFE simulations are performed to study the tensile responses of GNG Cu with grain sizes in the classical Hall-Petch regime. Assuming grain-size-dependent yield strengths, CPFE simulations reveal the novel gradient distributions of stress and plastic strain in the cross section of GNG samples. Such gradient distributions arise primarily due to the progressive attainment of yield points in grains with gradient sizes and accordingly different slip resistances.
- CPFE simulations also reveal the spatial variations of stress and plastic strain, which result from the combined effects of random grain orientations and gradient grain sizes. In addition, CPFE simulations are used to study the connections between sample-level strain hardening and grain-level hardening with grain-size dependence. The results suggest an appealing opportunity of tailoring grain-level strain hardening for achieving the desired overall strain hardening in GNG structures, given the fact that strain hardening is known to play a critical role in plastic instability such as necking and rupture.
- MD simulations are performed to investigate the atomistic mechanisms of plastic deformation in GNG Cu. Dramatic grain growth is observed, particularly after the overall strain exceeds ~10%. Grain growth occurs through migration of grain boundaries that is often coupled with shear deformation of the lattice traversed by the grain boundary. This is consistent with the early MD study of individual grain boundaries by Cahn et al. [131]. In addition, MD simulations also reveal the concerted motion of grain boundaries connected at the shared triple junction.

- Besides grain growth, MD simulations of GNG Cu reveal considerable dislocation plasticity, involving progressive nucleation of leading and trailing partials from grain boundaries, their gliding inside nano-grains, and obstruction/transmission at grain boundaries. Interestingly, there are more dislocations inside smaller nano-grains within the surface layer than inside larger grains within the central region. This is attributed to the formation of geometrically necessary dislocations whose density is grain-size-dependent, which is a unique characteristic of the GNG structure.
- The atomistic mechanisms of grain growth and dislocation plasticity revealed by MD simulations at high strain rates should be active during the experimental testing of GNG Cu at low strain rates, irrespective of grain size. However, we note that the grain size range of 2.5 - 10 nm studied for both GNG and NG samples by the present MD simulations fall into the inverse Hall-Petch regime. This is confirmed by our MD simulations of NG Cu with uniform grain sizes that exhibit the behavior of "smaller is softer". Hence, the strength/rate-controlling mechanism in the present MD simulations of NG and GNG samples can be reasonably attributed to the grain growth through coupled migration and shear of grain boundaries.

2.4.2 Implications and future work

Stress and plastic strain gradients. GNG metals have the unique microstructure with a gradient distribution of grain sizes. Our CPFE simulations reveal the novel gradient distributions of stress and plastic strain in the cross section of GNG samples. Such gradient distributions arise primarily due to the grain-size-dependent yield strength. Importantly, the gradient stress and plastic strain develop under an overall uniform deformation, and

they stand in stark contrast to the widely studied strain-gradient plasticity induced by applying non-uniform deformations such as torsion [126], bending [127], and indentation [128]. Our MD simulations of GNG Cu further show that the dislocation density is gradient, being higher inside smaller nano-grains. Dislocations in these MD simulations are primarily of the geometrically necessary type, due to the high strain rates of MD that tend to suppress the thermally activated formation of statistically stored dislocations. The same kind of grain size dependence is expected to hold to the density of geometrically necessary dislocations in gradient grains with any size range. It follows that the gradient density of geometrically necessary dislocations could underlie the macroscopic plastic strain gradients in GNG metals with grain sizes in the classical Hall-Petch regime.

Importantly, the plastic strain gradient is expected to produce a non-local strengthening effect and thereby enhance the overall yield strength. Such a strengthening effect has been well recognized in the previous studies of strain gradient plasticity induced by applying non-uniform deformations [126-128]. In the future, it is intriguing to perform the systematic experimental testing for samples with controlled GNG structures, so as to provide a firm experimental basis of the strengthening effect of plastic strain gradient arising from grain size gradient. The present crystal plasticity model only accounts for the grain-size-dependent yield strength, but does not include the strengthening effect of plastic strain gradient. Hence, the future study also requires the development of a non-local plasticity model and associated numerical procedure, so as to quantitatively evaluate the effect of plastic strain gradient through comparison with the experimental study.

Grain size gradient. The spatial distribution of the gradient grain size is expected to critically affect the stress and plastic strain gradients and accordingly the strengthening

effects on the GNG materials. From the material design standpoint, the gradient characteristics of grain size, including its magnitude and spatial variation (e.g., linear vs. non-linear change), should serve as important design parameters for achieving an optimal strength enhancement with retained ductility in nanocrystalline metals and alloys. To this end, it is essential to develop novel processing methods for a controlled variation of grain size gradient. Meanwhile, the non-local CPFE models and simulations that include the strengthening effect due to plastic strain gradient can be used to guide the design of the optimal grain size gradient.

In recent years, based on the concept of the atomic deformation gradient by using atomic position, Tucker et al.[132-134] developed a method to calculate continuum mechanical deformation by determining a non-local atomic deformation gradient metric. Their work provides insight into atomic behavior during shear deformation in 2D grain boundary structures, thin 3D equilibrium bicrystalline grain boundary structures and nanocrystalline structures. The significance of their work provides insight into our future work on gradient nano-grained copper.

CHAPTER 3. STRENGTH AND DEFORMATION MECHANISMS IN TRANSMODAL GRAINED ALUMINUM

Bimodal grained aluminum is developed in experiments. To understand the deformation mechanisms bimodal grained Al, we performed size-dependent crystal plasticity finite element (CPFE) simulations to investigate the effect of heterogeneous grains on the strength of bimodal grained Al. We also developed model of transmodal grained Al. We developed three dimensional model of heterogeneous grains with controllable sizes and distributions. We performed CPFE simulations to simulate the uniaxial deformations of the bimodal grained and transmodal grained Al. Section 3.1 is focus on the experiments. Section 3.2 is focus on the development of bimodal grained Al and transmodal grained Al. The CPFE simulation results are presented in section 3.3.

3.1 Sample preparation and experimental results

Spherical Al powders were used to prepare samples. Three different kinds of Al powders with average powder sizes of 0.8μm, 1.4μm and 5.0μm were used. The powder size can be measured from scanning electron microscope (SEM) image. Figure 3.1(a-c) are showing the SEM images of Al powders with the three different powder sizes. Furthermore, the powder sizes are following a unimodal distribution. Figure 3.1(d) is showing the distribution of the powder sizes of Al powder with average size of 1.4μm.

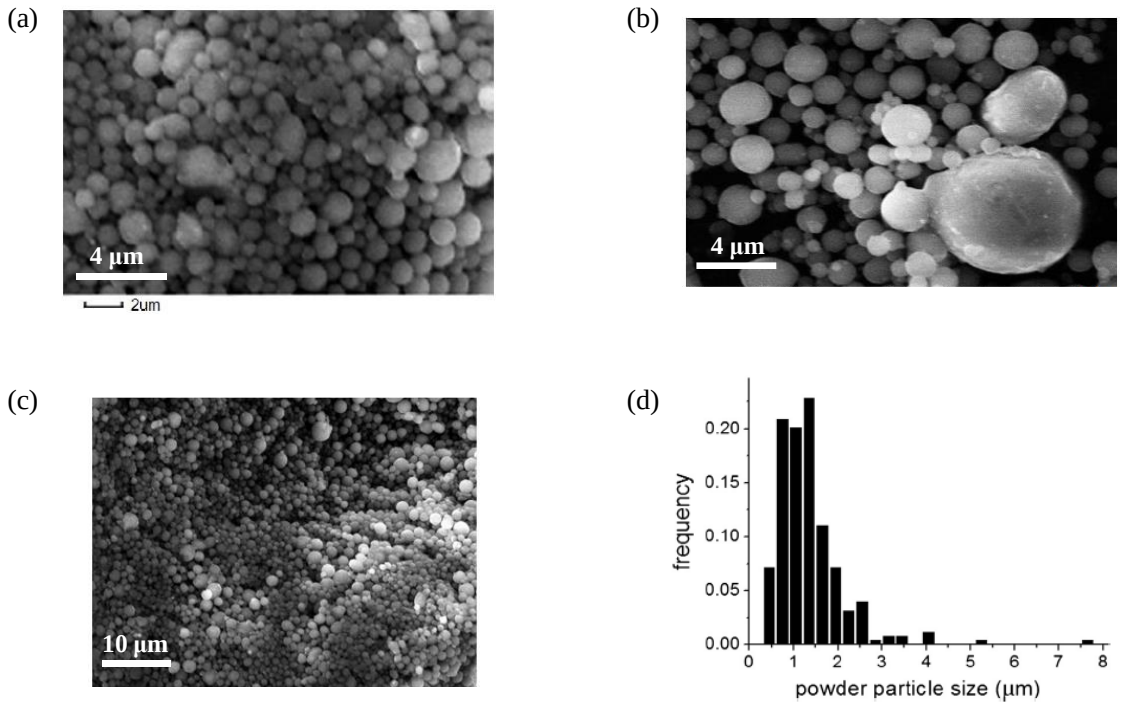

Figure 3.1 SEM images of the three kinds of Al powders with average sizes of: (a) 0.8µm, (b) 1.4µm, and (c) 5.2µm [135]; (d) distribution of the powder sizes of Al powder with average size of 1.4µm [135].

The spark plasma sintering (SPS) technique has been used to prepare polycrystalline Al samples. The SPS process was conduct using a specific developed heating/loading cycle, with a temperature up to 600 °C and a maximum up to 50 MPa. Further details of spark plasma sintering process are given elsewhere [39, 135]. After the SPS process, the Al powder were sintered together. As a result, polycrystalline Al samples were obtained.

The microstructure of the polycrystalline Al samples are characterized by SEM. Figure 3.2(a) shows the SEM images of polycrystalline Al. The grains are fully recrystallized. The grain sizes of polycrystalline Al are the same as the respective powder

sizes, as shown in Table 3.1. It means that there is no grain growth during the sintering process. This is because a large number of small oxide particles are at the grain boundaries, as shown in Figure 3.2(b). These oxide particles are effective in pinning grain boundaries to prevent grain growth. Furthermore, the EBSD data in Figure 3.3(a) and the distribution of grain boundary misorientation in Figure 3.3(b) show that the textures of the SPS Al are random.

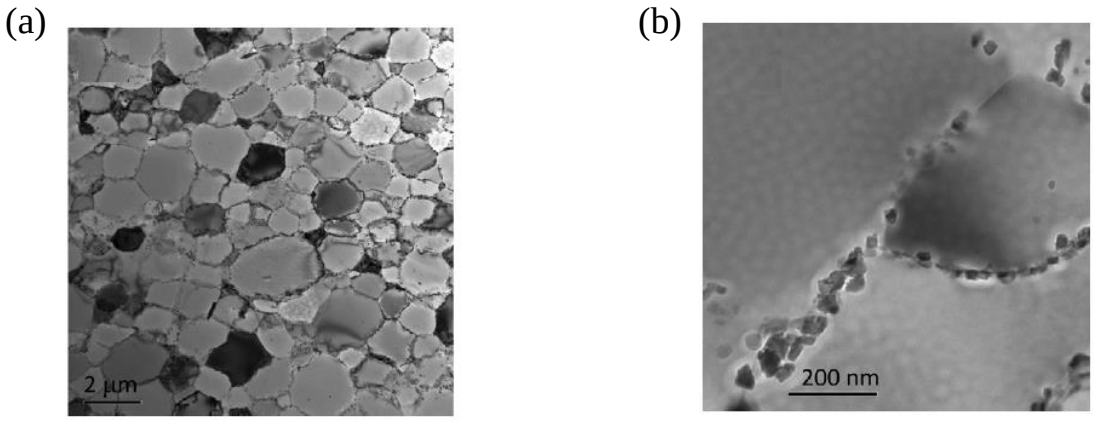

Figure 3.2 TEM image of the SPS sample. (a) fully recrystallized grain structure with an average grain size of 0.8μm; (b) oxide particles at the grain boundaries [135].

Table 3.1 SPS samples of polycrystalline Al sintered from powders of different size.

Starting powders	Particle size range	Samples	Average grain size	Density
Powder-5μm	2μm-15μm	**Al-5.2μm**	5.2μm	99%
Powder-1.4μm	0.5μm-5μm	**Al-1.3μm**	1.3μm	99%
Powder-0.8μm	0.2μm -2μm	**Al-0.8μm**	0.8μm	99%

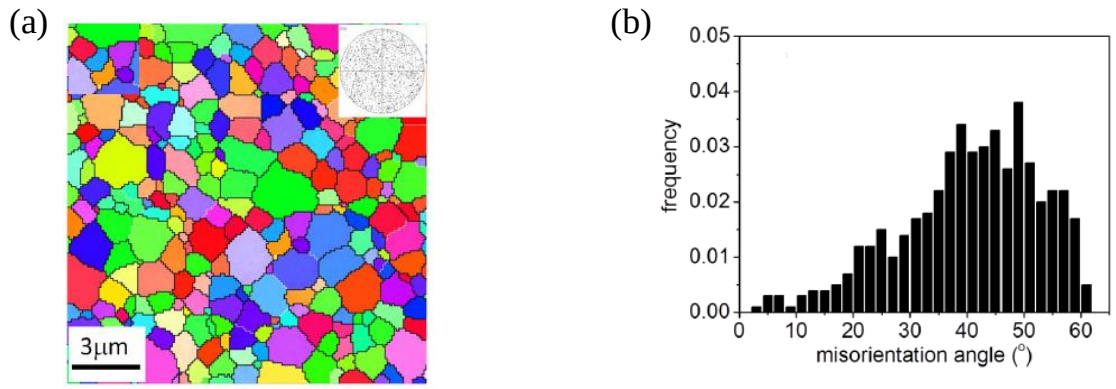

Figure 3.3 SPS Al sample with none texture. (a) EBSD data for the microstructure of SPS Al sample with an average grain size of 1.3μm; (b) distribution of grain boundary mis-orientations.

The constraint grain growth enables us to better control the grain size. Therefore, SPS polycrystalline Al samples are prepared with a mixing of fine powders and coarse powders. In experiments, mixed powders of powders of an average size of 0.8μm and powders of an average size of 5.2μm are used to prepare the polycrystalline Al by SPS process. As a result, the polycrystalline Al has a combination of fine grains and coarse grains. The grains are well-mixed. We call this material 'bimodal grained Al'. The EBSD images of bimodal grained Al are shown in Figure 3.4. Furthermore, the proportion of the mixed powders are varied, respectively, with a weight ratio of 5.2μm of 0%, 12%, 25%, 37%, 50%, 63%, 75%, 88% and 100%. The microstructures of bimodal grained Al are varying with the proportion, as shown in Figure 3.4.

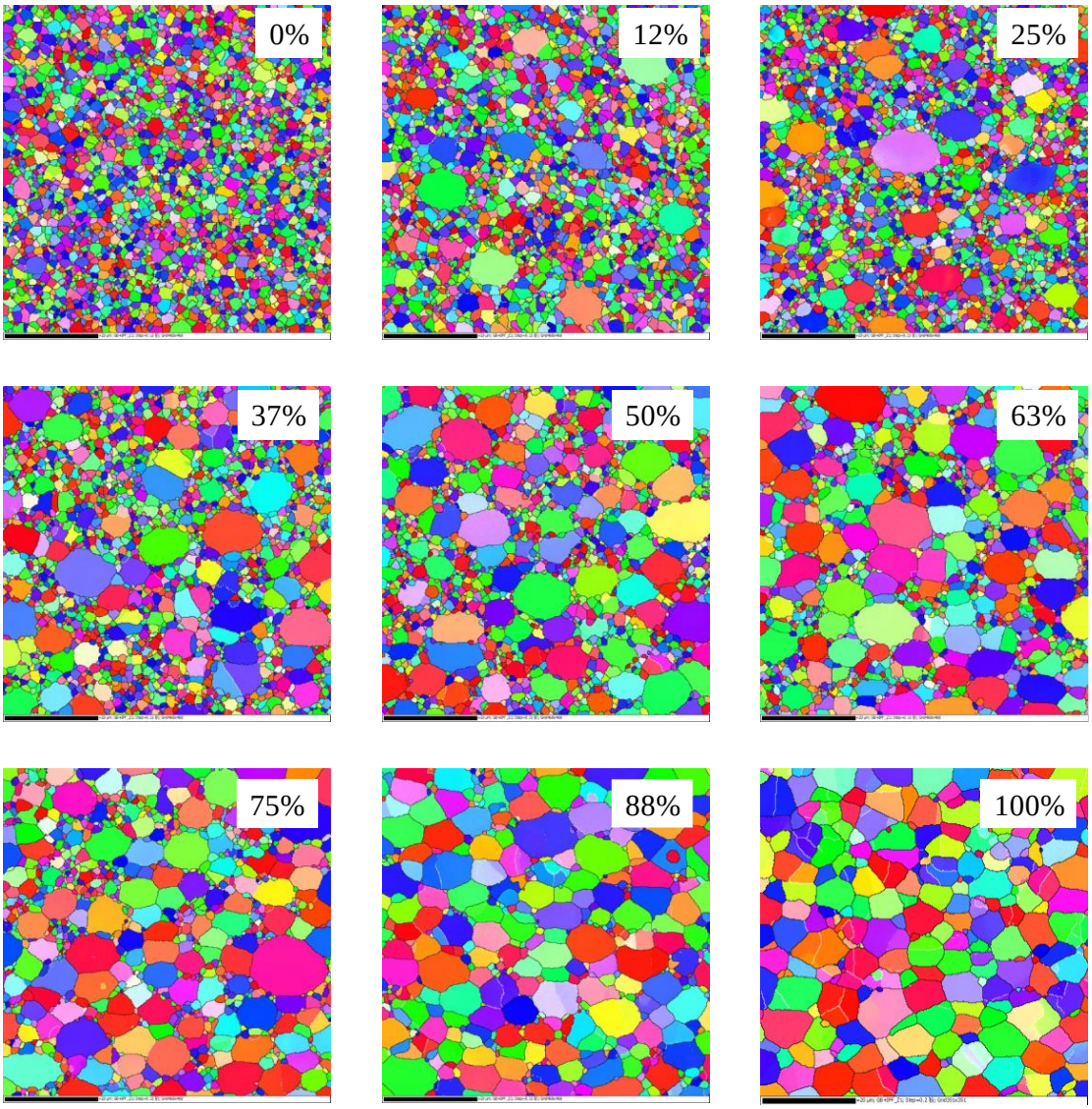

Figure 3.4 EBSD images of bimodal grained Al with different proportions of fine powders (0.8μm and coarse powders (5.2μm), respective; with a weight ratio of 5.2μm of 0%, 12%, 25%, 37%, 50%, 63%, 75%, 88% and 100%.

Mechanical experimental tests are conducted on polycrystalline Al. Figure 3.5 shows the stress-strain curves of polycrystalline Al. The stress is increasing with the grain size, following the Hall-Petch relation. The ultimate tensile strain is decreasing with the grain size, as shown in Figure 3.5(a). Figure 3.6 shows the stress-strain curves of bimodal

grained Al. The stress is increasing with the proportion of 0.8μm fine powders (in other words, the stress is decreasing with the proportion of 5.2μm coarse powders). The ultimate tensile strain is larger than 10% when the proportion of 5.2μm coarse powders is larger than 25%. Therefore, the bimodal grained Al shows a combination of strength and ductility. To understand the novel mechanical behaviors of bimodal grained Al, CPFE modeling is performed. The modeling works are discussed in the following sections.

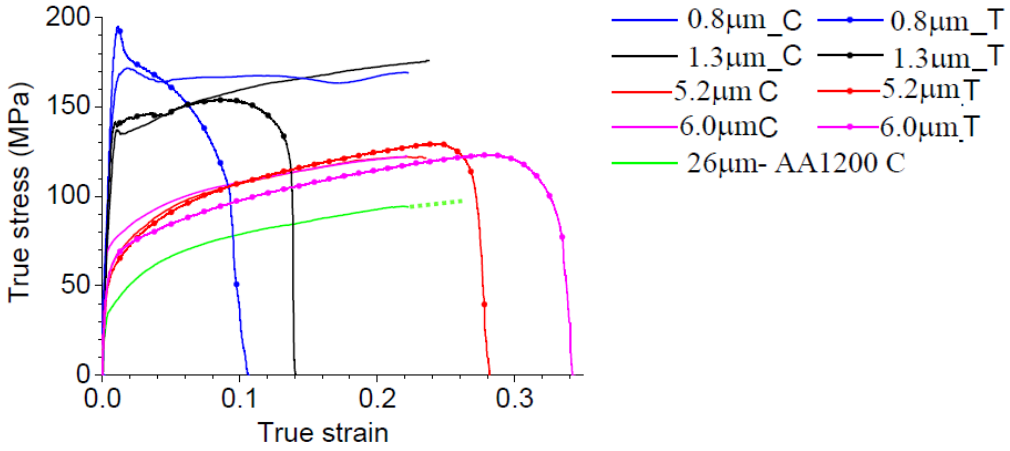

Figure 3.5 Stress-strain curves for tension (T) and compression (C) of SPS polycrystalline Al.

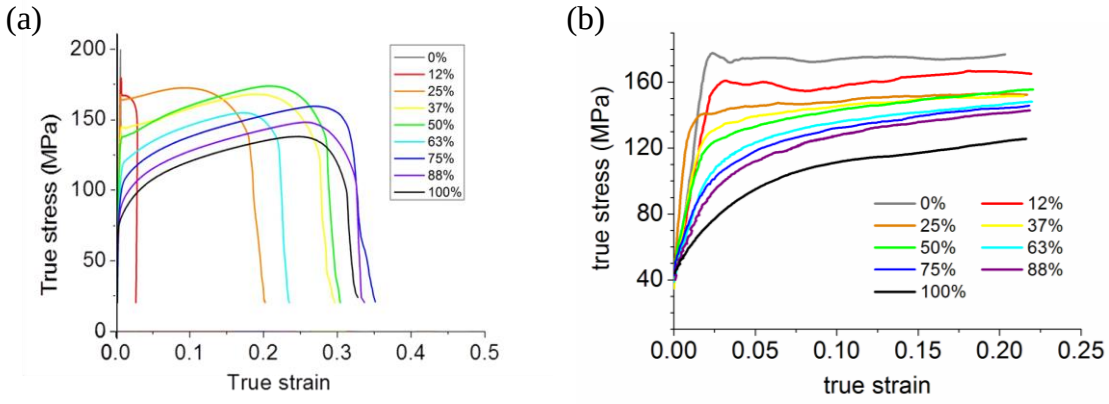

Figure 3.6 Stress-strain curves for tension (a) and compression (b) of bimodal grained Al.

3.2 Development of structures of bimodal grained Al and transmodal grained Al

Figure 3.7 shows three-dimensional structure models of bimodal grained Al rendered in an open-source software Neper [136]. There are grains of two sizes, respectively, with diameters around 0.8μm and 5.2μm. To construct this model, the first step was to pack poly-dispersed spherical particles with diameters of 0.8μm and 5.2μm. The geometry of packed particles was generated from a discrete element method simulation with LAMMPS [117, 137] . In this simulation, spherical particles with diameters of 0.8μm and 5.2μm were poured into a cubic container. The number of particles with each diameter was prescribed. The built-in Hertzian model for granular spherical particles was used to simulate the particle interactions, and the particle system was relaxed [138-140]. After relaxation, the centroids of the particles correspond to the centroids of the grains, and the diameters of the particles correspond to the grain diameters. Given the diameter and the position of the centroid of each particle, Laguerre tessellation was applied to construct the weighted Voronoi diagram with Neper. Each Voronoi cell is a polyhedron with an irregular shape, representing a grain in the AM SS structure. The diameter and the volume of each grain were calculated with the built-in functions in Neper and were used for the calculations of the volume fraction, as shown in Figure 3.7.

Furthermore, the fractions of particles with different diameters were tuned in order to obtain the different desired volume fractions in Figure 3.7. Figure 3.7(a) shows a bimodal grained Al with 66% grains with diameters around 0.8μm and 34% grains with diameters around 5.2μm, as shown in the distribution in Figure 3.7(b). We call the structure 34%-bimodal. Figure 3.7(c) shows a bimodal grained Al with 53% grains with diameters around 0.8μm and 47% grains with diameters around 5.2μm, as shown in the distribution

in Figure 3.7(d). Figure 3.7(e) shows a bimodal grained Al with 39% grains with diameters around 0.8μm and 61% grains with diameters around 5.2μm, as shown in the distribution in Figure 3.7(f). We call the structure 61%-bimodal. The size of the structures of bimodal grained Al in Figure 3.7(a), 7(c) and 7(e) is 9.84μm × 9.84μm × 9.84μm. Furthermore, Figure 7(g) shows three intersections along x, y and z direction of bimodal grained Al in Figure 7(a). These intersections show more details on the heterogeneous distribution of grains with two different sizes.

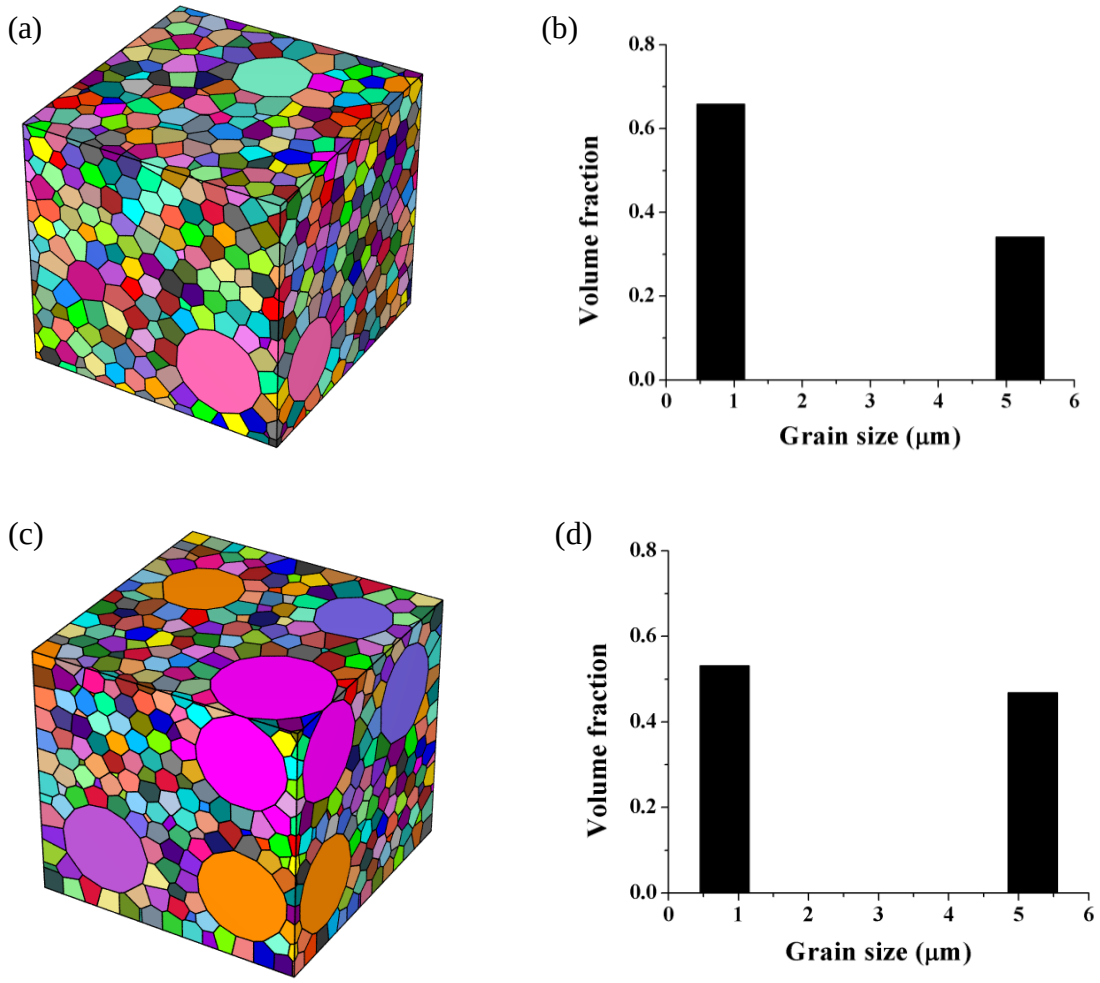

Figure 3.7 Structures of bimodal grained Al (a), (c), (e) and the corresponding volume fraction distribution, respectively, (b), (d), (f); (g) Intersections of bimodal grained Al in (a).

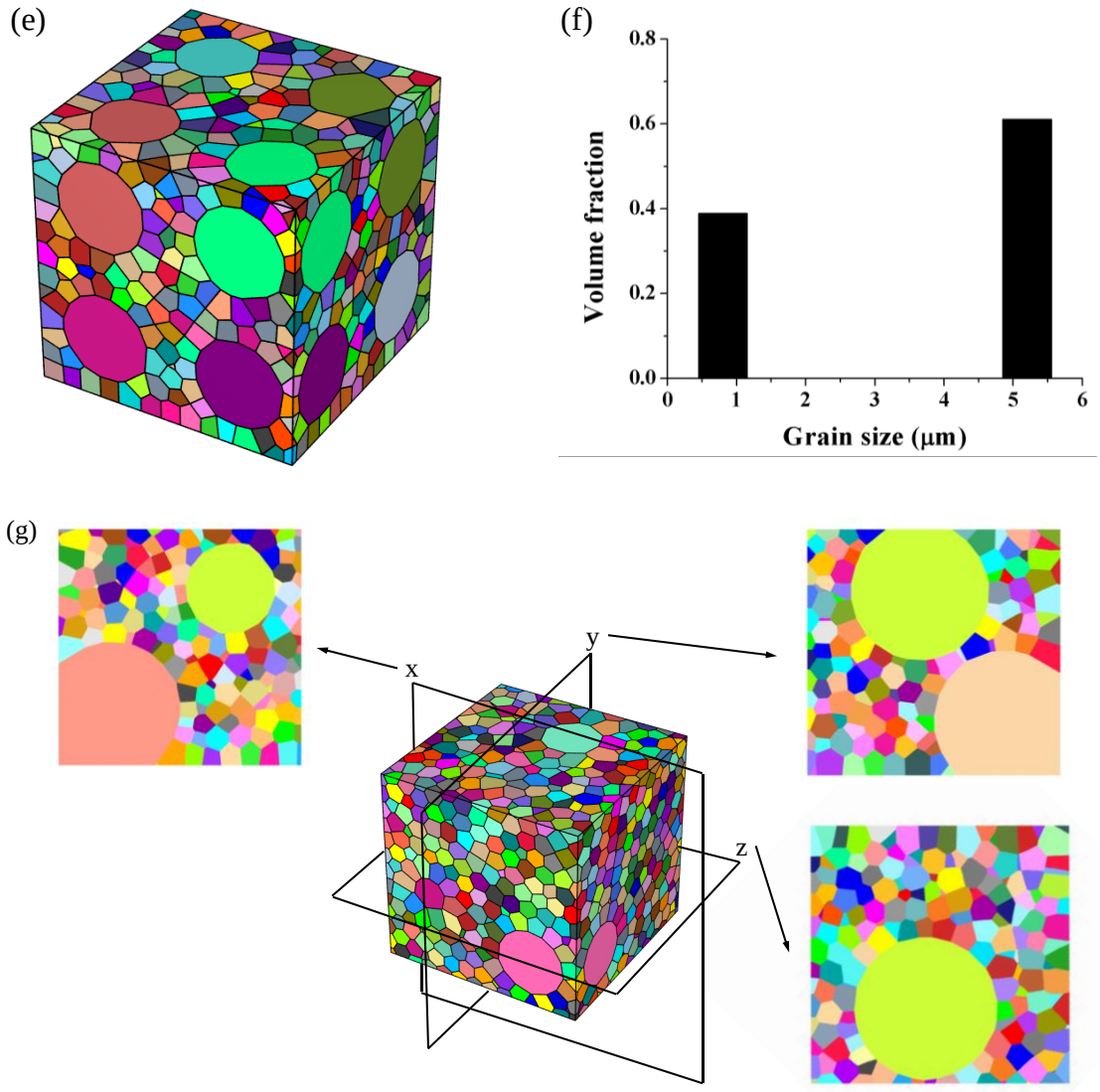

Figure 3.7 (continued).

Transmodal grained Al is also developed for simulations. Three-dimensional structure models of transmodal grained Al are shown in Figure 3.8. Figure 3.8(a) shows a transmodal grained Al with grain sizes nearly uniformly distributed from 0.8μm to 5.2μm, as shown in Figure 3.8(b). Figure 3.8(c) shows a transmodal grained Al with grain sizes

which peaking at 0.8μm and 5.2μm, as shown in Figure 3.8(d). There are much less grains in between sizes. The size of the structures of bimodal grained Al in Figure 3.8(a) and (c) is 9.84μm × 9.84μm × 9.84μm. Furthermore, Figure 3.8(e) shows three intersections along x, y and z direction of bimodal grained Al in Figure 3.8(c). These intersections show more details on the heterogeneous distribution of grains with gradually changing sizes.

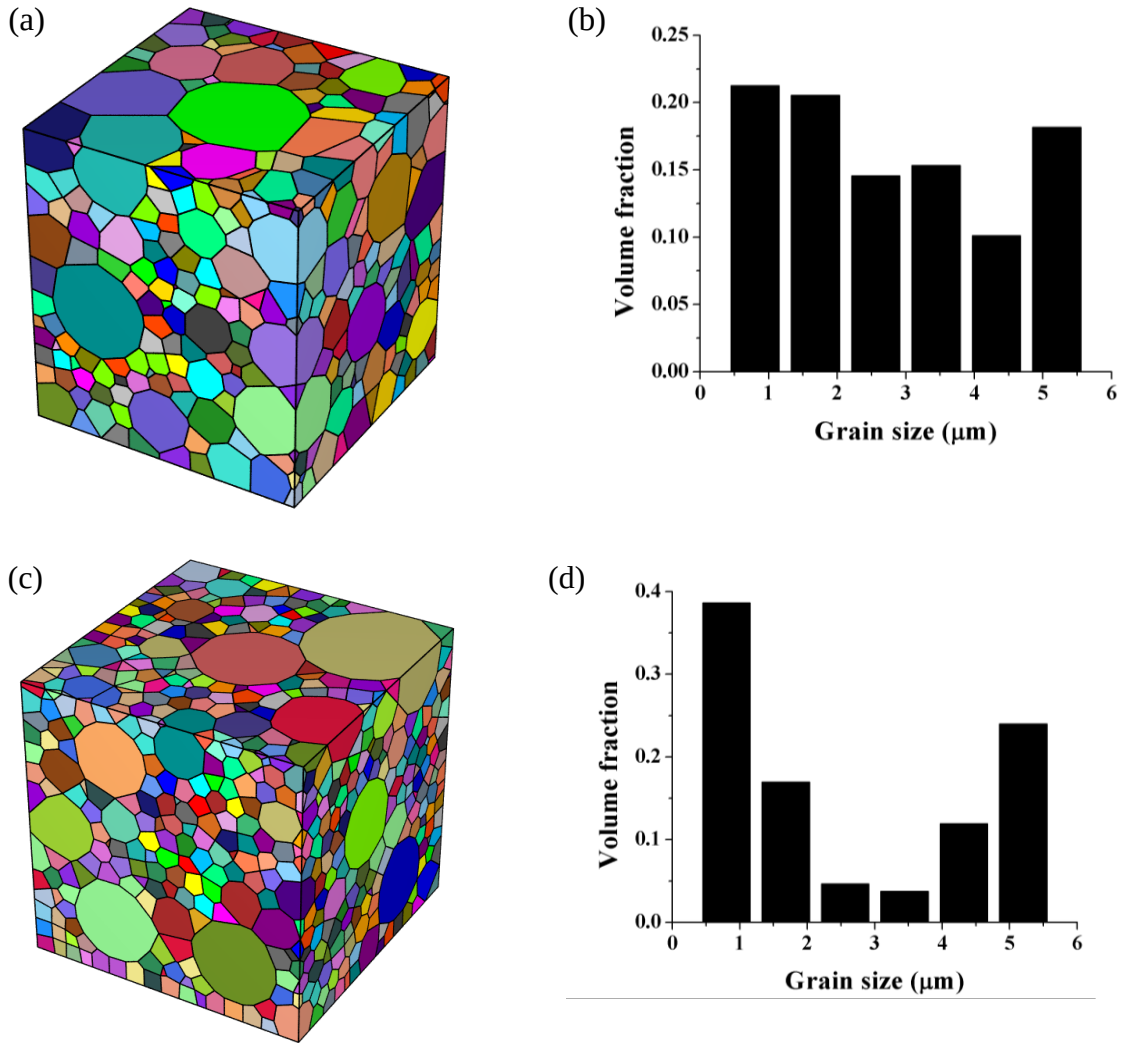

Figure 3.8 Structures of transmodal grained Al (a), (c) and the corresponding volume fraction distribution, respectively, (b), (d); (e) Intersections of bimodal grained Al in (c).

(e)

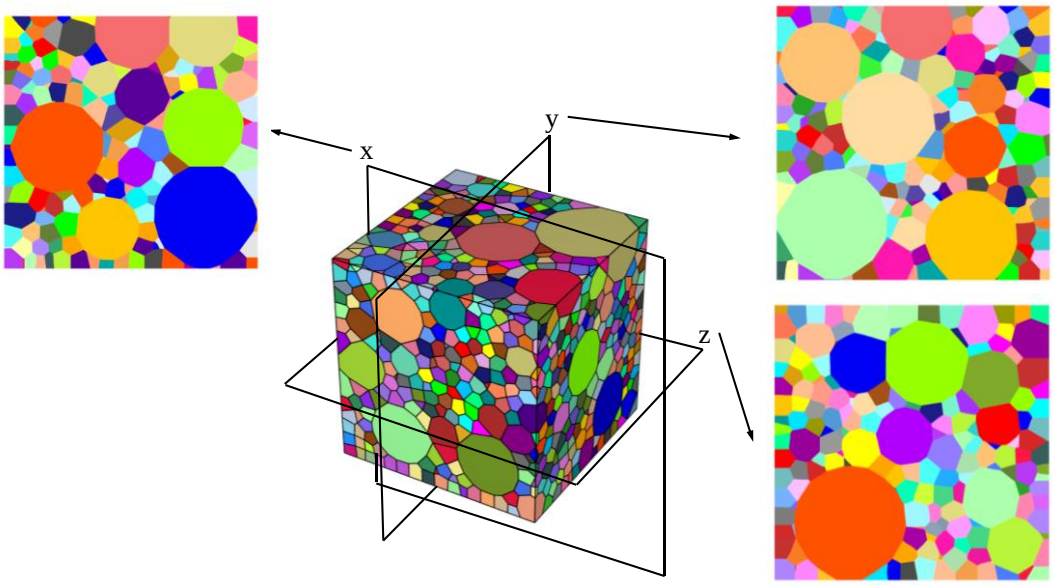

Figure 3.8 (continued).

3.3 Crystal plasticity finite element (CPFE) model

The structures of the bimodal grained Al and transmodal grained Al were used for crystal plasticity finite element simulations. Here we studied two bimodal grained Al samples, 34%-bimodal grained Al (in Figure 3.7(a)) and 61%-bimodal grained Al (in Figure 3.7(e)). The structure was meshed with the built-in meshing function in Neper with four-node linear tetrahedral elements (C3D4). The meshes were imported into ABAQUS/CAE to reproduce the sample of the bimodal grained Al in ABAQUS/CAE [116]. The resulting finite element structure models of bimodal grained Al rendered in ABAQUS/CAE are shown in Figure 3.9. There are 130407 elements in 34%-bimodal grained Al FEM model (in Figure 3.9(a)); 84043 elements in 61%-bimodal grained Al FEM model (in Figure 3.9(b)). The overall geometry of both samples is 8.94μm × 8.94μm × 8.94μm (x × y × z).

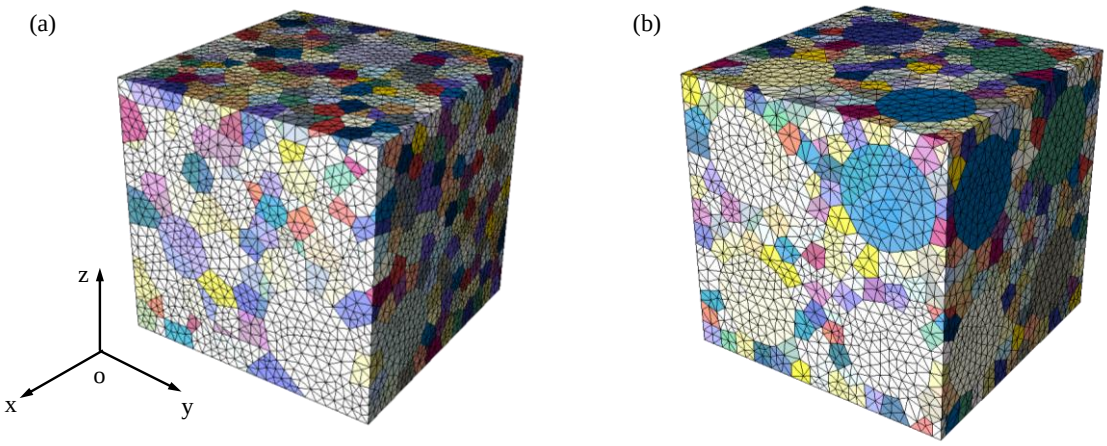

Figure 3.9 The finite element structures of (a) 34%-bimodal grained Al and (b) 61%-bimodal grained Al rendered by ABAQUS/CAE. The meshes are colored with respect to the grains they belong to. The coordinate system used in simulations is shown at the left corner.

Displacements and tractions are continuous at grain boundaries, meaning no separation or sliding between every pair of adjoining grains. The orientation of grains was assigned randomly in terms of three Euler angles, $\{\theta, \varphi, \Omega\}$, representing rotations from the crystal basis to the global basis [121]. A user material subroutine VUMAT was developed in ABAQUS/EXPLICIT to implement the grain-size-dependent crystal plasticity model which will be described below. With reference to Fig. 9, the boundary conditions of the bimodal grained Al samples were prescribed as follows: on $x = 0$ surface, the displacement in the x direction is zero ($u_x = 0$); on $y = 0$ surface, the displacement in the y direction is zero ($u_y = 0$); on $z = 0$ surface, the displacement in the z direction is zero ($u_z = 0$); on the $x = 8.94$μm and $z = 8.94$μm surfaces, the traction is zero; on $y = 8.94$μm surface, the velocity in the y direction is constant ($v_x = 8.9 \times 10^{-4}$μm/s), corresponding to an applied strain rate of 10^{-4}/s.

Using the finite element structure model of bimodal grained Al, crystal plasticity simulations were performed to simulate the uniaxial compression of AM SS under the plane-strain condition. To investigate the effect of grain size distribution on the stress-strain behavior of bimodal grained Al, the classical crystal plasticity theory was extended by incorporating the grain size dependence of yield strength [119-121, 141]. The complete details of the crystal plasticity model used in this work can be found in a recent article by Zeng et al. [141]. To apply this crystal plasticity model to bimodal grained Al, we assumed the slip resistance parameters in each grain, including $\{ s_0, h_0, a, s_{sat}, m\}$, were inversely proportional to the square root of grain size *d*,

$$\left\{s_0(d), h_0(d), a(d), s_{sat}(d), m(d)\right\} \sim d^{-1/2} \tag{3.1}$$

The numerical values for the slip resistance parameters are determined by fitting to the experimental stress-strain curve of SPS polycrystalline Al with grain size around 0.8μm and SPS polycrystalline Al with grain size around 5.2μm in Figure 5. Additionally, for the purpose of fitting, a much smaller three dimensional crystal plasticity finite element model has been developed, as shown in Figure 3.9(a). In the fitting processes, the simulation setup is the same as the setup in the simulations on the bimodal sample. For the 0.8μm grain, we took s_0 = 75 MPa, h_0 = 25 MPa, a = 1.8, s_{sat} = 160 MPa; and for the 5.2 μm grain, s_0 = 20 MPa, h_0 = 100 MPa, a = 2.4, s_{sat} = 140 MPa. The strain rate sensitivity *m* of Al varies from 0.012 and 0.01 for grain size *d* from 0.8μm to 5.2μm. The values of strain rate sensitivity are typical for polycrystalline FCC metals with grain size larger than 1μm. The stress-strain curves resulting from fitting are shown in Figure 3.10(b).

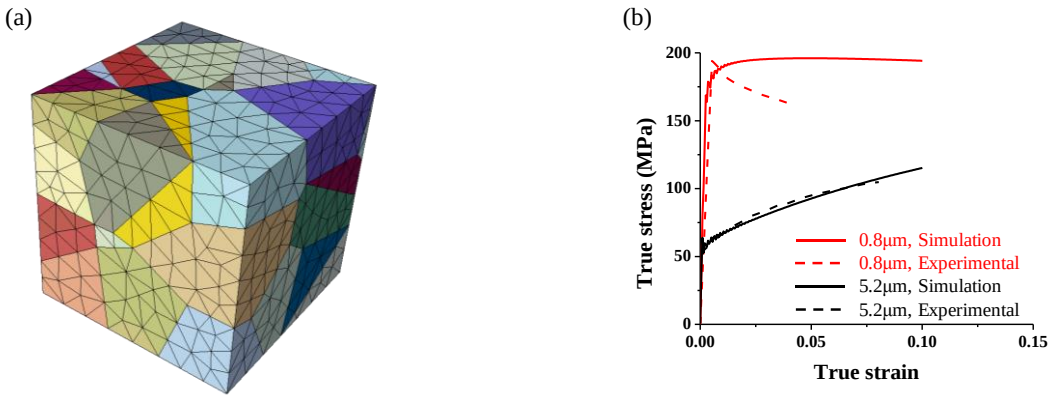

Figure 3.10 Fitting strategy for CPFE simulations. (a) Structure of polycrystalline Al for the purpose of fitting; (b) Stress-strain curves from the results of fitting.

To evaluate $\{s_0, h_0, a, s_{sat}, m\}$ for intermediate grain sizes, we used the above bounding values to fit the formula of $A = B + C \cdot d^{-1/2}$ where B and C are the fitting constants. The following fitting formulas were obtained

$$s_0(\text{MPa}) = -15.495 + 80.941 \cdot d^{-1/2},\ h_0(\text{MPa}) = 148.4 - 110.37 \cdot d^{-1/2}, \qquad (3.2)$$

$$a = 2.7872 - 0.883 \cdot d^{-1/2},\ s_{sat}(\text{MPa}) = 127.09 + 29.433 \cdot d^{-1/2},\ m = 0.0087 + 0.0029 \cdot d^{-1/2}$$

Other material properties, including elastic constants (C_{11}, C_{12}, C_{44}), twelve $\{111\}\langle 110\rangle$ slip systems, and the latent hardening matrix $\{q^{\alpha\beta}\}$, were assumed to be independent of grain size. For FCC Al, we took $C_{11} = 105$ GPa, $C_{12} = 62$ GPa and $C_{44} = 29$ GPa; $q^{\alpha\beta}$ = 1.0 if the slip systems α and β are coplanar and $q^{\alpha\beta}$ = 1.4 if they are non-coplanar [121].

3.4 CPFE simulation results

Figure 3.11 shows CPFE simulation results of bimodal grained Al using the grain-size-dependent crystal plasticity model described in section 3.3. In Figure 3.11, the red solid line is the stress-strain curve from CPFE simulation results of 34%-bimodal grained Al; the red dash line is the stress-strain curve from experimental results of 37%-bimodal grained Al; the black solid line is the stress-strain curve from CPFE simulation results of 61%-bimodal grained Al; the black dash line is the stress-strain curve from experimental results of 63%-bimodal grained Al. For both bimodal samples, the stress-strain relations from simulations match well with those from experiments. It indicates that our CPFE model is capable to predict the stress-strain behaviors of bimodal grained Al.

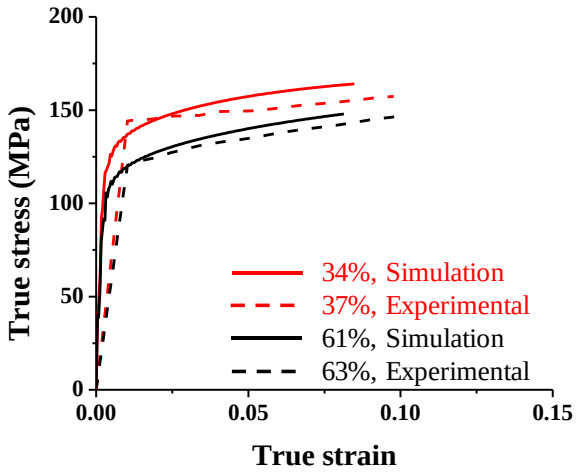

Figure 3.11 Tensile stress strain relations of bimodal grained Al.

Because of the non-uniform grain sizes, the stress in the bimodal grained Al is heterogeneous. Figure 3.12 shows the Von Mises stress of 34%-bimodal grained Al. Three intersections along x, y and z are also shown in Figure 3.12. Figure 3.13 shows the tensile

stress contour of 34%-bimodal grained Al. Three intersections along x, y and z are also shown in Figure 3.13. Figure 3.14a shows the Von Mises stress contour of 61%-bimodal grained Al; Figure 3.14b shows the tensile stress contour of 61%-bimodal grained Al.

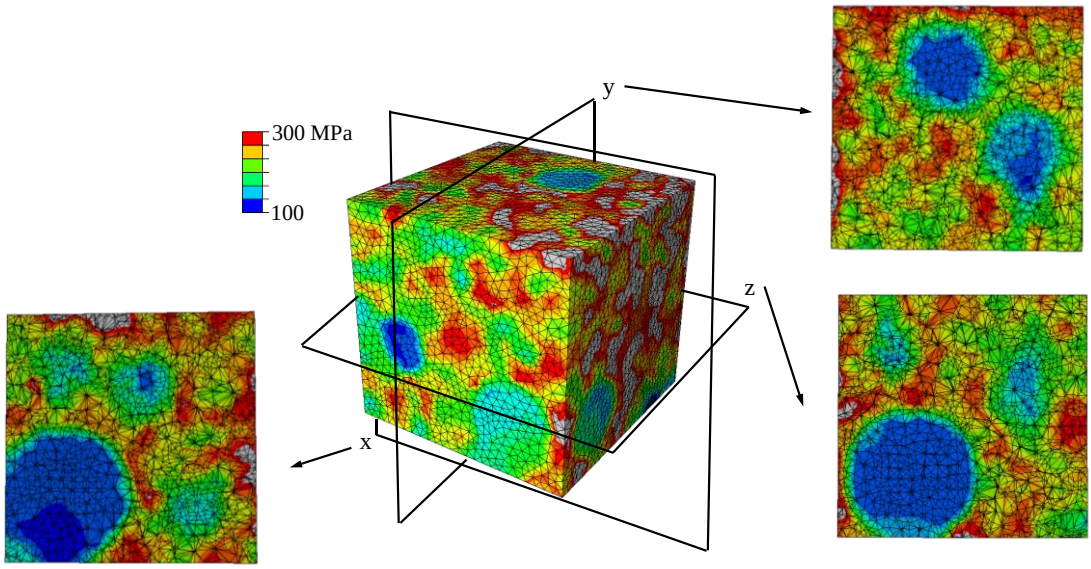

Figure 3.12 Von Mises stress contour of 34%-bimodal grained Al and views of intersections along x, y and z.

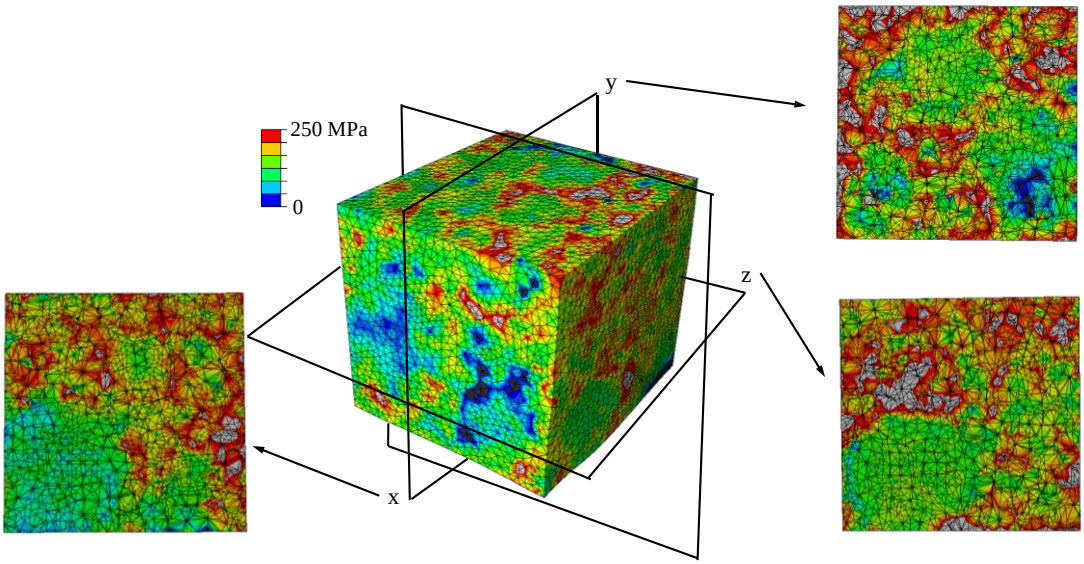

Figure 3.13 Tensile stress contour of 34%-bimodal grained Al and views of intersections along x, y and z.

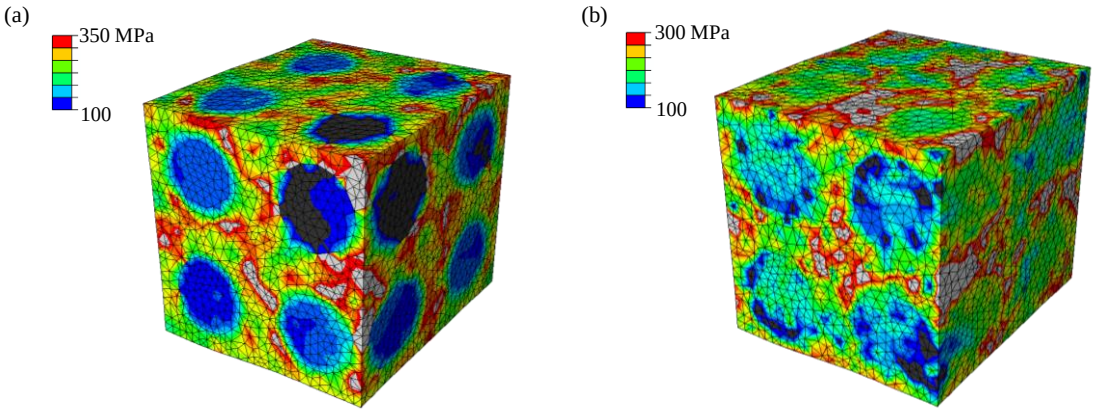

Figure 3.14 (a) Von Mises stress contour and (b) tensile stress contour of 61%-bimodal grained Al.

3.5 Conclusions

Bimodal grained Al has a mixture of fine and coarse grains which are distributed in a nonuniform way. We adapted Laguerre Voronoi tessellation to develop three dimensional polycrystal structure of bimodal grained Al. The grain size and size distribution are fully controllable. The models of bimodal grained Al have the same grain size and size distribution as the experimental sample. The models are further meshed to be developed into finite element models. Grain size-dependent crystal plasticity finite element (CPFE) simulations are performed to investigate the strength, as well as effects of grain-level heterogeneities. The simulation results show that the strength of bimodal grained Al is following the rule of mixture. The stress is nonuniform in the sample. The stress-strain curve matches well with the experimental results.

Model structure of transmodal grained Al is also developed. Transmodal grained Al has a mixture of grains with different sizes ranging from fine grains to coarse grains.

The grains of different sizes are mixed nonuniformly. Finite element models of transmodal grained Al are developed and grain size-dependent CPFE simulations are performed to study the effects of grain size distribution on the strength. The simulation results show that the strength of transmodal grained Al strongly depends on the grain size distribution. Several transmodal of different grains size distribution are studied. An optimal material design solution of transmodal grained Al is found in our simulations.

Zhang et al.[142] developed microstructure-based crystal plasticity finite element model to simulate the cyclic deformation of Ti–6Al–4V. In their work, the measured distributions of orientation and duplex Ti–6Al–4V are used to assign the same distributions of the crystallographic orientations to the finite element model. Shenoy et al.[143] developed microstructure-sensitive crystal plasticity model for polycrystalline Ni-base superalloy IN, under a hierarchical framework. Their model incorporates the effects of grain size, precipitate size distribution and precipitate volume fraction. The microstructural-sensitivity crystal plastiticy finite element models discussed above provide insight into my work on bimodal and transmodal grained Al.

CHAPTER 4. FRACTURE IN NANOTWINNED COPPER

Ultrafine grained copper with embedded nanoscale twin lamellas (hereafter referred to as nanotwinned Cu) exhibits an unusual combination of ultra-high strength (~ 1 GPa) and high tensile ductility (~14% elongation to failure) [23, 60-62]. The present work is motivated by previous in situ TEM observations [72, 73] (as shown in Figure 4.1) and aims to address the above questions by studying the growth of a pre-crack in a free-standing thin film of nanotwinned Cu using MD simulations. Section 4.1 is focus on the setup of MD simulations. The simulation results are discussed in section 4.2. The conclusions are in section 4.3.

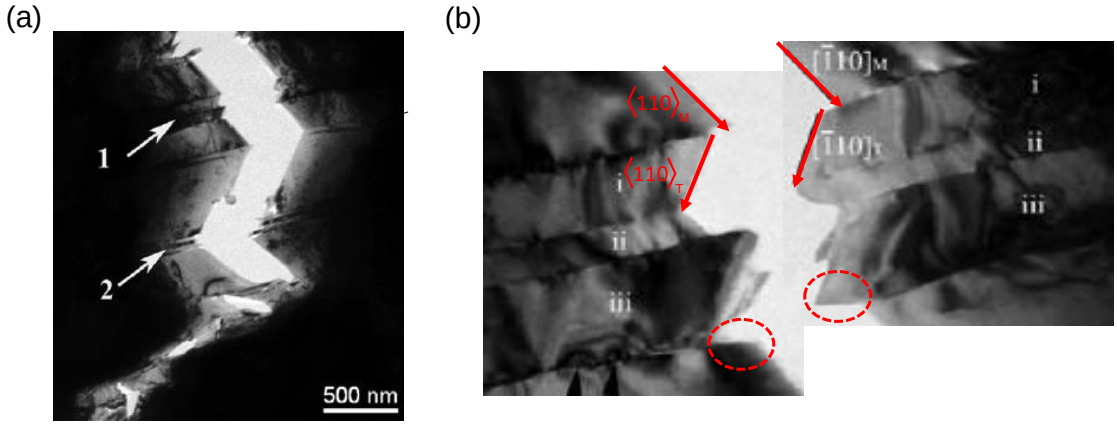

Figure 4.1 In situ TEM images of crack growth across twin groups in a thin foil of nanotwinned Cu, from a previous study by Shan et al. [72]. (a) A zigzag crack formed during tensile loading. (b) Magnified images of region 1 in (a), showing the $\langle 110\rangle_M$ and $\langle 110\rangle_T$ crack edges in the adjoining matrix (M) and twin (T) crystals. Circles indicate the short crack edges on twin boundaries.

4.1 Method

Figure 4.2 shows the setup of MD simulations containing a free-standing thin film of nanotwinned Cu with a pre-crack. The MD sample has an in-plane size of 22.1nm × 43.6 nm and a thickness of 1.7 nm. The twin boundaries are equally separated by 8.6 nm. Each twin lamella consists of the perfect Face-Centered Cubic (FCC) lattice. A pre-crack with a length of ~ 7nm is created at the sample edge by removing a single layer of atoms on the inclined $\{111\}$ plane. As a result, the pre-crack has its edge along the $\langle 112 \rangle_{\mathrm{M}}$ direction in the matrix (M) crystal. The total number of atoms in the system is 146,783. The periodic boundary condition is imposed only in the horizontal [112] direction. A uniaxial tensile load is applied in [112] direction at a constant strain rate $\dot{\varepsilon}$ of $2\times10^{9}/\mathrm{s}$, while both the [110] and [111] directions are traction free. The system temperature is maintained at 5K. We perform MD simulations with an embedded atom method (EAM) potential of Cu [130] using LAMMPS [144].

4.2 Results and discussion

Figures 3 presents a sequence of MD snapshots showing the simulated zigzag mode of crack growth. As the applied load increases, dislocations on the $\{111\}_{\mathrm{M}}$ slip plane in the matrix crystal emit from the crack tip and then pile up against the twin boundary that temporarily obstruct the movement of dislocations. As a result, a high local stress arises to act on the leading dislocation in the pileup array. As the applied load continues to increase, this local stress becomes so high that the leading dislocation transmits into the adjoining twin lamella and further glides on the conjugate $\{111\}_{\mathrm{T}}$ slip plane in next twin lamella. Dislocations behind the leading one in the pileup array repeat this “stop-and-go” process.

Meanwhile, transmitted dislocations in the adjoining twin lamella develop a pileup array, due to obstruction of the twin boundary further away from the crack tip. A similar "stop-and-go" process occurs at this twin boundary. Gliding of dislocations in each twin lamella causes local thinning at the active slip planes that eventually leads to lamella fracture. Since the crack is periodically deflected by twin boundaries, a zigzag crack path develops in MD simulations, which is consistent with the previous experimental observation through in situ TEM [72], as shown in Figure 4.1(a).

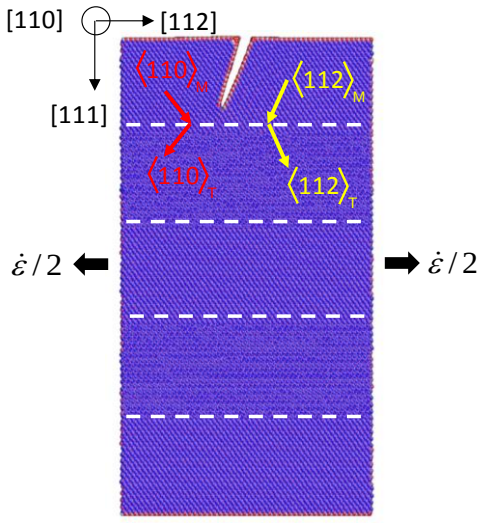

Figure 4.2 The MD setup involving a nanotwinned Cu thin film with a pre-existing edge crack. The dashed lines indicate twin boundaries. A uniaxial tensile load with constant strain rate $\dot{\varepsilon}$ is applied parallel to the twin boundary. Atoms are colored by the coordination number (CN). Atoms in a perfect FCC lattice have CN = 12 (yellow), while defective atoms have CN = 10 (green), 9 (pink), 8 (white), or 7 (blue).

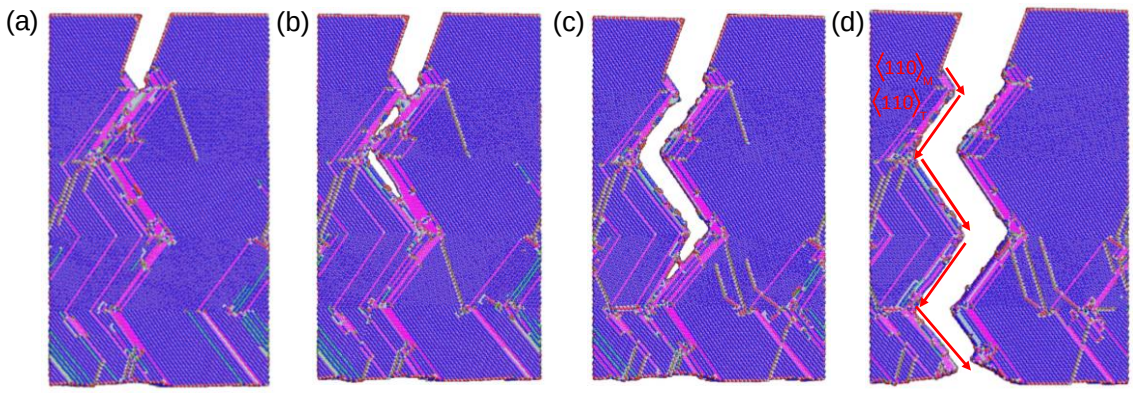

Figure 4.3 MD snapshots showing the simulated zigzag mode of crack growth. The applied tensile strains in (a) to (d) are 13.5%, 16.3%, 20.9% and 25%, respectively. The edges of the growing crack are along the $\langle 110 \rangle_M$ and $\langle 110 \rangle_T$ directions in the matrix (M) and twin (T) crystals, respectively. Atoms are colored with the same scheme as in Figure 4.2.

To understand the fracture mechanism of zigzag cracking, we note that in the 2D projected view of the film (Figure 4.2), the $\{111\}$ pre-crack has its edge along the $\langle 112 \rangle_M$ direction. We choose to create such $\{111\}$ pre-crack in order to facilitate cleavage fracture on the close-packed $\{111\}$ planes. However, it is unexpected to observe in Figure 4.3 that the edges of the growing crack in MD simulations are primarily aligned with the $\langle 110 \rangle$ directions in all lamellas. This footprint of $\langle 110 \rangle$ crack edges indicates that fracture does not occur by cleavage of $\{111\}$ planes, which otherwise would produce crack edges along the $\langle 112 \rangle$ directions.

A detailed analysis of MD results reveals that fracture occurs through a process of dislocation-mediated local thinning instead of cleavage. This is a unique mode of mechanical failure of thin films in the absence of out-of-plane constraints. More specifically, Figure 4.4(a) shows a 3D view of the atomic configuration of a partially

cracked film. Figures 4(b1) and (b2) respectively expose the (111) cross sections of the film that are cut at two different locations along the crack path, such that the onset and growth of the local thinning can be clearly seen. As schematically shown in Figure 4.4(c), the local thinning is mediated by dislocation glide. That is, an extended dislocation, which splits into the leading and trailing partials in FCC Cu, can glide on the conjugate $\{111\}_M$ and $\{111\}_T$ slip planes in the adjoining matrix and twin crystals. Such type of dislocations have the Burgers vector $\mathbf{b} = \langle 110 \rangle / 2$ with the non-zero component in the thickness direction of the film. As a result, gliding of those dislocations on $\{111\}_M$ and $\{111\}_T$ slip planes causes the decrease of film thickness, responsible for the local thinning and final rupture of the film. Because of symmetry, the in-plane tensile loading along the [112] direction can activate dislocations on all the equivalent inclined $\{111\}_M$ and $\{111\}_T$ slip planes symmetric about the (110) plane of the film, which eventually produce $\{111\}_M$ and $\{111\}_T$ crack surfaces, as illustrated in Figure 4.4(c). Within each twin lamella, the two inclined $\{111\}$ crack surfaces (indicated respectively by a solid and a dashed line) intersect to create an apparent $\langle 110 \rangle$ crack edge. Those characteristic $\langle 110 \rangle$ crack edges have already been seen in the 2D projected view of the fractured film in Figure 4.1(b) and Figure 4.3(d).

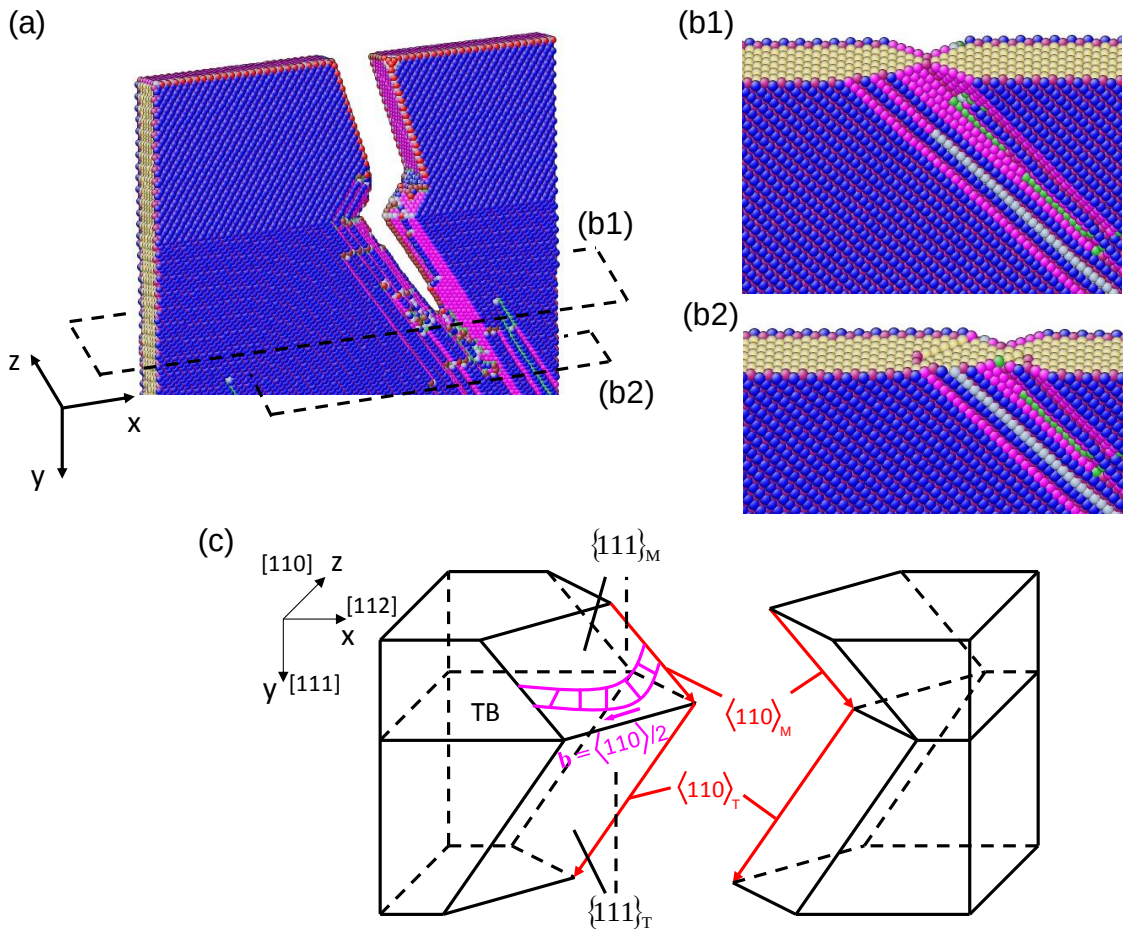

Figure 4.4 Fracture via dislocation-mediated local thinning in a thin film of nanotwinned Cu. (a) MD snapshot of a propagating crack. (b) The (111) cross sections are exposed to reveal the onset (b1) and growth (b2) of local thinning at two different locations along the crack extension path. Atoms are colored with the same scheme as in Figure 4.2. (c) 3D schematic showing the active mode of dislocation glide as well as the resultant crack surfaces and edges. Dislocations dominantly glide on the inclined {111} slip planes, so as to cause the local shear thinning and produce the $\{111\}_M$ and $\{111\}_T$ crack surfaces. Within each twin lamella, the two inclined $\{111\}$ crack surfaces (indicated respectively by a solid and a dashed line) intersect to create the $\langle 110\rangle$ crack edge (indicated by the red arrow).

We further analyze the nature of active dislocations responsible for the thinning and fracture of nanotwinned Cu thin films. Figure 4.5 shows a MD snapshot where several dislocations glide in between the upper and lower twin boundaries. The red parallelogram

indicates an inclined $\{111\}$ slip plane containing an extended dislocation (between two red curves) that splits into the leading and trailing partials enclosing a stacking fault ribbon in between. This is a screw dislocation with the Burgers vector $\mathbf{b} = \langle 110 \rangle / 2$, as illustrated on the schematic Thompson tetrahedron in Figure 4.5. Such type of screw dislocation occurs most frequently in MD simulations. This is because these screw dislocations are subjected to the largest resolved shear stress (corresponding to the largest Schmid factor of 0.41) among the twelve possible $\{111\}\langle 110 \rangle$ slip systems in the twin lamella [55], given the in-plane tensile load parallel to the twin boundary. From the standpoint of deformation compatibility, the Burgers vectors of these screw dislocations (i.e., $\mathbf{b} = \langle 110 \rangle / 2$) have non-zero components in both the in-plane loading direction and the out-of-plane thickness direction. As a result, gliding of these dislocation near the crack tip can produce in-plane elongation to accommodate the applied tensile load and meanwhile reduce film thickness to enable the relaxation of out-of-plane stresses. Moreover, gliding of a screw dislocation on the active $\{111\}_{\mathrm{M}}$ (or $\{111\}_{\mathrm{T}}$) slip plane can produce a relative shear displacement between two adjacent $\{111\}_{\mathrm{M}}$ (or $\{111\}_{\mathrm{T}}$) atomic planes. As more screw dislocations glide on this active $\{111\}_{\mathrm{M}}$ slip plane, the shear displacement gradually increases and eventually produces a shear-off mode of fracture on the $\{111\}_{\mathrm{M}}$ (or $\{111\}_{\mathrm{T}}$) slip plane as illustrated in Figure 4.4(c). In addition, we note that the Burgers vectors of these screw dislocations (i.e., $\mathbf{b} = \langle 110 \rangle / 2$) are parallel to the intersection between the conjugate $\{111\}_{\mathrm{M}}$ and $\{111\}_{\mathrm{T}}$ slip planes at twin boundary, thus facilitating the slip transmission of screw dislocations across twin boundary.

The TEM images in Figure 4.1 also show an intriguing characteristic of fracture path which features several short crack edges on twin boundaries, as highlighted by circles. Since the in-plane tensile load was primarily parallel to twin boundaries, the resolved normal and shear stresses on twin boundaries were small. As a result, there was a lack of direct driving forces to produce those short crack edges on twin boundaries. To understand the origin of those crack edges, we note that in both the in situ TEM experiment by Shan et al. [72] and the earlier studies of fracture of thin metal foils [145], it has been found that small-sized nanocracks frequently formed in front of the main crack; and as the tensile load increased, nanocracks grew and coalesced with the main crack. To explore the possible effect of crack coalescence on the formation of crack edges at twin boundaries, we setup two pre-cracks on the two opposite edges of a nanotwinned thin film, as shown in Figure 4.6(a). Under an in-plane tensile load parallel to twin boundaries, the two edge cracks grow in the opposite direction, producing zigzag crack paths, similar to the case of a single pre-crack in Figure 4.3. Interestingly, as the two cracks meet at a twin boundary, a small ligament typically arises in between two crack tips; in experiments, such meeting with an offset between the two crack tips is conceivably more common than the exact meeting without an offset. As shown by a sequence of MD snapshots in Figure 4.6(b-d), the final crack coalescence occurs through rotation and tearing of this small ligament, thereby producing a pair of short crack edges on the twin boundary as circled in Figure 4.6(d). Hence, this MD simulation not only reproduces the formation of short crack edges on twin boundaries as observed in the TEM image of Figure 4.1(b), but also demonstrates that MD simulations can help clarify the unexpected features and thus reveal the associated microscopic mechanisms during deformation and fracture.

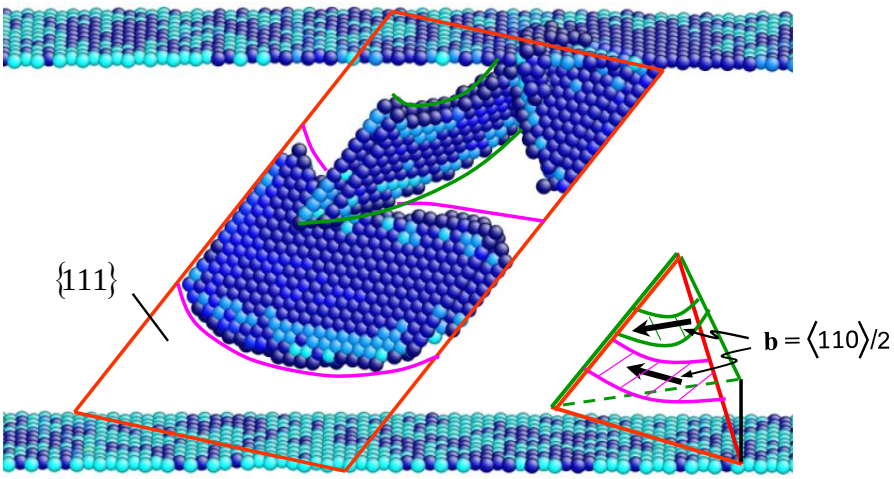

Figure 4.5 A MD snapshot showing the active screw dislocations on the $\{111\}\langle 110\rangle$ slip systems, as illustrated by the Thompson tetrahedron. Atoms are colored by the central symmetry parameter, showing the twin boundary and the stacking fault of screw dislocation.

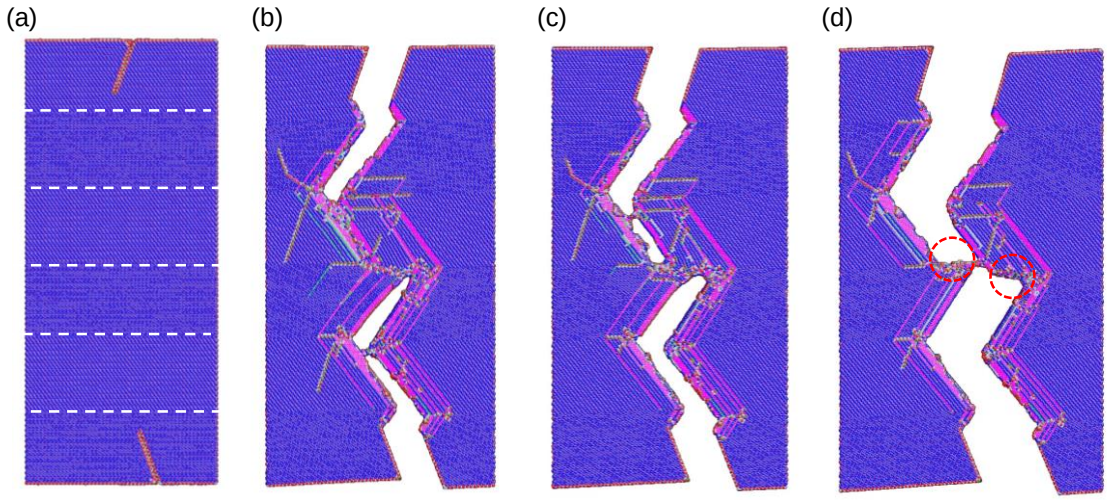

Figure 4.6 MD snapshots showing the formation of short crack edges on twin boundaries. (a) MD setup containing two pre-existing edge cracks. The dashed lines indicate twin boundaries. (b-d) A sequence of atomic structures showing the process of crack coalescence, involving the local rotation and tearing of a small ligament between the two crack tips meeting at a twin boundary. The applied tensile strains in (b) to (d) are 20.3%, 23.7%, and 38.5%, respectively. Atoms are colored with the same scheme as in Figure 4.2.

The above MD simulation results also reveal several toughening mechanisms by nanotwins. First, twin boundaries can obstruct the movement of dislocations emitted from the crack tip. The obstructed dislocations shield the crack tip from the applied load by producing back stresses near the crack tip [146]. As a result, the applied load has to increase to drive the dislocation emission and crack extension processes. Second, due to the periodic deflections of the crack path by twin boundaries, fracture occurs through zigzag cracking. Compared to a straight crack path, the zigzag mode of crack growth increases the effective crack length and thus causes more energy dissipation through irreversible plastic processes near the zigzag crack faces. Third, twin boundaries are coherent and thus have higher fracture resistances than the typical incoherent grain boundaries in nanocrystalline metals [60]. Figure 6 provides an example of fracture at the twin boundary through plastic tearing, which can cause more energy dissipation than the brittle fracture of weak incoherent boundaries. Fourth, the high density and accordingly small spacing of twin boundaries in nanotwinned metals can further enhance the aforementioned toughening mechanisms.

When the thickness of nanotwinned Cu thin films is around 100 nm or above, previous experimental and computational studies [73] have shown that a large number of dislocations on different $\{111\}\langle 110\rangle$ slip systems were emitted from the crack tip and they interacted with twin boundaries ahead of the crack. As a result, a high density of dislocations was accumulated on twin boundaries, transforming a clean and coherent twin boundary into a dislocation wall with increasing resistances to slip transmission. The dislocation walls effectively resisted crack propagation, such that either the crack was arrested by a twin boundary or the nanoscale twins became crack bridging ligaments. In this work, the nanotwinned sample is very thin. As a result, the type of active dislocation

slip systems and the interaction between dislocations are significantly restrained, resulting in the operation of a dominant type of screw dislocations as shown in Figure 4.5. The persistent slip of these dislocations leads to local thinning and crack extension through twin boundaries.

4.3 Conclusions

To conclude, our molecular dynamics simulations have revealed the zigzag mode of cracking in a free-standing thin film of nanotwinned Cu, which arises due to periodic deflections of the crack by twin boundaries. The microscopic mechanism of fracture involves the screw dislocation-mediated local thinning ahead of the crack, instead of cleavage of close-packed planes. The screw dislocation-induced thinning and fracture result in a unique footprint of the $\langle 110 \rangle$ -oriented crack edges as shown by both the present molecular dynamics simulations and the previous in situ TEM experiments [72]. Our results reveal the toughening mechanisms by nanotwins, including the twin boundary obstruction of dislocation glide, twin boundary deflection of crack path, strong fracture resistance of coherent twin boundary, and high twin boundary density to enhance the aforementioned toughening mechanisms. While the present study is focused on the nanotwinned thin film of FCC Cu, the fracture mechanism of dislocation-mediated thinning is expected to prevail during the mechanical failure of other types of thin FCC metal films as well. The combined MD and (previous) in situ TEM studies provide strong support for the operation of such fracture mechanism. Mechanistic insights gained in this work could be also valuable for studying fracture in nanotwinned crystals with other types of lattice structure [14, 34, 147].

CHAPTER 5. HETEROGENEITY- AND DEFECT-CONTROLLED STRENGTH AND MECHANISMS IN ADDITIVELY MANUFACTURED STEELS

Here we report that 316L stainless steels (SS) made by L-PBF can have hardness values that are over four times higher than that predicted from the H-P scaling law. Effects of these hierarchical heterogeneities and defects on material strengthening are further studied by computational modeling. We performed *size-dependent* crystal plasticity finite element (CPFE) simulations to investigate the effects of grain-level heterogeneities as well as sub-grain heterogeneities and defects (e.g., local misorientations, cellular structures, dislocations, and LAGBs) on plastic responses. The CPFE simulations are presented in section 5.2. To gain further mechanistic insights into the strength-controlling sub-grain heterogeneities and defects, we performed molecular dynamics (MD) simulations of plastic deformation in a model of polycrystalline fcc steel (Fe-10Ni-17Cr). The MD simulations are presented in section 5.3.

5.1 High strength of AM SS with heterogeneous microstructures

The cross-sectional grain orientation and size distribution are measured by electron backscatter diffraction (EBSD) in a scanning electron microscope (SEM). Grains under EBSD exhibit a ripple pattern instead of a traditional faceted morphology. These EBSD and compositional data suggest that AM 316L SS is an unconventional material with a broad grain size distribution, a large fraction of LAGBs, and impurities. Voids are also present but the volume fraction is far less than 1% in our materials.

The hardness, strain rate sensitivity, and apparent activation volume of as-built AM 316L SS were measured by nanoindentation. Such an extraordinary strength, together with the unusual distributions of grain sizes and GBs, suggests that the strength of AM 316L SS cannot be simply defined by the H-P relation based on coarse-grained and nanostructured counterparts. These results are unexpected given the fact that AM 316L SS reported here has average grain sizes nearly three orders of magnitude larger than those of nanocrystalline metals. Yet, we obtained a set of plastic deformation kinetics parameters that are close to those of nanocrystalline metals.

The heterogeneities and pre-existing defects in as-built 316L SS can have profound impacts on the deformation mechanisms of AM 316L SS. We postulate that a large amount of LAGBs, along with local misorientations, can have strong influences on the strengthening behavior.

5.2 Crystal plasticity finite element modeling

To further understand the deformation mechanisms of AM 316L SS, we performed *size-dependent* crystal plasticity finite element (CPFE) simulations to investigate the effects of grain-level heterogeneities as well as sub-grain heterogeneities and defects (e.g., local misorientations, cellular structures, dislocations, and LAGBs) on plastic responses.

5.2.1 Grain-size-dependent crystal plasticity model

To investigate the effect of grain size distribution on the stress-strain behavior of AM SS, the classical crystal plasticity theory was extended by incorporating the grain size dependence of yield strength [119-121, 141]. The complete details of the crystal plasticity

model used in this work can be found in a recent article by Zeng et al. [141]. To apply this crystal plasticity model to AM SS, we assumed the slip resistance parameters in each grain, including $\{s_0, h_0, a, s_{sat}, m\}$, were inversely proportional to the square root of grain size d,

$$\{s_0(d), h_0(d), a(d), s_{sat}(d), m(d)\} \sim d^{-1/2} \tag{5.1}$$

In Equation (5.1), the initial slip resistances s_0 were estimated from the Hall-Petch relation mentioned in the main context (by using the by Taylor's factor of 2.5). The strain rate sensitivity m of CG SS varies from 0.007 and 0.005 for grain size d from 3.1 μm to 33 μm [148, 149]. The strain hardening related parameters $\{h_0, a, s_{sat}\}$ were determined by fitting to the experimental stress-strain curves of SS for two grain sizes of 3.1 μm and 33 μm [150]. For the 3.1 μm grain, we took h_0 = 1200 MPa, a = 2.5, s_{sat} = 1080 MPa; and for the 33 μm grain, h_0 = 1100 MPa, a = 2.4, s_{sat} = 960 MPa. To evaluate $\{h_0, a, s_{sat}, m\}$ for intermediate grain sizes, we used the above bounding values to fit the formula of $A = B + C \cdot d^{-1/2}$ where B and C are the fitting constants. The following fitting formulas were obtained

$$s_0(\text{MPa}) = 73.32 + 101.46 \cdot d^{-1/2},\ h_0(\text{MPa}) = 1053.8 + 253.31 \cdot d^{-1/2}, \tag{5.2}$$

$$a = 2.3538 + 0.2533 \cdot d^{-1/2},\ s_{sat}(\text{MPa}) = 904.5 + 303.97 \cdot d^{-1/2},\ m = 0.0041 + 0.0051 \cdot d^{-1/2}$$

To investigate the effect of sub-grain heterogeneities and defects on the stress-strain behavior of AM SS, the slip resistance parameters were assumed to be controlled by a characteristic sub-grain length scale L_c, which was much smaller than the grain size. By

fitting to the experimental stress-strain curves of AM SS, we obtained the slip resistance parameters: s_0 = 300 MPa, h_0 = 470 MPa, a = 2.3, s_{sat} = 330 MPa. The strain rate sensitivity m is 0.025, which was already measured in our experiments.

Other material properties, including elastic constants (C_{11} , C_{12} , C_{44}), twelve $\{111\}\langle 110\rangle$ slip systems, and the latent hardening matrix $\left\{q^{\alpha\beta}\right\}$, were assumed to be independent of grain size. For FCC Fe, we took $C_{11} = 260$ GPa , $C_{12} = 111$ GPa and $C_{44} = 77$ GPa ; $q^{\alpha\beta}$ = 1.0 if the slip systems α and β are coplanar and $q^{\alpha\beta}$ = 1.4 if they are non-coplanar [121].

5.2.2 Finite element model and simulation

Figure 5.1(a) shows a three-dimensional structure model of AM SS rendered in an open-source software Neper [136]. The grain sizes are widely distributed, varying from 3 μm to 30 μm. To construct this model, the first step was to pack poly-dispersed spherical particles with a prescribed distribution of diameters. The geometry of packed particles was generated from a discrete element method simulation with LAMMPS [117, 137]. In this simulation, spherical particles with diameters ranging from 3 μm to 30 μm were poured into a cubic container. The number of particles with each diameter was prescribed. The built-in Hertzian model for granular spherical particles was used to simulate the particle interactions, and the particle system was relaxed [138-140]. After relaxation, the centroids of the particles correspond to the centroids of the grains, and the diameters of the particles correspond to the grain diameters. Given the diameter and the position of the centroid of each particle, Laguerre tessellation was applied to construct the weighted Voronoi diagram

with Neper. Each Voronoi cell is a polyhedron with an irregular shape, representing a grain in the AM SS structure. The diameter and the volume of each grain were calculated with the built-in functions in Neper and were used for the calculations of the volume fraction, as shown in Figure 5.1(b). Furthermore, the fractions of particles with different diameters were carefully tuned to obtain the desired volume fraction in Figure 5.1(b). Then the sample of the AM SS structure was meshed with the built-in meshing function in Neper with four-node linear tetrahedral elements (C3D4). The meshes were imported into ABAQUS/CAE to reproduce the sample of the AM SS in ABAQUS/CAE [116].

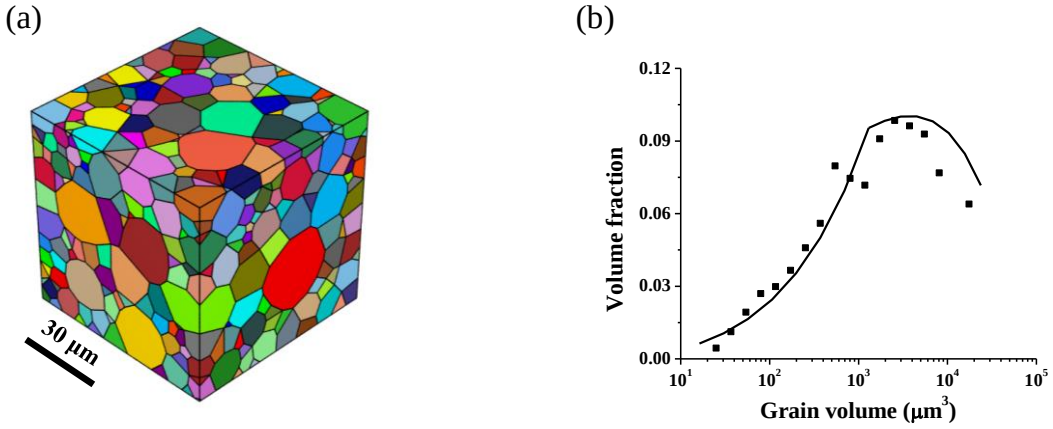

Figure 5.1 CPFE model of AM SS. (a) Structure of the heterogeneous grain-size model for CPFE simulation, showing a wide distribution of grain sizes. (b) Distribution of grain volumes (symbols) in the heterogeneous grain-size model in B, where the solid line is approximated from the measured grain area distribution from experiments.

The resulting finite element structure model of AM SS rendered in ABAQUS/CAE is shown in Figure 5.2. The overall sample geometry is 73 μm × 73 μm × 73 μm (x × y × z), with 88944 elements. Displacements and tractions are continuous at grain boundaries,

meaning no separation or sliding between every pair of adjoining grains. Using the finite element structure model of AM SS, crystal plasticity simulations were performed to simulate the uniaxial compression of AM SS under the plane-strain condition. The orientation of grains was assigned randomly in terms of three Euler angles, $\{\theta, \varphi, \Omega\}$, representing rotations from the crystal basis to the global basis [121]. A user material subroutine VUMAT was developed in ABAQUS/EXPLICIT to implement the grain-size-dependent crystal plasticity model described above. With reference to Figure 5.2, the boundary conditions of the AM SS sample were prescribed as follows: on $x = 0$ surface, the displacement in the x direction is zero ($u_x = 0$); on $y = 0$ surface, the displacement in the y direction is zero ($u_y = 0$); on $z = 0$ surface, the displacement in the z direction is zero ($u_z = 0$); on the $y = 73$ µm and $z = 73$ µm surfaces, the traction is zero; on $x = 73$ µm surface, the velocity in the x direction is constant ($v_x = 7.3 \times 10^{-4}$µm/s), corresponding to an applied strain rate of 10^{-5}/s.

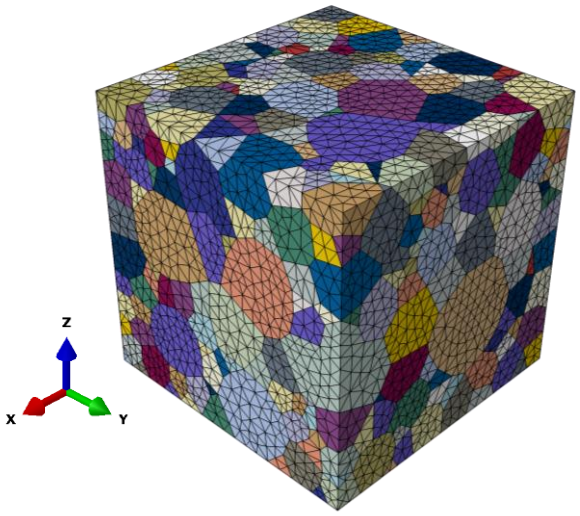

Figure 5.2 The finite element structure of AM SS render by ABAQUS/CAE. The meshes are colored with respect to the grains they belong to. The coordinate system used in simulations is shown at the left corner.

5.2.3 CPFE simulation results

While EBSD measurements of AM SS revealed a broad distribution of grain sizes and grain areas, our grain size-dependent CPFE simulations in Figure 5.3 indicate that the yield strength and strain hardening are not directly controlled by the length scale effect of EBSD-identified grains, which mostly involve HAGBs (> 10^{o}). Specifically, we constructed a heterogeneous grain-size model (Figure 5.1(a)) with a wide distribution of grain size (in the range of 3-30 μm) and hence grain volume (Figure 5.2(b)) similar to that of AM SS. We developed a grain size-dependent constitutive model, in which both the yield strength and strain hardening properties within each grain depend on the local grain size.

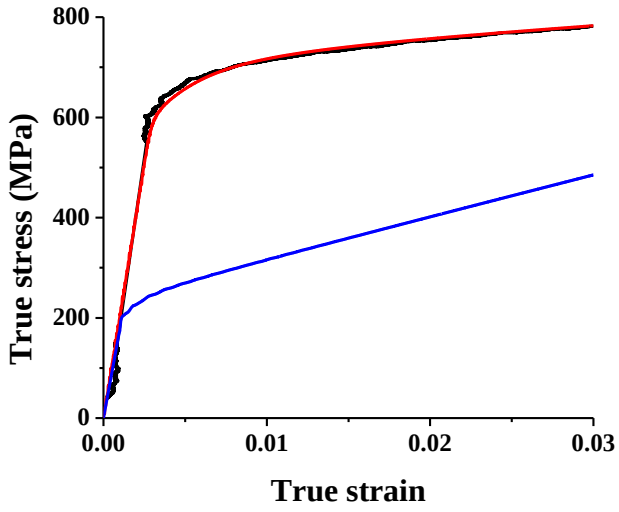

Figure 5.3 Size-dependent crystal plasticity finite element (CPFE) AM steel. Comparison of the stress-strain responses from the uniaxial compression experiment (black curve), the CPFE simulation with a heterogeneous grain-size model (blue curve), and the CPFE simulation with a sub-grain heterogeneity/defect model (red curve).

The corresponding constitutive parameters were determined by fitting the experimental data of 316L SS that closely follows the H-P equation between yield strength σ_Y and grain size d, i.e., σ_Y= 183.31 + 253.66/$\sqrt{d}$ (MPa). Using this grain size-dependent CPFE model, we simulated the stress-strain response of uniaxial compression of AM 316L SS (the blue curve in Figure 5.3), which predicted the yield strength and strain hardening responses that were much lower than those from experimental measurements (the black curve in Figure 5.3, where the 0.2% offset yield strength is slightly lower than the measured hardness strength). This result lends direct support to our earlier analysis of the important contribution of sub-grain heterogeneities and defects to the strength of AM 316L SS. To estimate an effective sub-grain length scale (denoted as L_c) that controls the strength of AM 316L SS, we modified the above grain size-dependent CPFE model; namely, the yield strength obeys the aforementioned H-P equation through L_c instead of grain size, such that σ_Y = 183.31 + 253.66/ $\sqrt{L_c}$ (MPa). The simulated stress-strain curve of uniaxial compression is plotted as the red curve in Figure 5.3. The fitting value of L_c is ~205 nm (based upon experimental compression curves). While it is difficult to clearly identify a specific heterogeneity/defect feature corresponding to L_c, this result reinforces the notion that the strength of AM SS is controlled by the collective effect of sub-grain heterogeneities and defects, instead of grains with HAGBs.

5.3 Molecular dynamics modeling

To gain further mechanistic insights into the strength-controlling sub-grain heterogeneities and defects, we performed molecular dynamics (MD) simulations of plastic deformation in a model of polycrystalline fcc steel (Fe-10Ni-17Cr).

5.3.1 Atomistic modal and MD simulation

To study the atomic-level deformation mechanisms in AM steel, we built a quasi-two-dimensional atomistic model of steel with columnar grains, as shown in Figure 5.4. Figure 5.5(a) and Figure 5.5(b) show the corresponding atomic structures rendered by an open source software OVITO [151]. Atoms were colored based on a common neighbor analysis: atoms in a local FCC structure, corresponding to the perfect FCC lattice inside grains, were colored green; atoms in local HCP structure, corresponding to the stacking faults, were colored red; atoms in local non-perfect crystal structure, corresponding to the grain boundaries, were colored white. Figure 5.5(c) and Figure 5.5(d) show the atomic structure rendered by ATOMEYE [118], where the atoms were colored by the central symmetry parameter.

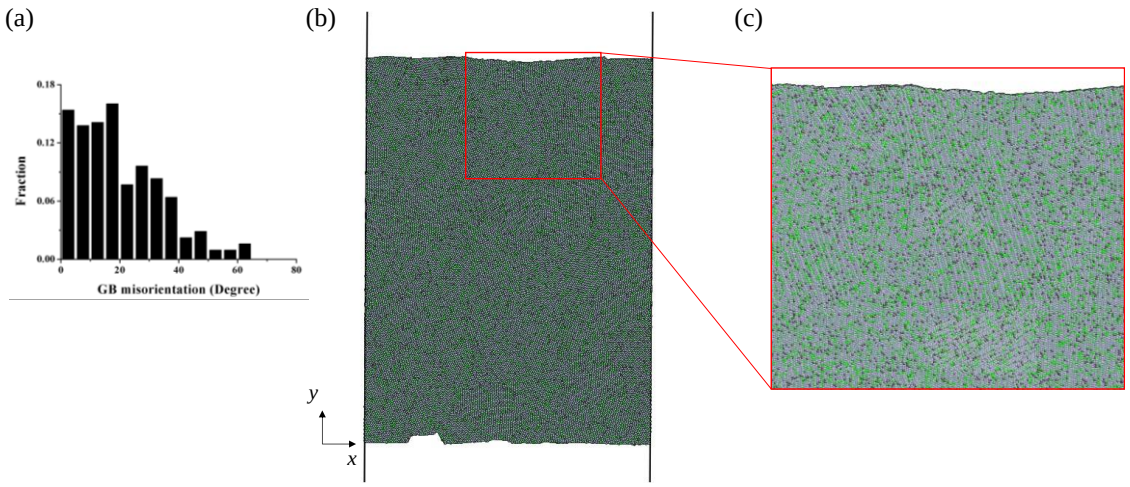

Figure 5.4 Atomistic model of steel used for molecular dynamics (MD) simulations. (a) Histogram of GB misorientations, showing the high fractions of low-angle GBs (misorientation less than 10°). (b) A MD snapshot of a polycrystalline steel (Fe-10Ni-17Cr) model under uniaxial tension in the *x* direction. (c) A magnified local region corresponding to Figure. 5.5 (a) and (b) in the paper. The scheme of atom coloring in B and C is as follows: Fe (grey); Cr (Green); Ni (Black).

To generate this structure, we first assigned random points in the plane and applied Voronoi tessellation (with a built-in function Voronoi command in Matlab) to construct the Voronoi diagram. Then we cut the single crystal lattice of pure FCC Fe into polygons for fitting into different grain domains of the AM SS structure. The thickness direction of each grain is aligned with the <112> direction. The in-plane orientation was randomly assigned from a normal distribution with the mean of 90° and the standard deviation of 15°. Figure 5.4(a) shows the distribution of grain boundary misorientations between any neighboring grains. It is seen that the resulting AM SS sample have a majority of low angle grain boundaries. Grains across the right and left edges of the simulation box were carefully constructed to avoid artificial boundaries on these edges that were caused by periodic boundary conditions. To achieve the same composition as SS in our MD model, 10% and 17% of Fe atoms were randomly selected and, respectively, replaced by Ni and Cr atoms, as shown in Figure 5.4(a) and (b).

We performed MD simulations with an embedded atom method (EAM) potential of Fe-Ni-Cr alloys [152] using LAMMPS. The MD time step is 1 fs. In MD simulations, the top and bottom surfaces are traction free, while the sample thickness is fixed, corresponding to the plane-strain condition. Periodic boundary conditions are imposed in the x and thickness directions. We first relaxed the sample for 500 ps at the temperature of 300 K and zero stresses using a Nose-Hoover thermostat and barostat. This process eliminated most of the unfavorable features in grain boundaries with high energies. The relaxed sample of AM SS has an in-plane dimension of 50.4 nm × 75 nm, and is 1.75 nm in thickness. The number of atoms in the system is 576,336. Then we simulated uniaxial

tensile behaviors of AM SS by applying a tensile strain rate of $1\times10^{8}/s$ in the x direction. The system temperature was maintained at 300 K using the Nose-Hoover thermostat.

5.3.2 MD simulation results

Since many large grains in AM 316L SS exhibited local misorientations inside grains, our MD simulations focused on the LAGBs (< 10°, see Figure 5.4(a)). Under the applied axial load, MD simulations revealed that plasticity in this steel sample was mediated by the motion of dislocations, stacking faults, and twins. Of particular interest is the plastic deformation processes associated with LAGBs. As an example, we highlight in Figure 5.5(a) a LAGB that contains an array of dislocations. During loading, this LAGB migrated via gliding of GB dislocations (Figure 5.5(b)). Most interestingly, Figure 5.5(c) and Figure 5.5(d) directly reveal the lattice misorientation across the two adjoining grains at this LAGB. Such misorientations can be correlated with the similar features revealed by IPFOM in TEM with the continuous variation of color and accordingly misorientations within individual grains. This MD result suggests that the LAGBs and equivalent dislocation boundaries can act as an important type of sub-grain defect structures that divides the apparently large grains detected from EBSD measurements and thus elevates the strength of AM SS. Moreover, this type of GB can dynamically evolve via the motion of constituting dislocation arrays, which may interact with other intra-grain dislocations and twins so as to contribute to the strain hardening and tensile ductility in AM SS.

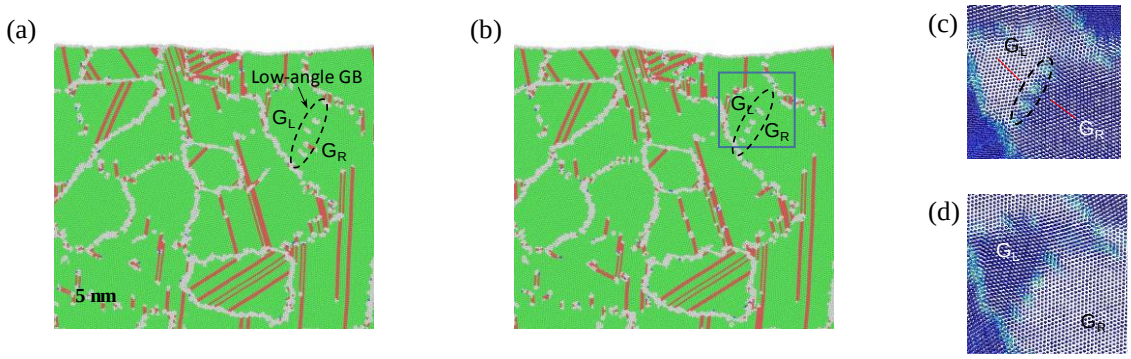

Figure 5.5 MD snapshots of a deformed polycrystalline steel (Fe-10Ni-17Cr) sample; the out-of-plane direction is <112>. The dashed ellipse in (a) indicates a low-angle grain boundary (GB), which effectively consists of an array of dislocations. The applied loading causes the migration of this GB, as shown in (b). (c)-(d). Local lattice misorientation across the small-angle GB between grains GL and GR, corresponding to the boxed region in (b). In (c), the viewing direction is tilted such that the out-of-plane direction of GL is aligned with <110>, while in G, the out-of-plane direction of GR is <110>. The change in contrast of the lattice between GL and GR in F (and in G as well) indicates a misorientation between GL and GR.

5.4 Conclusions

Our combined experimental and modeling study provides compelling evidence of the crucial effects of structural and chemical heterogeneities as well as the unique sub-grain defects (e.g., LAGBs and local misorientations) on the strength and controlling deformation mechanisms in AM steels. Our results suggest that the complex and processing-specific microstructures in AM materials, as reported in this work and recent literature, make it challenging to delineate the material strength using the Hall-Petch scaling law based on a single parameter of grain size determined primarily by HAGBs or any other single strength-controlling mechanism. Broadly, this work demonstrates that the mechanical properties of AM metals and alloys are controlled by their microstructural heterogeneities and sub-grain defects uniquely produced during additive manufacturing.

CHAPTER 6. PLASTICITY IN NANOSCALE BCC TUNGSTEN

Using these *in situ* fabricated samples, we demonstrate that twinning is the dominant deformation mechanism in nanoscale W crystals at room temperature and low strain rates. Such mechanical twinning is pseudoelastic, as evidenced by the reversible detwinning during unloading. Section 6.1 is focus on the experimental observations of twinning deformation. Atomistic simulations are performed to provide insights into the twinning dominated deformation mechanism in these nanoscale BCC crystals. Atomistic modeling of twinning dominated deformation is presented in section 6.2. In section 6.3, we further find that the loading orientation governs the competition between twinning and dislocation slip. Section 6.4 is focus on the atomistic modeling of dislocation dominated deformation. Section 6.5 provides further discussion on the competition between twinning and dislocation slip.

6.1 In situ atomic-scale observation of twinning dominated deformation in nanoscale body-centered cubic crystals

Figure 6.1 shows the *in situ* uniaxial compression of a W bicrystal nanowire at room temperature under a strain rate of $\sim 10^{-3}$ s^{-1}. This sample contains a large single crystal whose $[\bar{1}10]$ direction is aligned with the overall axial direction of the bicrystal nanowire. Since the deformation events are primarily observed in this large crystal, the bicrystal sample is referred to as a $[\bar{1}10]$-oriented nanowire. TEM imaging is aligned with the transverse $[110]$ direction (Figure 6.1(a)). Upon compressive loading, the nanowire

initially undergoes elastic deformation. As the lattice strain in the relatively large $[\bar{1}10]$-oriented crystal accumulates to around 4.9% (Figure 6.2), a small twin embryo nucleates from the intersection between the grain boundary and free surface, and transverses the entire sample under continued loading (Figure 6.1(b)). Figure 6.1(d)-(f) confirms that the observed deformation band in the $[\bar{1}10]$-oriented crystal is a twin band with the active twinning system of $[\bar{1}11](\bar{1}12)$, as evidenced by the Fast-Fourier transform pattern (Figure 6.1(d)-(e)) and zoomed-in image (Figure 6.1(f)). At the onset of twinning, the resolved shear stress on the $(\bar{1}12)$ plane on which the twin forms is estimated to be about 9 GPa based on the lattice strain (Figure 6.2). After a complete twin band forms, the lattice strain is released to about 1.3% (Figure 6.2). A further increase in the applied load causes thickening of the twin band, thus producing an increased amount of inelastic strain (Figure 6.1(c)). Moreover, we observe that the grain boundary alone can serve as the effective nucleation site for deformation twins (in Figure 6.3).

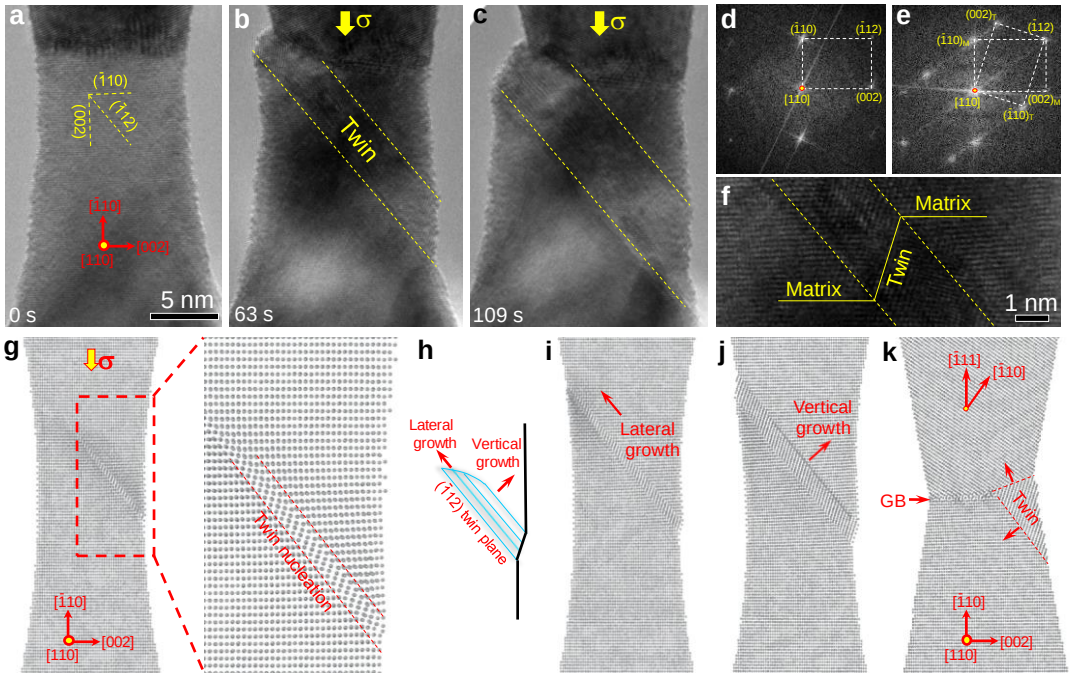

Figure 6.1 Deformation twinning in a W bicrystal nanowire under $[\bar{1}10]$ compression. (a-c) Sequential TEM images showing deformation twinning in a W bicrystal nanowire (15 nm in diameter) at room temperature under a strain rate of 10^{-3} s^{-1}, which is loaded along $[\bar{1}10]$ and viewed along $[110]$. (d-e) Fast-Fourier transformed pattern of the pristine W bicrystal and the deformation twin, respectively. (f) An enlarged TEM image showing the deformation twin. (g) A MD snapshot and zoomed-in image showing the nucleation of a deformation twin embryo in a W single crystal nanowire. (h) Schematic of the lateral expansion and vertical thickening of a twin band. (i-j) MD snapshots showing the lateral expansion and vertical thickening of twin. (k) Nucleation and growth of a deformation twin in a W bicrystal nanowire.

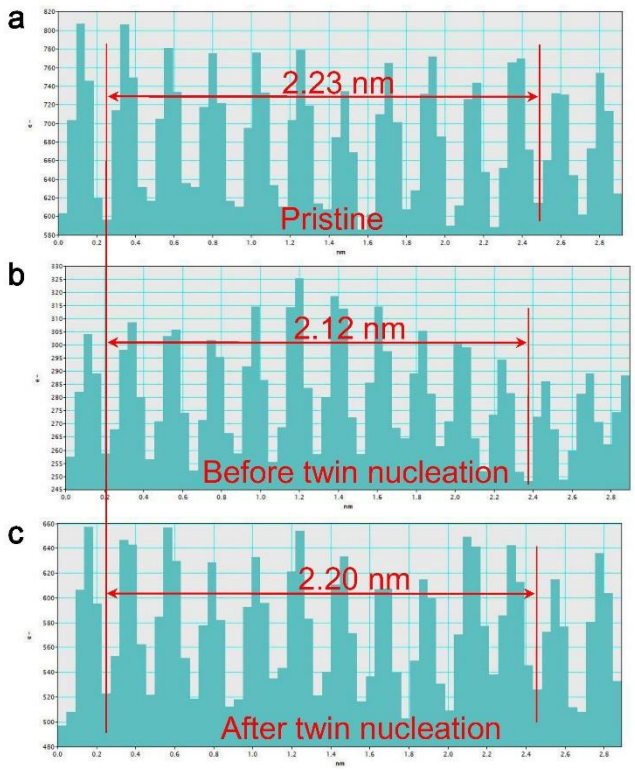

Figure 6.2 The inter-planar spacing evolution of the $(\bar{1}10)$ plane during compressive loading. The strain, and accordingly stress, of twin nucleation is estimated by measuring the inter-planar spacing of the $(\bar{1}10)$ planes. (a-b) The inter-planar spacing of the $(\bar{1}10)$ plane decreases gradually as the elastic compressive strain increases. At an elastic strain of 4.9 %, the W bicrystal nanowire yields suddenly via the emission of a deformation twin. Young's modulus of W along $\langle 110 \rangle$ direction is 389 GPa (see Supplementary Discussion 1), and thus the estimated yield strength is about 19.2 GPa. Since deformation twinning occurs via shear on the $[\bar{1}11](\bar{1}12)$ twin system, the corresponding Schmid factor is 0.47 and the resolved shear stress for twin formation is estimated as 9 GPa. (c) After the formation of a deformation twin band, the lattice strain is reduced to about 1.3%.

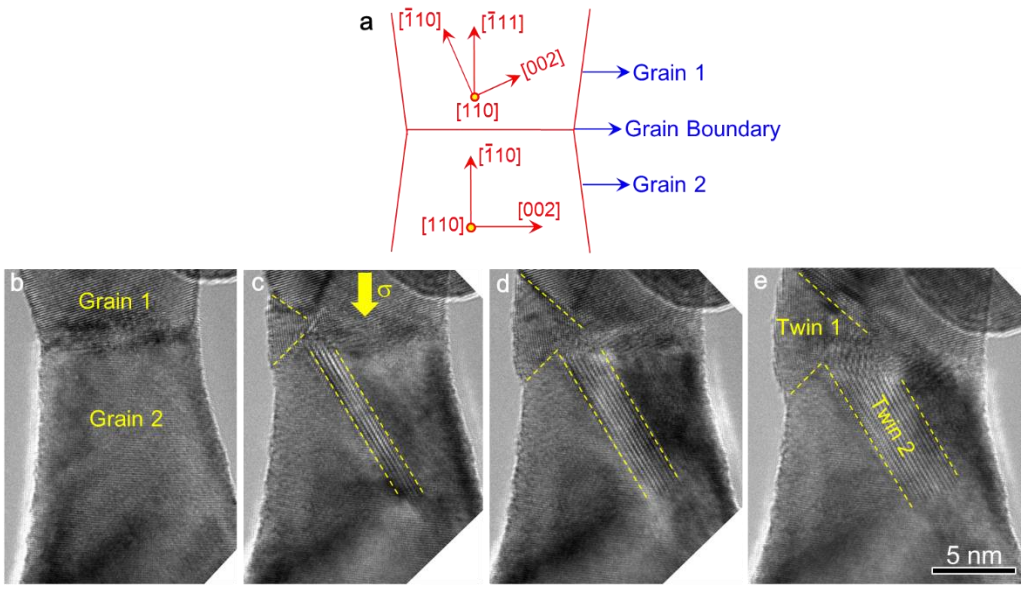

Figure 6.3. The nucleation of deformation twins at the intersection between a grain boundary (GB) and free surface in a W bicrystal nanowire under compression. (a) The crystallographic orientations of the two adjoining grains in the W bicrystal nanowire: the upper grain is loaded along $[\bar{1}11]$ while the lower grain is $[1\bar{1}0]$. (b) The pristine W bicrystal nanowire. (c) Under compression, deformation twins are observed to nucleate from both the GB (denoted as Twin 2) and the GB/surface intersection (denoted as Twin 1). (d-e) Twin 1 grows layer-by-layer into both grains, while the growth of Twin 2 mainly occurs inside Grain 2.

Deformation twinning in W bicrystals is pseudoelastic, as manifested through reversible detwinning upon unloading. That is, during compressive loading, the W bicrystal experiences large deformation via the formation of a deformation twin (Figure 6.4(a)-(b),(f)-(g)), the thickness of which is about 4 nm just before unloading (Figure 6.4(g)). However, upon unloading, deformation mainly occurs at the twin boundary via a layer-by-layer detwinning (Figure 6.4(c),(h)). Detwinning proceeds in the same fashion as twinning through the nucleation and propagation of twinning dislocations, but in the reverse direction. As a result, the twin thickness is gradually reduced, returning the bicrystal to its

original shape without apparent defects after a complete unloading (Figure 6.4(d),(i)). Pseudoelasticity is also manifested in the stress-strain curve, which demonstrates the recovery of the initial zero stress and strain values after a loading/unloading cycle (Figure 6.4(j)). During multiple loading/unloading cycles, the deformation twin is always observed to nucleate at the same location (Figure 6.4(e)). The pseudoelastic twinning is also observed in our MD simulations. Figure 6.4(k) shows MD snapshots of a detwinning process during unloading, which occurs layer-by-layer at the twin boundary via $1/6[\bar{1}\bar{1}1]$ dislocations nucleated on adjacent $(\bar{1}12)$ planes, consistent with TEM observations. The driving force of detwinning can be attributed to both the unloading and the deformation incompatibility at the intersection between grain boundary and twin band. While such geometrical incompatibility can be partially released by deformation near the grain boundary during loading, it cannot be completely accommodated due to the strong cohesion of grain boundary, thus resulting in back stresses acting on the twin band. Once the unloading begins, these back stresses can drive the formation of twinning dislocations near the grain boundary, whose glide along the twin boundary causes the thinning of the twin band.

In addition to the $\langle 110 \rangle$ loading, we observe that deformation twinning dominates for several other loading orientations tested, including $\langle 100 \rangle$ tension and $\langle 111 \rangle$ compression, as shown in Figure 6.5.

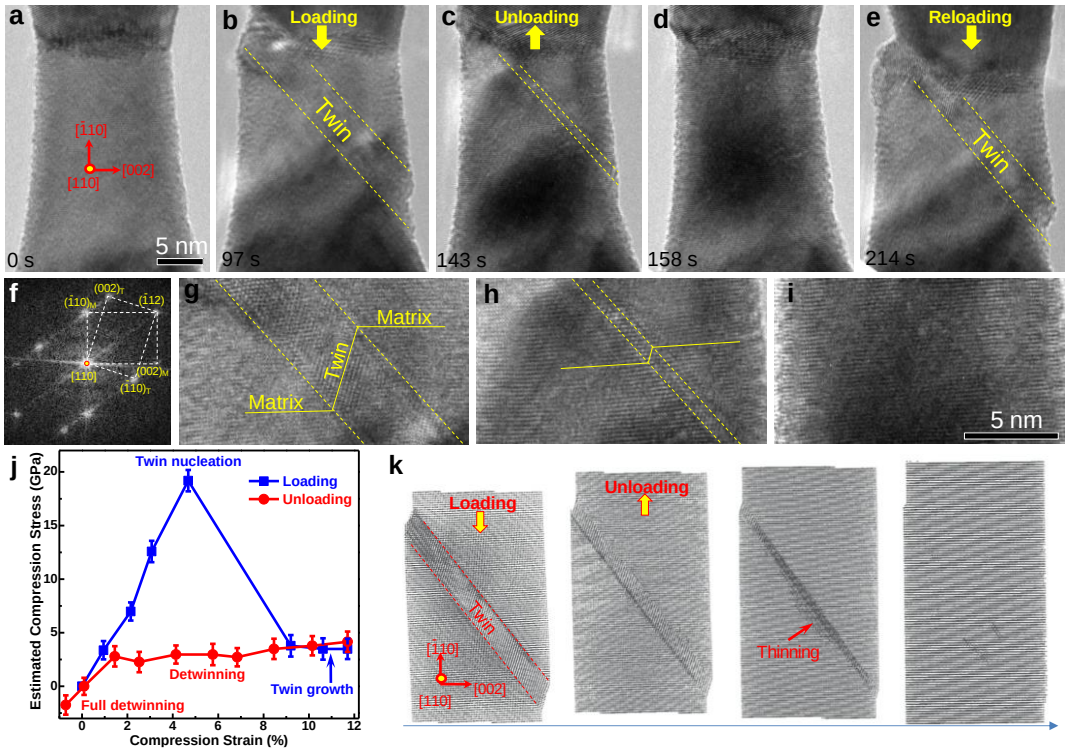

Figure 6.4 Reversible deformation twinning and detwinning processes in a W bicrystal nanowire under cyclic loading. (a) A pristine W bicrystal nanowire with the diameter 14.7 nm as viewed along $[110]$ and loaded along $[\bar{1}10]$. (b, g) Under compression, the deformation twin nucleates and grows to about 4 nm in thickness. (c, h) A layer-by-layer detwinning process occurs upon unloading (also see Supplementary Movie 3). (d, i) After complete detwinning, the W bicrystal recovers its original shape. (e) A deformation twin nucleates at the same place in subsequent deformation cycles. (f) The Fast-Fourier transformed pattern of the deformation twin. (j) Stress versus strain curve during compressive loading and unloading, showing the pseudoelastic response. The stress is estimated based on the lattice strain, while the compressive strain is measured from the change of nanowire length. (k) MD snapshots, showing the twinning and detwinning process similar to TEM observations.

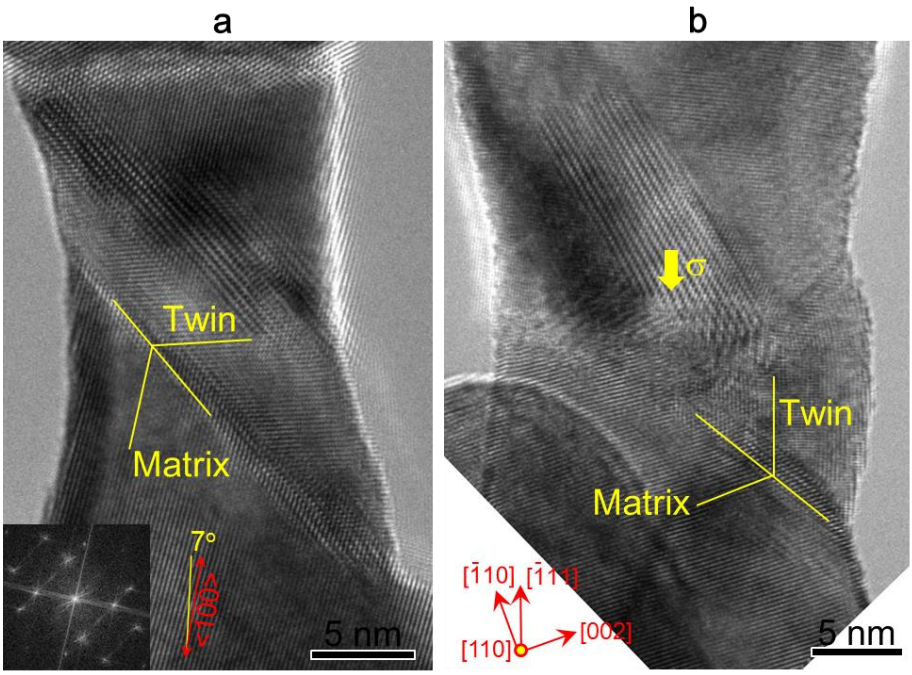

Figure 6.5 Orientation-dependent deformation twinning in W nanoscale crystals. All samples were viewed along the [110] direction. Deformation twinning occurred under (a) [100] tension and (b) $[\bar{1}11]$ compression.

6.2 Atomistic modeling of twinning dominated deformation in BCC W

To understand the twinning mechanism of nanoscale W crystals, we performed molecular dynamics (MD) simulations of both single and bicrystal W nanowires (Figure 6.1(g)-(k)). The simulations of twinning, detwinning and dislocation mediated deformation in W nanowires were obtained by MD using LAMMPS. The temperature of the system was maintained at 300K and the time step was 1fs. The Ackland-Thetford-Finnis-Sinclair potential of W was used in MD simulations. The applied strain rate was 10^8 s^{-1} for both $[\bar{1}10]$ and [112]compression. All of the NWs have circular cross sections. Some of the NWs have uniform diameter along the NW length, while others were constructed by

creating a tapered solid of revolution about the NW axis. To create the bicrystal, a $\langle 111 \rangle$ and $\langle 110 \rangle$ oriented single crystals (see Figure 6.1(k) for complete orientations) were bonded through the nature of the interatomic cohesion.

In the $[\bar{1}10]$-oriented single crystal, a twin embryo initially forms from the surface (Figure 6.1(g)) and expands laterally to penetrate the whole nanowire (Figure 6.1(h)-(i)). Then, the twin band thickens through a layer-by-layer vertical growth at the twin boundary via sequential nucleation of $1/6[\bar{1}11]$ twinning dislocations on adjacent $(\bar{1}12)$ planes (Figure 6.1(j)). The resolved shear stress on the $(\bar{1}12)$ plane for twin formation in MD is about 8 GPa, which is on the same order as the experimental estimate. The bicrystal nanowire in MD exhibits twin nucleation and growth from the intersection between grain boundary and free surface (Figure 6.1(k)), which penetrates into both crystals, similar to the observations in some of our experiments (Figure 6.3). This grain boundary controlled detwinning process has been observed in our MD simulations, as shown in Figure 6.6.

These atomistic studies also show that deformation twinning in nanoscale W crystals is controlled by surface nucleation. Irrespective of types of surface sites and shear modes used in the simulations, the twin embryo is always able to nucleate from the free surface and grow into a twin band in a $[\bar{1}10]$-oriented W nanowire at the characteristic load level measured in experiments. Overall, these MD results compare favorably with our experimental observations.

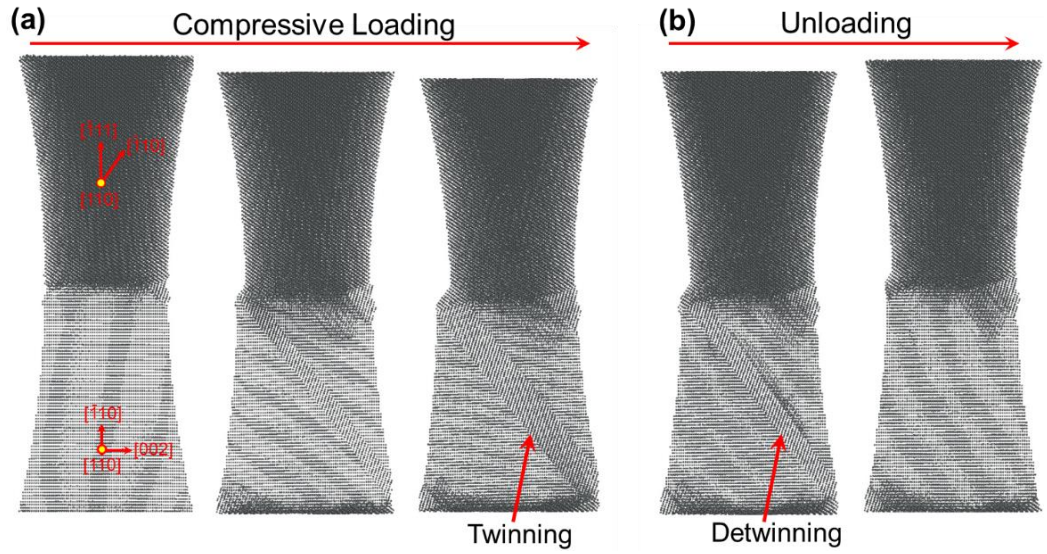

Figure 6.6 MD simulations of twinning and detwinning mediated by a grain boundary in a W bicrystal nanowire. (a) A twin band (indicated by the red arrow) forms during compressive loading of the bicrystal nanowire, and (b) detwinning occurs upon unloading due to the deformation incompatibility at the intersection between the twin band and the grain boundary.

6.3 Dislocation dominated deformation in BCC W

We find that dislocation slip prevails under $\langle 112 \rangle$ loading, for both tension and compression. Figure 6.7 shows the dislocation mediated plastic deformation of a W bicrystal under $[112]$ compression. Initially, the bicrystal is nearly pristine without observable dislocations (Figure 6.8(a)). Under compressive loading, dislocations nucleate simultaneously from multiple sources with the estimated shear stress of about 7.2 GPa on the (101) slip plane (Figure 6.7(a)-(b)), leading to the yielding of W bicrystal. Most dislocations appear to nucleate as dipoles (Figure 6.7), which are likely dislocation half loops on (101) planes. It is worth noting that most dipoles lie on the same slip plane, though a few involve dislocations on adjacent slip planes (Figure 6.7 and Figure 6.8-6.10).

The dislocations in the dipoles are mobile, resulting in their expansion on the (101) slip planes after nucleation (Figure 6.7(e)-(f)).

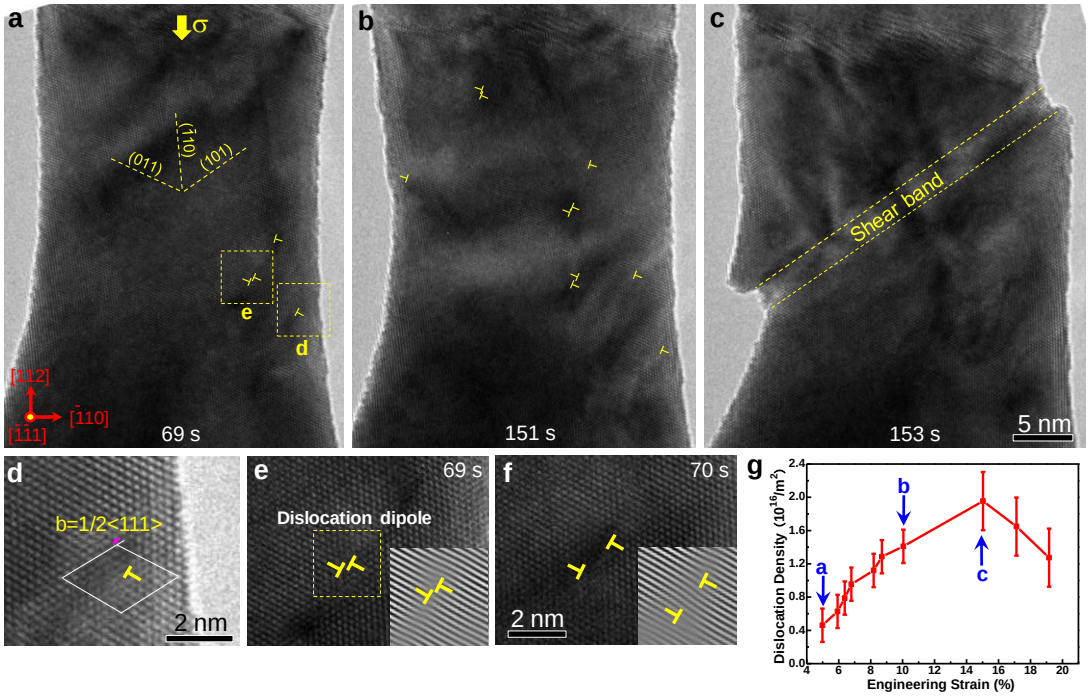

Figure 6.7 Dislocation dynamics inside a W bicrystal nanowire under [112] compression. (a-c) Sequential TEM images showing the deformation of a W bicrystal nanowire under $[112]$ compression, as viewed along $[\bar{1}\bar{1}1]$, exhibiting the nucleation of dislocations and formation of a shear band. Dislocations are marked by an upside-down "T". (d) Analysis of the Burgers vector of a dislocation nucleated from side surface indicates a $1/2\langle 111\rangle$-type mixed dislocation. (e-f) Sequential TEM images showing the nucleation and expansion of a dislocation dipole under $[112]$ compression. (g) The statistical dislocation density evolution with the compressive strain; blue arrows indicate the states of deformation shown in TEM images of (a), (b) and (c).

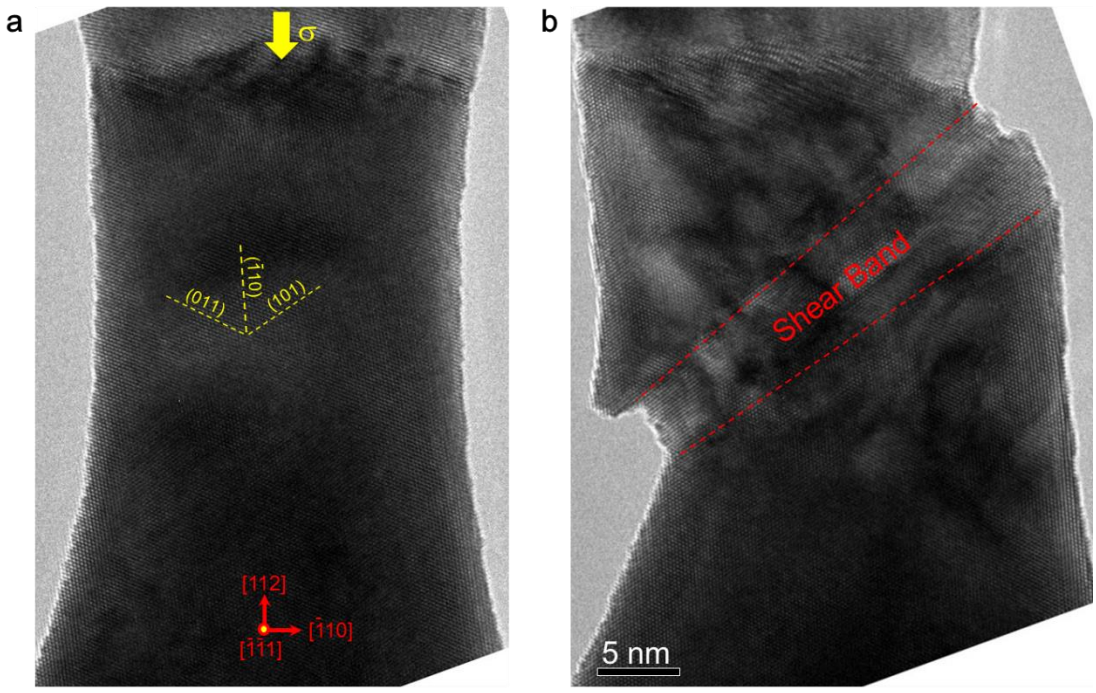

Figure 6.8 Additional TEM images for the W bicrystal nanowire shown in Figure 6.7. (a) The pristine state prior to [112] compression. (b) An additional TEM image showing the further thickening of the shear band during continued compressive loading.

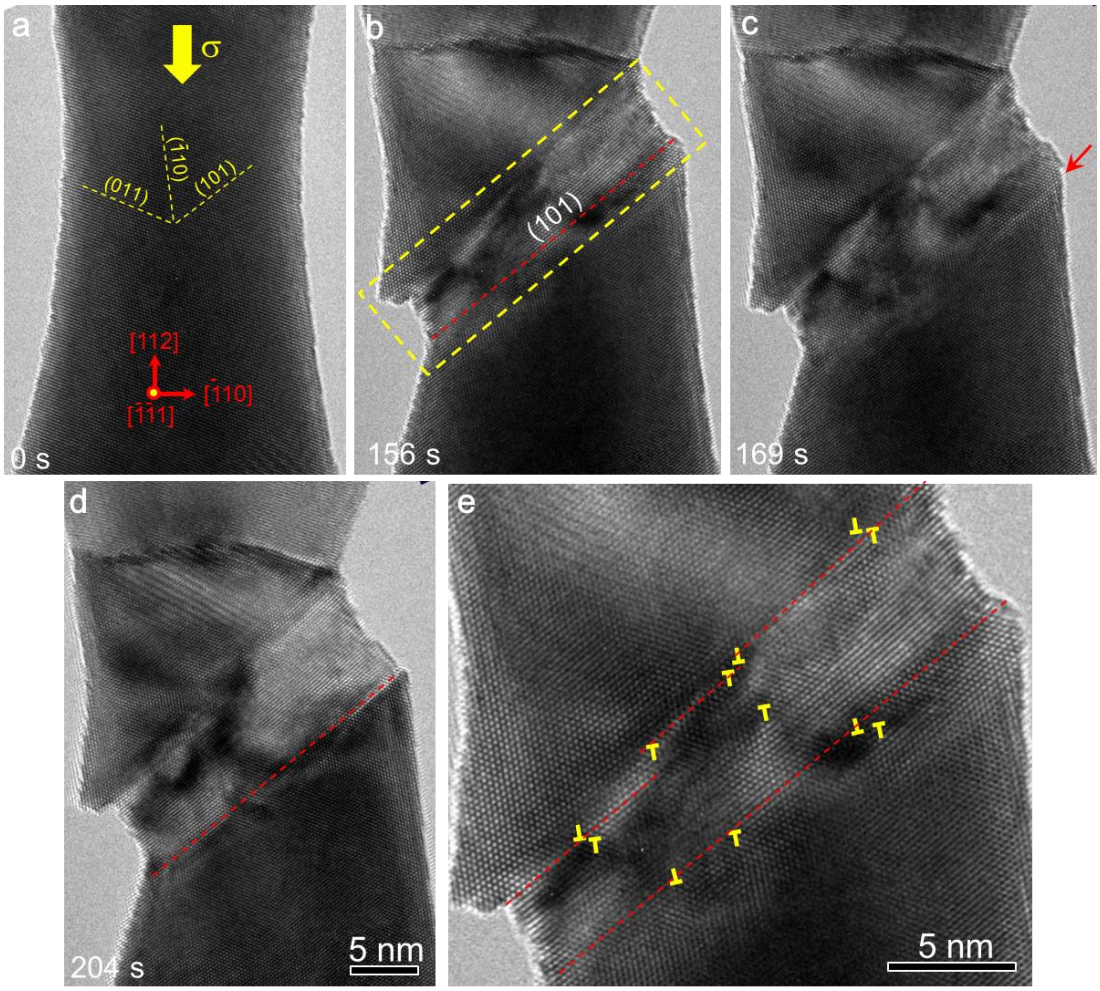

Figure 6.9 The nucleation of dislocations and the formation of a dislocation-mediated shear band in a W bicrystal nanowire under [112] compression. (a-d) Sequential TEM images showing the formation of a shear band and subsequent thickening. (e) A close-up view of the interface between the shear band and matrix in (b). The upper interface contains the atomic-level steps. Several dislocation dipoles are observed at the interfaces between the shear band and the matrix, while few dislocations appear inside the shear band.

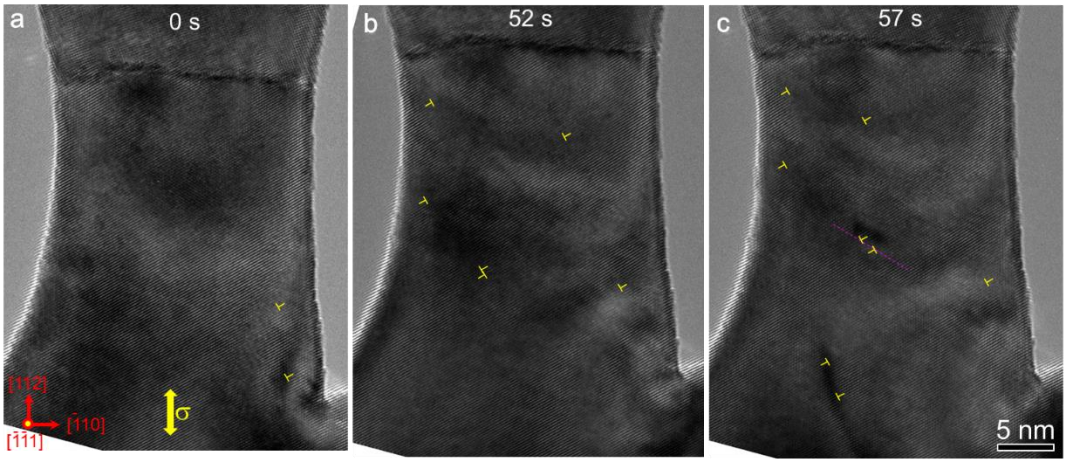

Figure 6.10 Dislocation dominated plastic deformation in a W bicrystal nanowire under [112] tension. (a) Some dislocations already exist in the W bicrystal nanowire prior to loading. (b-c) Under tensile loading, the dislocation density increases, possibly due to the nucleation from multiple sources, including free surfaces and the bulk.

Further deformation results in the formation and thickening of the shear band on the (101) plane within which the dislocation density is as high as ~2×10^{16} m^{-2}, thus generating a large local plastic strain (Figure 6.7(c), (g) and Figure 6.8-6.9). Incidentally, it has been notoriously difficult to determine the operative dislocation slip planes in BCC metals[153, 154], and the commonly used visual inspection of slip traces often caused confusion as to the {110} versus {112} slip[153]. In contrast, our in situ HRTEM experiments enable a direct unambiguous determination of the active slip plane in BCC crystals, i.e., a specific {110} plane whose activation is presumably due to the large resolved shear stress. While the recent work of Caillard reported TEM observations of {110} slip in iron[155, 156], our method provides a way to directly view the active slip planes and provides a complementary technique to that used by Caillard for the determination of slip planes in BCC metals.

6.4 Atomistic modeling of twinning dominated deformation in BCC W

To understand the competition between deformation twinning and dislocation slip, we perform atomistic studies of W single crystals under $\langle 112 \rangle$ loading. In our direct MD simulations, either tension or compression, deformation is dominated by dislocation slip, including the nucleation of dislocations from the surface, their glide inside the crystal and entanglement with each other; some dislocations eventually escape from other parts of the surface under continued loading, as shown in Figure 6.11. While the MD simulations are consistent with experimental observations, one might still question why dislocation slip is the active deformation mode under $\langle 112 \rangle$ loading, while twinning dominates under other loading orientations tested, including $\langle 110 \rangle$, $\langle 100 \rangle$ and $\langle 111 \rangle$.

To further investigate the competition between twinning and dislocation slip, we note that a surface-emanated defect in small BCC crystals can experience large resistances concurrently from both the surface and lattice. As a result, even if a surface defect such as a twin embryo has been emanated at some favorable surface site, its expansion in the nucleation process, as schematically shown in Figure 6.1h, still has to compete with other modes of defect nucleation.

To explore such competition of nucleation, we create a twin embryo near the surface of a $[112]$-oriented W crystal (Figure 6.12). This embryo belongs to the $[\bar{1}\bar{1}1](211)$ twin system, which is subjected to the largest resolved shear stress among all possible twinning systems under $[112]$ compression.

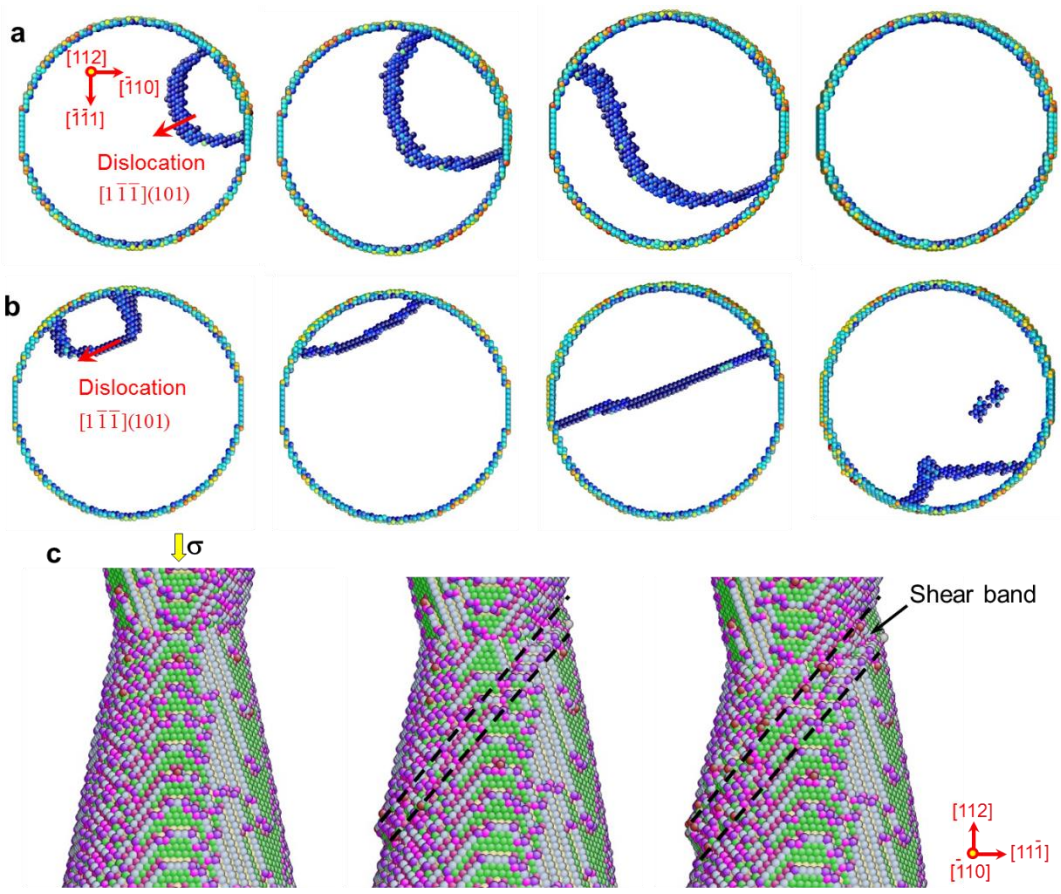

Figure 6.11 Atomistic simulations of dislocation dominated plastic deformation in a tapered W bicrystal nanowire under [112] compression. (a) Molecular statics snapshots showing the sequential process of surface nucleation, expansion and annihilation of a dislocation half loop, which primarily consists of an edge dislocation segment. (b) Similar to (a), except that the dislocation half loop primarily consists of a screw dislocation segment. (c) Sequential MD snapshots showing the morphological changes of the W bicrystal nanowire during the formation of a shear band.

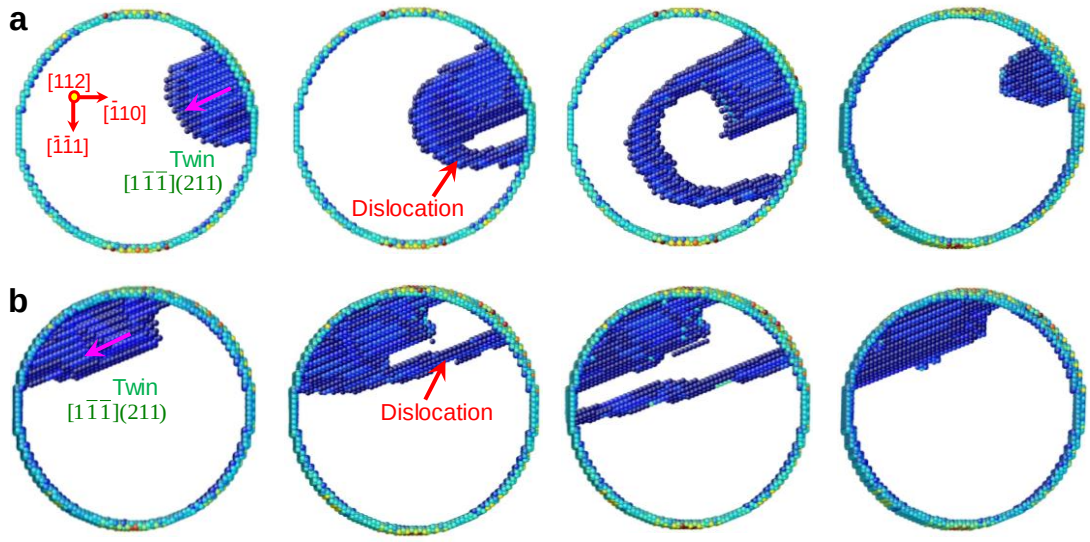

Figure 6.12 Atomistic simulations of the competition between twinning and dislocation slip in W under [112] compression. (a) Nucleation and expansion of a dislocation loop from the edge of a pre-embedded twin embryo, whose edge is predominantly perpendicular to the twin shear direction (pink arrow). (b) Similar to (a), except that the dominant edge of the twin embryo is parallel to the twin shear direction. In both cases, the expansion of the twin embryo is suppressed due to the competing nucleation of a dislocation that accommodates the load and results in shrinkage of the twin embryo.

The twin embryo in W nanowires was first created under constraints and then fully relaxed by molecular statics simulations using LAMMPS with the conjugate gradient (CG) algorithm. To create a twin embryo, a pristine W NW was compressed to 4% so as to generate the internal stress to facilitate the twin formation. Then, a twin embryo was embedded into the nanowire through the following procedures: (a) A patch of five layers of atoms in $\{112\}$ planes were selected near the side face of the nanowire. (b) Each layer of atoms were moved by a prescribed displacement along the favored twin shear direction as follows: the displacement for the first layer was $1/3\langle 111\rangle$, the second was $1/6\langle 111\rangle$, the third was 0, the forth was $-1/6\langle 111\rangle$ and the fifth was $-1/3\langle 111\rangle$. (c) The nanowire was

relaxed by CG while the displaced atoms in the patch were constrained from moving. Under such constrained relaxation, an incipient twin embryo was formed in the nanowire. (d) After (c), the constraints on atoms in the patch were removed and the system was fully relaxed. As a result, a twin embryo can be created in both the $[\bar{1}10]$ and $[112]$ nanowires.

During molecular statics relaxations under various applied stresses, we always observe the nucleation of individual dislocation loops from the edge of the twin embryo rather than the expansion of the twin embryo itself. Similar dislocation dominated responses are observed when a twin embryo is created at other surface locations (e.g., Figure 6.12(b)). These results demonstrate that the nucleation of the twin embryo can be limited by the lateral expansion of its nucleation process under $[112]$ compression. In contrast, for other loading orientations studied, the twin embryo created at the surface always form a complete twin band and then thickens through layer-by-layer migration of twin boundary, as seen during $[\bar{1}10]$ compression. These atomistic studies clearly demonstrate the surface nucleation controlled deformation mechanisms in nanoscale BCC W crystals; and during $\langle 112 \rangle$ compression, the surface-emanated twin embryos cannot expand due to the competition of dislocation nucleation. These MD results also reinforce the notion of twinning dominated deformation mechanism in BCC W nanostructures, except for $\langle 112 \rangle$ loading.

6.5 Competition between twinning and dislocation in BCC W

Below we discuss in detail our quantitative studies of dislocation nucleation and twin formation. Recall that in our experiments, at the onset of yielding, the *resolved shear*

stresses for the formation of deformation twins and dislocations were estimated (from lattice strain measurements) to be very high, *i.e.*, about 9 GPa for twinning on {112} planes and 7.2 GPa for dislocations on {110} planes. Those measured stresses are close to the ideal shear strengths of W on {112} and {110} slip planes (~ 18 GPa) from first principles calculations[52,53]. Therefore, in our experiments, the formation of both deformation twins and dislocations in W nanoscale crystals are most likely controlled by their nucleation at the free surface, particularly at the intersection between free surface and grain boundary for deformation twins.

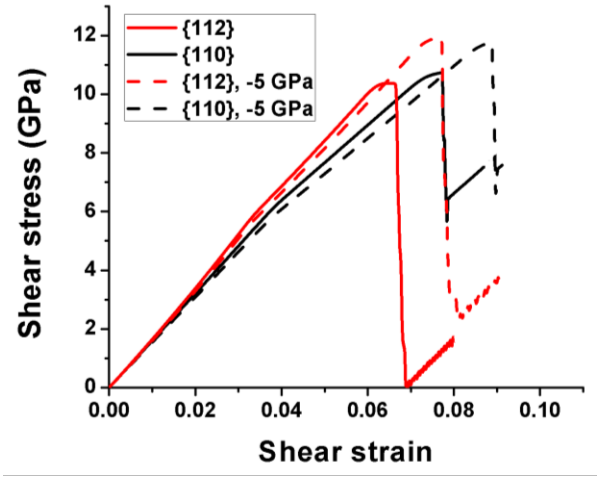

Figure 6.13 Stress-strain curves of simple shear calculated from the interatomic potential used in this work. Solid lines correspond to the simulations carried out with only a pure shear stress applied on the {112} or {110} planes. Dashed lines correspond to the case with an additional constant compressive stress of 5 GPa normal to the noted slip planes.

To support the experimental results, we have performed atomistic simulations to evaluate the critical loads for surface nucleation of deformation twins and dislocations during $[\bar{1}10]$ compression. First, we performed molecular statics calculations of $\langle 111 \rangle$

simple shear on the {112} and {110} slip planes. To understand the effect of normal stress on the shear plane under axial loading, we also included normal stresses of 0 GPa and -5 GPa (compressive stress) on the shear plane. Figure 6.13 shows the calculated shear stress-strain curves on {112} and {110}, respectively. The maximum shear stresses obtained from the interatomic potential are in the range of 10-12 GPa, as compared with the values of around 18 GPa given by the first principles calculations[52,53]. This comparison indicates that the interatomic potentials used here will moderately under-predict the nucleation stresses in real tungsten nanowires by a factor between 1.5 and 2.0.

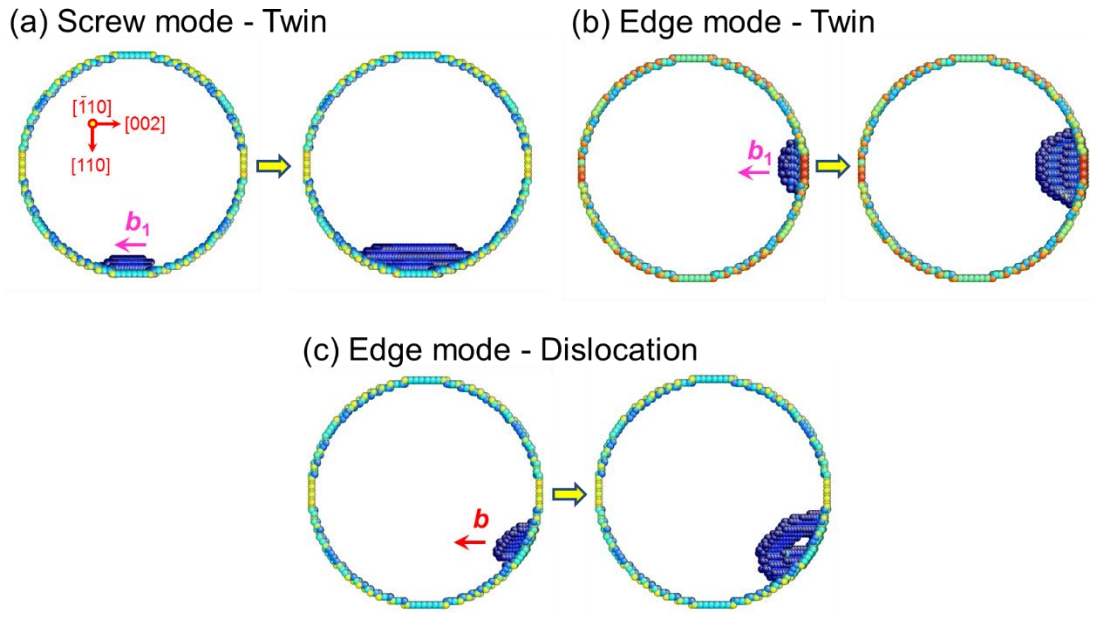

Figure 6.14 Molecular statics studies of the critical stresses of surface nucleation of twin and dislocation in a W nanowire under <110> compression. (a) The nucleation of a screw-mode twin where the twinning shear is $1/6[\bar{1}11](\bar{1}12)$ at the critical axial compression of ~18 GPa. (b) The nucleation of an edge-mode twin at the critical axial compression of ~14.5 GPa. (c) The surface nucleation of an edge-mode dislocation with the slip system of $1/2[\bar{1}11](10\bar{1})$ at the critical axial compression of ~18 GPa. These simulations indicate that twinning is favored over dislocation nucleation under <110> compression.

Secondly, we performed molecular statics simulations to evaluate the critical stresses for the nucleation of deformation twins and dislocations at different surface locations in a W nanowire during $[\bar{1}10]$ compression. To determine the stress required to propagate a defect in these nanowires, we embed a small embryonic twin or dislocation loop with similar sizes near the free surface. As described in detail in Simulation Methods, this is achieved by assigning shear displacement to the selected atoms in the loop and subsequently relaxing the whole system while holding a constant load. We then gradually increase the applied load to determine the critical one for growing this embryonic surface defect. This controlled study of defect nucleation allows us to estimate the critical loads of surface nucleation of twin and dislocation at different surface sites, as well as to determine the relative load required to nucleate a twin and a dislocation at the same type of surface site. Figure 6.14a shows the screw mode of surface nucleation, where the primary edge of the incipient loop is parallel to the shear direction of $\langle 111 \rangle$. In this case, the twin embryo with the twin system of $1/6[\bar{1}\bar{1}1](\bar{1}\bar{1}2)$ nucleates at the critical stress of 18 GPa. Similarly, Figure 6.14(b) shows the edge mode of surface nucleation, where the primary edge of the incipient loop is perpendicular to the shear direction of $\langle 111 \rangle$. In this case, an embryonic twin loop embedded on the {112} shear plane generates the same type of twin product as (a) at the critical axial compression of about 14.5 GPa. In contrast, Figure 6.14(c) shows the nucleation of a surface defect on the {110} plane which, in this case, results in the nucleation of an edge dislocation. The final product is a dislocation with the slip system of $1/2[\bar{1}\bar{1}1](\bar{1}01)$ at the critical axial compression of ~18 GPa. These unit process studies give the critical axial loads of twin nucleation that are on the same order of magnitude as both

experimental measurements and our MD results. Moreover, these simulations indicate that twinning is favored over dislocation nucleation for <110> compression. Additionally, we note that the above studies focus on single crystals, but the intersection between free surface and grain boundary in bicrystals can create surface heterogeneities that facilitate the twin or dislocation nucleation, as shown in our MD simulations of bicrystals. However, the simulated critical loads for surface nucleation between single crystal and bicrystal setups are similar.

Finally, we further performed molecular statics simulations to study the expansion of twins that penetrate the nanowire during $[\bar{1}10]$ compression. Similarly, small embryonic twin loops with similar sizes were embedded at different surface sites. This controlled study allows us to reveal the expansion behavior of these twin embryos nucleated from different surface locations. Figure 6.15 shows the sequential molecular statics snapshots of expansion of a screw-type twin embryo, the edge of which is primarily parallel to the twin shear direction. During its nucleation process, this screw-type twin embryo can easily expand laterally, resulting in a complete twin plate, similar to the one shown in Figure 6.1(i). Similarly, Figure 6.15(b) shows the expansion of an edge-type twin embryo, resulting in a complete twin plate in the nanowire cross. The above molecular statics simulations demonstrate that a surface twin embryo can easily expand laterally to form a fully developed twin band in a $[\bar{1}10]$-oriented W nanowire after its nucleation from the favorable free surface sites.

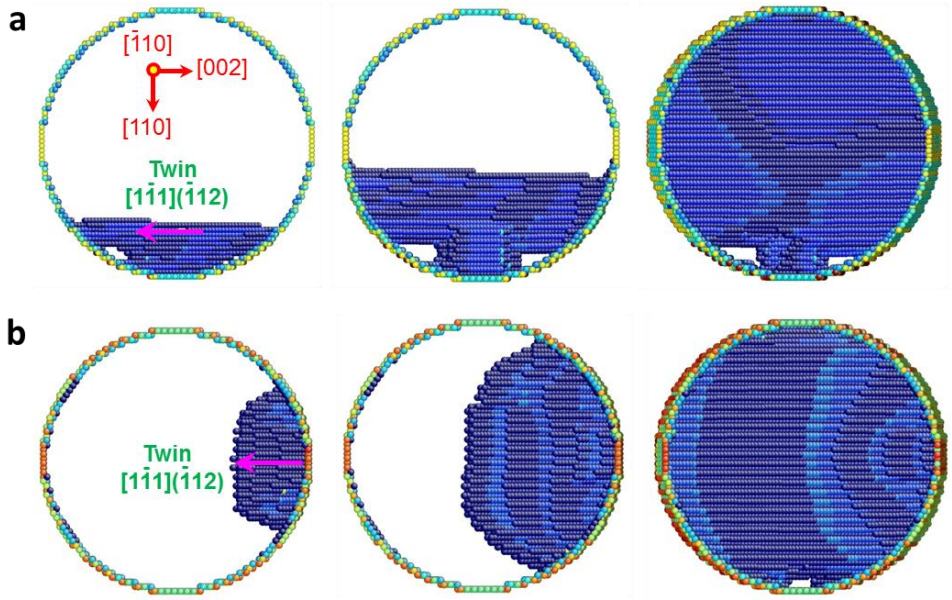

Figure 6.15 Atomistic simulations of the lateral expansion of a surface twin embryo in a W nanowire under $[\bar{1}10]$ compression. (a) Sequential molecular statics snapshots showing the lateral expansion of a twin embryo into a fully developed twin plate, as shown in Figure 6.1i. The edge of the twin embryo is primarily parallel to the twin shear direction (pink arrow). (b) Similar to (a), except that the edge of the twin embryo is perpendicular to the twin shear direction (pink arrow).

From the above modeling studies of surface nucleation and expansion of defects, we conclude that deformation twinning in nanoscale W crystals is controlled by surface nucleation, *i.e.*, irrespective of types of surface sites and shear modes, a twin embryo can nucleate from the free surface and expand into a twin band in a $[\bar{1}10]$-oriented W nanowire at the characteristic load level measured in experiments. Combining the results of twinning under $\langle 110 \rangle$ compression (Figure 6.14-15) with the results of surface nucleation of dislocations and twins under $\langle 112 \rangle$ compression (Figure 6.11 and Figure 6.12), we demonstrate that deformation in nanoscale W crystals should be controlled by the competing nucleation mechanisms of twins and dislocations.

Table 6.1 Largest Schmid factors on the dislocation slip and deformation twinning systems for the four loading orientations tested in BCC W

Loading orientation	Dislocation		Twinning		Dominant mechanism in experiment
	Slip system	Schmid factor	Twin system	Schmid factor	
$[\bar{1}10]$	$1/2[\bar{1}11](\bar{1}01)$	0.4082	$1/6[\bar{1}11](\bar{1}12)$	0.4714	Twinning
$[112]$	$1/2[\bar{1}\bar{1}1](101)$	0.4082	$1/6[\bar{1}\bar{1}1](211)$	0.3928	Dislocation slip
$[100]$	$1/2[\bar{1}11](\bar{1}\bar{1}0)$	0.4082	$1/6[\bar{1}11](\bar{2}\bar{1}1)$	0.4714	Twinning
$[\bar{1}11]$	$1/2[\bar{1}11](\bar{1}01)$	0.2722	$1/6[\bar{1}11](\bar{1}12)$	0.3143	Twinning

Further insights into the competition between deformation twinning and dislocation slip are gained by an analysis of the resolved shear stress on the respective twin and slip systems. Currently, there is a lack of established criteria for selecting the active mode of deformation twinning or dislocation slip in BCC metals. However, one expects that the resolved shear stress should play an important role. Table 6.1 lists the largest Schmid factors of twinning and dislocation slip for each of the four loading orientations tested. Under $\langle 110 \rangle$, $\langle 100 \rangle$ and $\langle 111 \rangle$ axial loadings, the corresponding Schmid factors of twinning are larger by a finite margin than those of dislocation slip. This is consistent with the observed twinning dominated deformation mechanism in the experiments. However, for $\langle 112 \rangle$ axial loading, the Schmid factors of twinning and dislocation slip are very close, which implies similar resolved shear stresses to drive twin formation and dislocation

nucleation. In this case, the above atomistic simulations shown in Figure 6.12 suggest that the dislocation nucleation is favored, possibly due to the difficulty of lateral expansion of the twin embryo. Nevertheless, a mechanistically-based, quantitative criterion for selecting the deformation twinning versus dislocation slip warrants further research in the future.

It is worthwhile to compare and contrast the deformation mechanisms of FCC and BCC nanostructures. First, mechanical twinning can become the dominant deformation mechanism in both BCC and FCC nanoscale crystals at room temperature and low strain rate. While deformation twinning has been well documented in FCC nanostructures[34, 90-92], our work provides the first direct experimental evidence of twinning dominated deformation mechanism in BCC W nanostructures. The twinning dominance in nanoscale FCC and BCC metals arises due to the prevalent high stresses that favor the twinning over dislocation slip. However, unlike FCC metals, twin nucleation in BCC metals is subject to large surface and lattice resistances. Our atomistic simulations suggest that the nucleation of twin embryos can be limited by their lateral expansion under $\langle 112 \rangle$ compression, while the vertical twin thickening is relatively easy as it involves the glide of twin interface dislocations with low energy barriers[157]. As a result, dislocation slip can dominate over twinning for certain loading conditions such as $\langle 112 \rangle$ tension and compression in W nanostructures. Second, dislocation starvation is typical in FCC nanostructures[89], but not always observed in the BCC W nanostructures. In BCC nanoscale crystals under $\langle 112 \rangle$ loading, numerous nucleation events can occur simultaneously, and a gradual increase in dislocation density occurs during continual straining. This difference may play a role in the observed different strengthening trends in small scale FCC and BCC single crystals when dislocations dominant the deformation[113, 158]. Third, deformation twinning can be

pseudoelastic in elemental BCC nanoscale crystals during loading and unloading, as shown in the present work. In contrast, while the deformation induced twinning has been experimentally observed in FCC nanowires[90-92], the detwinning and resultant pseudoelasticity have not been reported to date. It is also of interest to note the recent observations of pseudoelastic deformation in nanoscale shape memory alloys[159] and ceramics[160]. Pseudoelasticity could allow for reversible inelastic deformation, superelasticity, large actuation, energy storage and mechanical damping in micro/nano-devices[87, 159-161]. Finally, we comment that the in situ welding technique developed in this work provides a relatively simple and yet effective means of sample preparation to facilitate the in situ atomic-scale mechanical testing of nanostructures. Our work also demonstrates the advantage of *in situ* HRTEM deformation experiments that allow the unambiguous determination of active systems of dislocation slip, which has been a challenge for BCC crystals[86, 153].

6.6 Conclusions

In conclusion, the combined in situ TEM experiments and atomistic simulations have revealed that deformation twinning is the dominant deformation mode in BCC W nanoscale crystals at room temperature and low strain rates, when loaded along $\langle 100 \rangle$, $\langle 110 \rangle$, and $\langle 111 \rangle$ directions. Under cyclic loads, deformation twinning is pseudoelastic and such a unique nanoscale deformation behavior could enable large actuation, energy storage and mechanical damping in micro/nano-devices. Our in situ TEM experiments also reveal that dislocation plasticity is the primary mode of deformation for $\langle 112 \rangle$ loading, resulting in plastic yielding. The loading orientation effect is attributed to the competing

nucleation mechanism of defects in small-scale BCC crystals. Broadly, our work demonstrates that the combined in situ HRTEM nanomechanical testing and atomistic modeling enable a deeper understanding of the fundamental deformation mechanisms in nanomaterials, and such integrated research may ultimately enable the design of nanostructured materials to realize their latent mechanical strength to the full.

CHAPTER 7. CONCLUSIONS

Heterogeneous nanostructured metals have an unprecedented synergy of strength and ductility. This thesis presents multiscale modeling of the heterogeneous nanostructured metals. The multiscale modeling methods are molecular dynamics simulations, molecular static simulations and crystal plasticity finite element modeling. Three kinds of heterogeneous nanostructured metals are studied. They are gradient nano-grained copper, transmodal grained aluminum and additively manufactured stainless steel.

GNG metals have the unique microstructure with a gradient distribution of grain sizes. We develop both crystal plasticity and atomistic models to investigate the mechanical behavior of gradient nano-grained (GNG) Cu. We adapt the classical crystal plasticity theory to account for grain-size-dependent yield strengths in the Hall-Petch regime − smaller grain is stronger. The associated finite element simulations reveal the gradient distributions of both stress and plastic strain in the cross section of GNG samples subjected to axial tension. These gradient distributions arise due to progressive yielding of gradient grains under an overall uniform deformation. They stand in stark contrast to the widely studied strain gradient plasticity induced by applying non-uniform deformations such as torsion, bending, and indentation. Grain-size-dependent strain hardening in GNG Cu is also studied to examine its effects on the sample-level hardening. Moreover, we perform molecular dynamics simulations to reveal the competing deformation mechanisms of grain growth and dislocation plasticity in the inverse Hall-Petch regime − smaller grain is softer. Our models and simulations gain mechanistic insights into the mechanical behavior of

GNG metals, and also provide a framework for further study of the optimal gradient nano-grains in the future.

Transmodal grained Al has a mixture of grains with different sizes ranging from fine grains to coarse grains. The mixture of grains with different sizes are distributed in a nonuniform way. We adapted Laguerre Voronoi tessellation to develop three dimensional polycrystal structures of bimodal grained Al. The grain size and size distribution are fully controllable. The models are further meshed to be developed into finite element models. Grain size-dependent crystal plasticity finite element (CPFE) simulations are performed to investigate the strength, as well as effects of grain-level heterogeneities. The simulation results show that the strength of transmodal grained Al strongly depends on the grain size distribution. Several transmodal of different grains size distribution are studied. An optimal material design solution of transmodal grained Al is found in our simulations. Bimodal grained Al has grains of two different sizes, fine and coarse. The fine grains and the coarse grains are mixed nonuniformly. The models of transmodal grained Al are developed. The models of bimodal grained Al have the same grain size and size distribution as the experimental samples. Finite element models of transmodal grained Al are developed and grain size-dependent CPFE simulations are performed to study the effects of grain size distribution on the strength. The simulation results show that the strength of bimodal grained Al is following the rule of mixture. The stresses are nonuniform in the sample. The stress-strain curves match well with the experimental results.

Nanotwinned Cu exhibits an unusual combination of ultra-high strength and high tensile ductility. We study the fracture in a free-standing thin film of nanotwinned Cu using molecular dynamics (MD) simulations. For a pre-crack inclined to the twin boundary, MD

simulations show a characteristic fracture mode of zigzag cracking, which arises due to periodic deflections of the crack path by twin boundaries. The mechanism of fracture involves the screw dislocation-mediated local thinning ahead of the crack, instead of cleavage fracture. Importantly, MD simulations show a unique fracture footprint of $\langle 110 \rangle$ -oriented crack edges, consistent with the previous experimental observation from in situ transmission electron microscopy. Our results reveal the toughening mechanisms by nanotwins and also have broader implications for understanding the mechanical failure of metallic thin films.

Additively manufactured (AM) austenitic stainless steels can have hardness values over four times higher than that predicted from the Hall-Petch scaling law. We demonstrate that the strength and plastic deformation of AM steels are predominantly controlled by the structurally and chemically interwoven heterogeneities and defects. we performed *size-dependent* crystal plasticity finite element (CPFE) simulations to investigate the effects of grain-level heterogeneities as well as sub-grain heterogeneities and defects on plastic responses. The CPFE simulation result reinforces the notion that the strength of AM SS is controlled by the collective effect of sub-grain heterogeneities and defects. We also performed molecular dynamics (MD) simulations of plastic deformation in a model of polycrystalline fcc steel. Our MD simulations focused on the low angle grain boundaries. MD simulations revealed that plasticity in this steel sample was mediated by the motion of dislocations, stacking faults, and twins. This work demonstrates that the mechanical properties of AM metals and alloys are controlled by their microstructural heterogeneities and sub-grain defects uniquely produced during additive manufacturing.

By using in situ high-resolution transmission electron microscopy and atomistic simulations, here we show that twinning is the dominant deformation mechanism in nanoscale crystals of BCC tungsten. Such deformation twinning is pseudoelastic, manifested through reversible detwinning during unloading. We find that the competition between twinning and dislocation slip can be mediated by loading orientation, which is attributed to the competing nucleation mechanism of defects in nanoscale BCC crystals. Our work provides direct observations of deformation twinning as well as new insights into the deformation mechanism in BCC nanostructures.

The microstructure uncertainties arise from the heterogeneities of microstructures and enhance the strength-ductility properties. The microstructure uncertainties enhance the strength and ductility through engineering materials with gradient grains, transmdoal grains and 3D printed microstructures. Therefore, heterogeneous microstructures turn microstructure uncertainties into valuable features of material properties.

REFERENCES

[1] C.C. Koch, D.G. Morris, K. Lu, A. Inoue. Ductility of nanostructured materials, MRS Bulletin 24 (1999) 54-58.

[2] Y.M. Wang, M.W. Chen, F.H. Zhou, E. Ma. High tensile ductility in a nanostructured metal, Nature 419 (2002) 912-915.

[3] N. Tsuji, Y. Ito, Y. Saito, Y. Minamino. Strength and ductility of ultrafine grained aluminum and iron produced by ARB and annealing, Scripta Materialia 47 (2002) 893-899.

[4] R. Valiev. Nanostructuring of metals by severe plastic deformation for advanced properties, Nature Materials 3 (2004) 511-516.

[5] Y.T. Zhu, X.Z. Liao. Nanostructured metals - Retaining ductility, Nature Materials 3 (2004) 351-352.

[6] E. Ma. Eight routes to improve the tensile ductility of bulk nanostructured metals and alloys, JOM 58 (2006) 49-53.

[7] K. Lu. Making strong nanomaterials ductile with gradients, Science 345 (2014) 1455-1456.

[8] K. Lu. Stabilizing nanostructures in metals using grain and twin boundary architectures, Nature Reviews Materials (2016) 16019.

[9] K.S. Kumar, H. Van Swygenhoven, S. Suresh. Mechanical behavior of nanocrystalline metals and alloys, Acta Materialia 51 (2003) 5743-5774.

[10] M.A. Meyers, A. Mishra, D.J. Benson. Mechanical properties of nanocrystalline materials, Progress in Materials Science 51 (2006) 427-556.

[11] Y.H. Zhao, E.J. Lavernia. The mechanical properties of multi-scale metallic materials. in: Whang SH, (Ed.). Nanostructured Metals and Alloys. Woodhead Publishing Cambridge, 2011. pp. 375-429.

[12] A.H. Cottrell. Strong solids, Proceedings of the Royal Society of London A282 (1964) 2-9.

[13] U.G.K. Wegst, H. Bai, E. Saiz, A.P. Tomsia, R.O. Ritchie. Bioinspired structural materials, Nature Materials 14 (2015) 23-36.

[14] T. Zhu, J. Li. Ultra-strength Materials, Progress in Materials Science 55 (2010) 710-757.

[15] D. Pan, S. Kuwano, T. Fujita, M.W. Chen. Ultra-Large Room-Temperature Compressive Plasticity of a Nanocrystalline Metal, Nano Letters 7 (2007) 2108-2111.

[16] E.W. Hart. Theory of tensile test, Acta Metallurgica 15 (1967) 351-355.

[17] J.W. Hutchinson, K.W. Neale. Influence of strain-rate sensitivity on necking under uniaxial tension, Acta Metallurgica 25 (1977) 839-846.

[18] Y.M. Wang, E. Ma. Strain hardening, strain rate sensitivity, and ductility of nanostructured metals, Materials Science And Engineering A 375-77 (2004) 46-52.

[19] M. Dao, L. Lu, Y.F. Shen, S. Suresh. Strength, strain-rate sensitivity and ductility of copper with nanoscale twins, Acta Materialia 54 (2006) 5421-5432.

[20] L. Lu, M. Dao, T. Zhu, J. Li. Size dependence of rate-controlling deformation mechanisms in nanotwinned copper, Scripta Materialia 60 (2009) 1062-1066.

[21] R.O. Ritchie. The conflicts between strength and toughness, Nature Materials 10 (2011) 817-822.

[22] X. Wu, F. Yuan, M. Yang, P. Jiang, C. Zhang, L. Chen, Y. Wei, E. Ma. Nanodomained nickel unite nanocrystal strength with coarse-grain ductility, Scientific Reports 5 (2015) 11728.

[23] L. Lu, Y.F. Shen, X.H. Chen, L.H. Qian, K. Lu. Ultrahigh strength and high electrical conductivity in copper, Science 304 (2004) 422-426.

[24] P.V. Liddicoat, X.-Z. Liao, Y. Zhao, Y. Zhu, M.Y. Murashkin, E.J. Lavernia, R.Z. Valiev, S.P. Ringer. Nanostructural hierarchy increases the strength of aluminium alloys, Nat Commun 1 (2010) 63.

[25] X. Wu, P. Jiang, L. Chen, F. Yuan, Y.T. Zhu. Extraordinary strain hardening by gradient structure, Proceedings of the National Academy of Sciences of the United States of America 111 (2014) 7197-7201.

[26] Y.H. Zhao, T. Topping, J.F. Bingert, J.J. Thornton, A.M. Dangelewicz, Y. Li, W. Liu, Y.T. Zhu, Y.Z. Zhou, E.L. Lavernia. High tensile ductility and strength in bulk nanostructured nickel, Advanced Materials 20 (2008) 3028-3033.

[27] T.H. Fang, W.L. Li, N.R. Tao, K. Lu. Revealing extraordinary intrinsic tensile plasticity in gradient nano-grained copper, Science 331 (2011) 1587-1590.

[28] X. Wu, M. Yang, F. Yuan, G. Wu, Y. Wei, X. Huang, Y. Zhu. Heterogeneous lamella structure unites ultrafine-grain strength with coarse-grain ductility, Proceedings of the National Academy of Sciences of the United States of America 112 (2015) 14501-14505.

[29] Y. Wei, Y. Li, L. Zhu, Y. Liu, X. Lei, G. Wang, Y. Wu, Z. Mi, J. Liu, H. Wang, H. Gao. Evading the strength- ductility trade-off dilemma in steel through gradient hierarchical nanotwins, Nature Communications 5 (2014) 3580.

[30] F. Dalla Torre, H. Van Swygenhoven, M. Victoria. Nanocrystalline electrodeposited Ni: microstructure and tensile properties, Acta Materialia 50 (2002) 3957-3970.

[31] M.F. Ashby. Deformation of plastically non-homogenous materials Philosophical Magazine 21 (1970) 399-424.

[32] Y. Estrin, A. Vinogradov. Extreme grain refinement by severe plastic deformation: A wealth of challenging science, Acta Materialia 61 (2013) 782-817.

[33] Y.S. Li, N.R. Tao, K. Lu. Microstructural evolution and nanostructure formation in copper during dynamic plastic deformation at cryogenic temperatures, Acta Materialia 56 (2008) 230-241.

[34] Y.T. Zhu, X.Z. Liao, X.L. Wu. Deformation twinning in nanocrystalline materials, Prog. Mater. Sci. 57 (2012) 1-62.

[35] S. Suresh. Graded materials for resistance to contact deformation and damage, Science 292 (2001) 2447-2451.

[36] R. Thevamaran, O. Lawal, S. Yazdi, S.-J. Jeon, J.-H. Lee, E.L. Thomas. Dynamic creation and evolution of gradient nanostructure in single-crystal metallic microcubes, Science 354 (2016) 312-316.

[37] D.A. Hughes. Microstructure evolution, slip patterns and flow stress, Mater. Sci. Eng. A 319–321 (2001) 46-54.

[38] D.A. Hughes, N. Hansen. Exploring the Limit of Dislocation Based Plasticity in Nanostructured Metals, Physical Review Letters 112 (2014) 135504.

[39] G.M. Le, A. Godfrey, N. Hansen, W. Liu, G. Winther, X. Huang. Influence of grain size in the near-micrometre regime on the deformation microstructure in aluminium, Acta Mater. 61 (2013) 7072-7086.

[40] I. Gibson, D. Rosen, B. Stucker. Additive Manufacturing Technologies. 2nd ed., Springer New York, 2015.

[41] L. Thijs, M.L. Montero Sistiaga, R. Wauthle, Q. Xie, J.-P. Kruth, J. Van Humbeeck. Strong morphological and crystallographic texture and resulting yield strength anisotropy in selective laser melted tantalum, Acta Mater. 61 (2013) 4657-4668.

[42] T. Zhu, J. Li. Ultra-strength materials, Prog. Mater. Sci. 55 (2010) 710-757.

[43] Y. Wang. Multiscale Uncertainty Quantification Based on a Generalized Hidden Markov Model, Journal of Mechanical Design 133 (2011) 031004-031004-031010.

[44] V. Yamakov, D. Wolf, S.R. Phillpot, A.K. Mukherjee, H. Gleiter. Dislocation processes in the deformation of nanocrystalline aluminium by molecular-dynamics simulation, Nat. Mater. 1 (2002) 45-49.

[45] J. Schiøtz, K.W. Jacobsen. A maximum in the strength of nanocrystalline copper, Science 301 (2003) 1357-1359.

[46] J. Schiøtz, F.D. Di Tolla, K.W. Jacobsen. Softening of nanocrystalline metals at very small grain sizes, Nature 391 (1998) 561-563.

[47] Y.J. Wei, C. Su, L. Anand. A computational study of the mechanical behavior of nanocrystalline fcc metals, Acta Mater. 54 (2006) 3177-3190.

[48] X.L. Wu, P. Jiang, L. Chen, F.P. Yuan, Y.T. Zhu. Extraordinary strain hardening by gradient structure, P. Natl. Acad. Sci. U.S.A. 111 (2014) 7197-7201.

[49] F. Roters, P. Eisenlohr, L. Hantcherli, D.D. Tjahjanto, T.R. Bieler, D. Raabe. Overview of constitutive laws, kinematics, homogenization and multiscale methods in crystal plasticity finite-element modeling: Theory, experiments, applications, Acta Mater. 58 (2010) 1152-1211.

[50] A. Kidane, A. Lashgari, B. Li, M. McKerns, M. Ortiz, H. Owhadi, G. Ravichandran, M. Stalzer, T.J. Sullivan. Rigorous model-based uncertainty quantification with application to terminal ballistics, part I: Systems with controllable inputs and small scatter, J. Mech. Phys. Solids 60 (2012) 983-1001.

[51] M. Adams, A. Lashgari, B. Li, M. McKerns, J. Mihaly, M. Ortiz, H. Owhadi, A.J. Rosakis, M. Stalzer, T.J. Sullivan. Rigorous model-based uncertainty quantification with application to terminal ballistics—Part II. Systems with uncontrollable inputs and large scatter, J. Mech. Phys. Solids 60 (2012) 1002-1019.

[52] A.S. Argon, S. Yip. The strongest size, Phil. Mag. Lett. 86 (2006) 713-720.

[53] R.J. Asaro, S. Suresh. Mechanistic models for the activation volume and rate sensitivity in metals with nanocrystalline grains and nano-scale twins, Acta Mater. 53 (2005) 3369-3382.

[54] X.Y. Li, Y.J. Wei, L. Lu, K. Lu, H.J. Gao. Dislocation nucleation governed softening and maximum strength in nano-twinned metals, Nature 464 (2010) 877-880.

[55] Z. You, X. Li, L. Gui, Q. Lu, T. Zhu, H. Gao, L. Lu. Plastic anisotropy and associated deformation mechanisms in nanotwinned metals, Acta Materialia 61 (2013) 217-227.

[56] J.J. Li, A.K. Soh. Modeling of the plastic deformation of nanostructured materials with grain size gradient, Int. J Plasticity 39 (2012) 88-102.

[57] J. Li, A.K. Soh. Enhanced ductility of surface nano-crystallized materials by modulating grain size gradient, Modelling and Simulation in Materials Science and Engineering 20 (2012) 085002.

[58] J. Li, S. Chen, X. Wu, A.K. Soh. A physical model revealing strong strain hardening in nano-grained metals induced by grain size gradient structure, Materials Science and Engineering A 620 (2015) 16-21.

[59] A. Okabe, B. Boots, K. Sugihara, S.N. Chiu. Spatial tessellations: concepts and applications of Voronoi diagrams, John Wiley & Sons, London, UK, 2009.

[60] K. Lu, L. Lu, S. Suresh. Strengthening Materials by Engineering Coherent Internal Boundaries at the Nanoscale, Science 324 (2009) 349-352.

[61] T. Zhu, H.J. Gao. Plastic deformation mechanism in nanotwinned metals: An insight from molecular dynamics and mechanistic modeling, Scripta Materialia 66 (2012) 843-848.

[62] I.J. Beyerlein, X. Zhang, A. Misra. Growth Twins and Deformation Twins in Metals, Annual Review of Materials Research 44 (2014) 329-363.

[63] E. Bitzek, J.R. Kermode, P. Gumbsch. Atomistic aspects of fracture, International Journal of Fracture 191 (2015) 13-30.

[64] Z.H. Jin, P. Gumbsch, E. Ma, K. Albe, K. Lu, H. Hahn, H. Gleiter. The interaction mechanism of screw dislocations with coherent twin boundaries in different face-centred cubic metals, Scripta Materialia 54 (2006) 1163-1168.

[65] T. Zhu, J. Li, A. Samanta, H.G. Kim, S. Suresh. Interfacial plasticity governs strain rate sensitivity and ductility in nanostructured metals, Proceedings of the National Academy of Sciences of the USA 104 (2007) 3031-3036.

[66] L. Lu, Zhu, T., Shen, Y.F., Dao, M., Lu, K., Suresh, S. Stress relaxation and the structure size-dependence of plastic deformation in nano-twinned copper, Acta Materialia 57 (2009) 5165-5173.

[67] L. Lu, X. Chen, X. Huang, K. Lu. Revealing the Maximum Strength in Nanotwinned Copper, Science 323 (2009) 607-610.

[68] Y.J. Wei. The kinetics and energetics of dislocation mediated de-twinning in nano-twinned face-centered cubic metals, Materials Science and Engineering A 528 (2011) 1558-1566.

[69] Y.M. Wang, F. Sansoz, T. LaGrange, R.T. Ott, J. Marian, T.W. Barbee, Jr., A.V. Hamza. Defective twin boundaries in nanotwinned metals, Nature Materials 12 (2013) 697-702.

[70] E.W. Qin, L. Lu, N.R. Tao, J. Tan, K. Lu. Enhanced fracture toughness and strength in bulk nanocrystalline Cu with nanoscale twin bundles, Acta Materialia 57 (2009) 6215-6225.

[71] A. Singh, L. Tang, M. Dao, L. Lu, S. Suresh. Fracture toughness and fatigue crack growth characteristics of nanotwinned copper, Acta Materialia 59 (2011) 2437–2446.

[72] Z.W. Shan, L. Lu, A.M. Minor, E.A. Stach, S.X. Mao. The effect of twin plane spacing on the deformation of copper containing a high density of growth twins, JOM 60 (2008) 71-74.

[73] S.-W. Kim, X. Li, H. Gao, S. Kumar. In situ observations of crack arrest and bridging by nanoscale twins in copper thin films, Acta Materialia 60 (2012) 2959-2972.

[74] H. Zhou, S. Qu. The effect of nanoscale twin boundaries on fracture toughness in nanocrystalline Ni, Nanotechnology 21 (2010) 035706.

[75] D. Herzog, V. Seyda, E. Wycisk, C. Emmelmann. Additive manufacturing of metals, Acta Mater. 117 (2016) 371-392.

[76] E. MacDonald, R. Wicker. Multiprocess 3D printing for increasing component functionality, Science 353 (2016) 1512.

[77] B. Vrancken, L. Thijs, J.P. Kruth, J. Van Humbeeck. Microstructure and mechanical properties of a novel beta titanium metallic composite by selective laser melting, Acta Mater. 68 (2014) 150-158.

[78] D. Gu, Y.-C. Hagedorn, W. Meiners, G. Meng, R.J.S. Batista, K. Wissenbach, R. Poprawe. Densification behavior, microstructure evolution, and wear performance of selective laser melting processed commercially pure titanium, Acta Mater. 60 (2012) 3849-3860.

[79] K.N. Amato, S.M. Gaytan, L.E. Murr, E. Martinez, P.W. Shindo, J. Hernandez, S. Collins, F. Medina. Microstructures and mechanical behavior of Inconel 718 fabricated by selective laser melting, Acta Mater. 60 (2012) 2229-2239.

[80] J.R. Greer, J.T.M. De Hosson. Plasticity in small-sized metallic systems: Intrinsic versus extrinsic size effect, Prog. Mater. Sci. 56 (2011) 654-724.

[81] M.D. Uchic, D.M. Dimiduk, J.N. Florando, W.D. Nix. Sample Dimensions Influence Strength and Crystal Plasticity, Science 305 (2004) 986-989.

[82] Z.W. Shan, R.K. Mishra, S.A. Syed Asif, O.L. Warren, A.M. Minor. Mechanical annealing and source-limited deformation in submicrometre-diameter Ni crystals, Nat. Mater. 7 (2007) 115-119.

[83] Q. Yu, Z.-W. Shan, J. Li, X. Huang, L. Xiao, J. Sun, E. Ma. Strong crystal size effect on deformation twinning, Nature 463 (2010) 335-338.

[84] J.W. Wang, S. Narayanan, J. Yu Huang, Z. Zhang, T. Zhu, S.X. Mao. Atomic-scale dynamic process of deformation-induced stacking fault tetrahedra in gold nanocrystals, Nat. Commun. 4 (2013) 2340.

[85] J. Wang, F. Sansoz, J. Huang, Y. Liu, S. Sun, Z. Zhang, S.X. Mao. Near-ideal theoretical strength in gold nanowires containing angstrom scale twins, Nat. Commun. 4 (2013) 1742.

[86] C. Marichal, H. Van Swygenhoven, S. Van Petegem, C. Borca. {110} Slip with {112} slip traces in bcc Tungsten, Sci. Rep. 3 (2013) 2547.

[87] L. Li, C. Ortiz. Pervasive nanoscale deformation twinning as a catalyst for efficient energy dissipation in a bioceramic armour, Nat. Mater. 13 (2014) 501-507.

[88] L. Huang, Q.-J. Li, Z.-W. Shan, J. Li, J. Sun, E. Ma. A new regime for mechanical annealing and strong sample-size strengthening in body centred cubic molybdenum, Nat. Commun. 2 (2011) 547.

[89] J. Greer, W. Nix. Nanoscale gold pillars strengthened through dislocation starvation, Phys. Rev. B 73 (2006) 245410.

[90] A. Sedlmayr, E. Bitzek, D.S. Gianola, G. Richter, R. Mönig, O. Kraft. Existence of two twinning-mediated plastic deformation modes in Au nanowhiskers, Acta Mater. 60 (2012) 3985-3993.

[91] Y. Yue, P. Liu, Q. Deng, E. Ma, Z. Zhang, X. Han. Quantitative Evidence of Crossover toward Partial Dislocation Mediated Plasticity in Copper Single Crystalline Nanowires, Nano Lett. 12 (2012) 4045-4049.

[92] J.-H. Seo, Y. Yoo, N.-Y. Park, S.-W. Yoon, H. Lee, S. Han, S.-W. Lee, T.-Y. Seong, S.-C. Lee, K.-B. Lee, P.-R. Cha, H.S. Park, B. Kim, J.-P. Ahn. Superplastic Deformation of Defect-Free Au Nanowires via Coherent Twin Propagation, Nano Lett. 11 (2011) 3499-3502.

[93] A.E. Lita, D. Rosenberg, S. Nam, A.J. Miller, D. Balzar, L.M. Kaatz, R.E. Schwall. Tuning of tungsten thin film superconducting transition temperature for fabrication of photon number resolving detectors, IEEE Trans. Appl. Supercond. 15 (2005) 3528-3531.

[94] Y.-H. Lee, C.-H. Choi, Y.-T. Jang, E.-K. Kim, B.-K. Ju, N.-K. Min, J.-H. Ahn. Tungsten nanowires and their field electron emission properties, Appl. Phys. Lett. 81 (2002) 745-747.

[95] Y. Zhang, J. Li, S. To, Y. Zhang, X. Ye, L. You, Y. Sun. Automated nanomanipulation for nanodevice construction, Nanotechnology 23 (2012) 065304.

[96] H.V. Swygenhoven, P.M. Derlet, A.G. Frøseth. Stacking fault energies and slip in nanocrystalline metals, Nat. Mater. 3 (2004) 399-403.

[97] D.H. Warner, W.A. Curtin, S. Qu. Rate dependence of crack-tip processes predicts twinning trends in f.c.c. metals, Nat. Mater. 6 (2007) 876-881.

[98] V.I. Yamakov, E.H. Glaessgen. Nanoscale fracture: To twin or not to twin, Nat. Mater. 6 (2007) 795-796.

[99] J.W. Christian, S. Mahajan. Deformation twinning, Prog. Mater. Sci. 39 (1995) 1-157.

[100] Q. Yu, L. Qi, K. Chen, R.K. Mishra, J. Li, A.M. Minor. The Nanostructured Origin of Deformation Twinning, Nano Lett. 12 (2012) 887-892.

[101] A.S. Argon, S.R. Maloof. Fracture of tungsten single crystals at low temperatures, Acta Metall. 14 (1966) 1463-1468.

[102] S. Mahajan. Accommodation at deformation twins in bcc crystals, MTA 12 (1981) 379-386.

[103] J.-Y. Kim, D. Jang, J.R. Greer. Tensile and compressive behavior of tungsten, molybdenum, tantalum and niobium at the nanoscale, Acta Mater. 58 (2010) 2355-2363.

[104] M.S. Han, G. Feng, J.Y. Jung, H.J. Jung, J.R. Groves, W.D. Nix, C. Yi. Critical-temperature/Peierls-stress dependent size effects in body centered cubic nanopillars, Appl. Phys. Lett. 102 (2013) 041910.

[105] K.Y. Xie, S. Shrestha, Y. Cao, P.J. Felfer, Y. Wang, X. Liao, J.M. Cairney, S.P. Ringer. The effect of pre-existing defects on the strength and deformation behavior of α-Fe nanopillars, Acta Mater. 61 (2013) 439-452.

[106] C. Marichal, K. Srivastava, D. Weygand, S. Van Petegem, D. Grolimund, P. Gumbsch, H. Van Swygenhoven. Origin of Anomalous Slip in Tungsten, Phys. Rev. Lett. 113 (2014) 025501.

[107] C. Chisholm, H. Bei, M.B. Lowry, J. Oh, S.A. Syed Asif, O.L. Warren, Z.W. Shan, E.P. George, A.M. Minor. Dislocation starvation and exhaustion hardening in Mo alloy nanofibers, Acta Mater. 60 (2012) 2258-2264.

[108] H. Bei, S. Shim, G.M. Pharr, E.P. George. Effects of pre-strain on the compressive stress–strain response of Mo-alloy single-crystal micropillars, Acta Mater. 56 (2008) 4762-4770.

[109] A. Schneider, D. Kaufmann, B. Clark, C. Frick, P. Gruber, R. Mönig, O. Kraft, E. Arzt. Correlation between Critical Temperature and Strength of Small-Scale bcc Pillars, Phys. Rev. Lett. 103 (2009) 105501.

[110] Y.M. Wang, A.M. Hodge, J. Biener, A.V. Hamza, D.E. Barnes, K. Liu, T.G. Nieh. Deformation twinning during nanoindentation of nanocrystalline Ta, Appl. Phys. Lett. 86 (2005) 101915-101913.

[111] M.S. Duesbery, V. Vitek. Plastic anisotropy in b.c.c. transition metals, Acta Mater. 46 (1998) 1481-1492.

[112] S. Narayanan, D.L. McDowell, T. Zhu. Crystal plasticity model for BCC iron atomistically informed by kinetics of correlated kinkpair nucleation on screw dislocation, J. Mech. Phys. Solids 65 (2014) 54-68.

[113] C.R. Weinberger, W. Cai. Surface-controlled dislocation multiplication in metal micropillars, Proc. Natl. Acad. Sci. U.S.A. 105 (2008) 14304-14307.

[114] P. Gumbsch, J. Riedle, A. Hartmaier, H.F. Fischmeister. Controlling Factors for the Brittle-to-Ductile Transition in Tungsten Single Crystals, Science 282 (1998) 1293-1295.

[115] D. Brunner. Comparison of flow-stress measurements on high-purity tungsten single crystals with the kink-pair theory, Materials Transactions, JIM(Japan) 41 (2000) 152-160.

[116] Abaqus. Abaqus 6.13 documentation, Dassault Systèmes, Providence, RI, US (2013).

[117] S. Plimpton, B. Hendrickson. A new parallel method for molecular dynamics simulation of macromolecular systems, J. Comput. Chem. 17 (1996) 326-337.

[118] J. Li. AtomEye: an efficient atomistic configuration viewer, Model. Simul. Mater. Sc. 11 (2003) 173-177.

[119] J.R. Rice. Inelastic constitutive relations for solids: an internal-variable theory and its application to metal plasticity, J. Mech. Phys. Solids 19 (1971) 433-455.

[120] R.J. Asaro, J.R. Rice. Strain localization in ductile single crystals, J. Mech. Phys. Solids 25 (1977) 309-338.

[121] S.R. Kalidindi, C.A. Bronkhorst, L. Anand. Crystallographic texture evolution in bulk deformation processing of FCC metals, J. Mech. Phys. Solids 40 (1992) 537-569.

[122] Y.J. Wei, L. Anand. Grain-boundary sliding and separation in polycrystalline metals: application to nanocrystalline fcc metals, J. Mech. Phys. Solids 52 (2004) 2587-2616.

[123] E.O. Hall. The deformation and ageing of mild steel. 3. Discussion of results, Proc. Phys. Soc. Lond. B 64 (1951) 747-753.

[124] N.J. Petch. The cleavage strength of polycrystals, J. Iron Steel Inst. 174 (1953) 25-28.

[125] J. Chen, L. Lu, K. Lu. Hardness and strain rate sensitivity of nanocrystalline Cu, Scripta Mater. 54 (2006) 1913-1918.

[126] N.A. Fleck, G.M. Muller, M.F. Ashby, J.W. Hutchinson. Strain graident plasticity - Theory and experiment, Acta Metallurgica et Materialia 42 (1994) 475-487.

[127] A.G. Evans, J.W. Hutchinson. A critical assessment of theories of strain gradient plasticity, Acta Materialia 57 (2009) 1675-1688.

[128] W.D. Nix, H.J. Gao. Indentation size effects in crystalline materials: A law for strain gradient plasticity, Journal of the Mechanics and Physics of Solids 46 (1998) 411-425.

[129] M.F. Ashby. The deformation of plastically non-homogeneous materials, Philos. Mag. 21 (1970) 399-424.

[130] Y. Mishin, M.J. Mehl, D.A. Papaconstantopoulos, A.F. Voter, J.D. Kress. Structural stability and lattice defects in copper: Ab initio, tight-binding, and embedded-atom calculations, Physical Review B 63 (2001) 224106.

[131] J.W. Cahn, Y. Mishin, A. Suzuki. Coupling grain boundary motion to shear deformation, Acta Mater. 54 (2006) 4953-4975.

[132] G.J. Tucker, J.A. Zimmerman, D.L. McDowell. Shear deformation kinematics of bicrystalline grain boundaries in atomistic simulations, Model. Simul. Mater. Sc. 18 (2010) 015002.

[133] G.J. Tucker, S. Tiwari, J.A. Zimmerman, D.L. McDowell. Investigating the deformation of nanocrystalline copper with microscale kinematic metrics and molecular dynamics, J. Mech. Phys. Solids 60 (2012) 471-486.

[134] G.J. Tucker. Atomistic simulations of defect nucleation and free volume in nanocrystalline materials. Georgia Institute of Technology, 2011.

[135] G.M. Le, A. Godfrey, N. Hansen. Structure and strength of aluminum with sub-micrometer/micrometer grain size prepared by spark plasma sintering, Materials & Design 49 (2013) 360-367.

[136] R. Quey, P.R. Dawson, F. Barbe. Large-scale 3D random polycrystals for the finite element method: Generation, meshing and remeshing, Computer Methods in Applied Mechanics and Engineering 200 (2011) 1729-1745.

[137] F. Radjaï, F. Dubois. Discrete-element modeling of granular materials, Wiley-Iste, London, UK, 2011.

[138] N.V. Brilliantov, F. Spahn, J.-M. Hertzsch, T. Pöschel. Model for collisions in granular gases, Phys. Rev. E 53 (1996) 5382-5392.

[139] L.E. Silbert, D. Ertaş, G.S. Grest, T.C. Halsey, D. Levine, S.J. Plimpton. Granular flow down an inclined plane: Bagnold scaling and rheology, Phys. Rev. E 64 (2001) 051302.

[140] H.P. Zhang, H.A. Makse. Jamming transition in emulsions and granular materials, Phys. Rev. E 72 (2005) 011301.

[141] Z. Zeng, X. Li, D. Xu, L. Lu, H. Gao, T. Zhu. Gradient plasticity in gradient nano-grained metals, Extreme Mech. Lett.

[142] M. Zhang, J. Zhang, D.L. McDowell. Microstructure-based crystal plasticity modeling of cyclic deformation of Ti–6Al–4V, Int. J Plasticity 23 (2007) 1328-1348.

[143] M. Shenoy, Y. Tjiptowidjojo, D. McDowell. Microstructure-sensitive modeling of polycrystalline IN 100, Int. J Plasticity 24 (2008) 1694-1730.

[144] S. Plimpton. Fast Parallel Algorithms For Short-Range Molecular-Dynamics, Journal of Computational Physics 117 (1995) 1-19.

[145] S.M. Ohr. An electron-microscope study of crack tip deformation and its impact on the dislocation theory of fracture, Materials Science and Engineering 72 (1985) 1-35.

[146] T. Zhu, W. Yang, T. Guo. Quasi-cleavage processes driven by dislocation pileups, Acta Materialia 44 (1996) 3049-3058.

[147] J. Wang, Z. Zeng, C.R. Weinberger, Z. Zhang, T. Zhu, S.X. Mao. In situ atomic-scale observation of twinning-dominated deformation in nanoscale body-centred cubic tungsten, Nature Materials (2015) 10.1038/nmat4228.

[148] D. Jang, M. Atzmon. Grain-boundary relaxation and its effect on plasticity in nanocrystalline Fe, J. Appl. Phys. 99 (2006) 083504.

[149] R. Rodríguez-Baracaldo, J.A. Benito, J. Caro, J.M. Cabrera, J.M. Prado. Strain rate sensitivity of nanocrystalline and ultrafine-grained steel obtained by mechanical attrition, Mater. Sci. Eng. A 485 (2008) 325-333.

[150] B.P. Kashyap, K. Tangri. On the Hall-Petch relationship and substructural evolution in type 316L stainless steel, Acta Metall, Mater. 43 (1995) 3971-3981.

[151] A. Stukowski. Visualization and analysis of atomistic simulation data with OVITO–the Open Visualization Tool, http://ovito.org/, Model. Simul. Mater. Sc. 18 (2009) 015012.

[152] G. Bonny, N. Castin, D. Terentyev. Interatomic potential for studying ageing under irradiation in stainless steels: the FeNiCr model alloy, Model. Simul. Mater. Sc. 21 (2013) 085004.

[153] C.R. Weinberger, B.L. Boyce, C.C. Battaile. Slip planes in bcc transition metals, Int. Mater. Rev. 58 (2013) 296-314.

[154] K. Srivastava, D. Weygand, P. Gumbsch. Dislocation junctions as indicators of elementary slip planes in body-centered cubic metals, J. Mater. Sci. 49 (2014) 7333-7337.

[155] D. Caillard. Kinetics of dislocations in pure Fe. Part I. In situ straining experiments at room temperature, Acta Mater. 58 (2010) 3493-3503.

[156] D. Caillard. Kinetics of dislocations in pure Fe. Part II. In situ straining experiments at low temperature, Acta Mater. 58 (2010) 3504-3515.

[157] S. Ogata, J. Li, S. Yip. Energy landscape of deformation twinning in bcc and fcc metals, Phys. Rev. B 71 (2005) 224102.

[158] J.R. Greer, C.R. Weinberger, W. Cai. Comparing the strength of f.c.c. and b.c.c. sub-micrometer pillars: Compression experiments and dislocation dynamics simulations, Mater. Sci. Eng., A 493 (2008) 21-25.

[159] J.S. Juan, M.L. Nó, C.A. Schuh. Nanoscale shape-memory alloys for ultrahigh mechanical damping, Nat. Nanotechnol. 4 (2009) 415-419.

[160] A. Lai, Z.H. Du, C.L. Gan, C.A. Schuh. Shape Memory and Superelastic Ceramics at Small Scales, Science 341 (2013) 1505-1508.

[161] S. Li, X. Ding, J. Li, X. Ren, J. Sun, E. Ma. High-Efficiency Mechanical Energy Storage and Retrieval Using Interfaces in Nanowires, Nano Lett. 10 (2010) 1774-1779.